2010

Design, Modeling, Fabrication and Characterization of Three-dimensional Ferromagnetic-Core Solenoid Inductors in Su-8 Interposer Layer for Embedded Passive Component Integration with Active Chips

Robert Carl Fitch Jr.
Wright State University

DESIGN, MODELING, FABRICATION AND CHARACTERIZATION OF THREE-DIMENSIONAL FERROMAGNETIC-CORE SOLENOID INDUCTORS IN SU-8 INTERPOSER LAYER FOR EMBEDDED PASSIVE COMPONENT INTEGRATION WITH ACTIVE CHIPS

A dissertation submitted in partial fulfillment of the
requirements for the degree of
Doctor of Philosophy

By

ROBERT CARL FITCH, JR.
M.S.E.E., Air Force Institute of Technology, 1990
B.S.E.E., Louisiana Tech University, 1985
B.S.M.E., The Pennsylvania State University, 1983

2010
Wright State University

WRIGHT STATE UNIVERSITY

SCHOOL OF GRADUATE STUDIES

September 2, 2010

I HEREBY RECOMMEND THAT THE DISSERTATION PREPARED UNDER MY SUPERVISION BY Robert Carl Fitch, Jr. ENTITLED Design, Modeling, Fabrication and Characterization of Three-Dimensional Ferromagnetic-Core Solenoid Inductors in SU-8 Interposer Layer for Embedded Passive Component Integration with Active Chips BE ACCEPTED IN PARTIAL FULFILLMENT OF THE REQUIREMENTS FOR THE DEGREE OF Doctor of Philosophy.

_____

Marian K. Kazimierczuk, Ph.D.
Dissertation Director

_____

Ramana V. Grandhi, Ph. D.
Director, Ph.D. in Engineering Program

_____

Andrew Toming Hsu, Ph.D.
Dean, School of Graduate Studies

Committee on
Final Examination

_____

Antonio Crespo, Ph.D.

_____

Marty Emmert, Ph.D.

_____

Marian Kazimierczuk, Ph.D.

_____

Raymond Siferd, Ph.D.

_____

LaVern Starman, Ph.D.

ABSTRACT

Fitch, Robert Carl Jr. Ph.D., Department of Electrical Engineering, Wright State University, 2010.
Design, Modeling, Fabrication and Characterization of Three-Dimensional Ferromagnetic-Core Solenoid Inductors in SU-8 Interposer Layer for Embedded Passive Component Integration with Active Chips.

Integrated circuit technology continually presses toward higher transistor density and thus smaller dimensions, yet passive components which remain the bulk of the circuit area, surprisingly receive sideline attention. This work addresses a niche area of inductor design as it applies to the 3-dimensional (3-D) integration of active transistors and passive components. Hybrid, 3-D circuits residing on inexpensive silicon substrates can be fashioned using a photosensitive epoxy known as SU-8 serving as the interposer layer between the substrate and in which the passive components are embedded. The active components, which are known-good-chips, are secured with epoxy into deep reactive ion etched pockets in the silicon substrate. The inductors are fabricated in the SU-8 covering the active chips. This technique saves considerable money and increases the yield of 3-D circuits compared with the high cost of monolithic microwave integrated circuits (MMICs). The design of solenoid inductors was simulated using a Matlab model incorporating closed-form equations. Herein, that model was developed and verified against both empirical data from fabricated solenoids and against data from a physical simulator in CoventorWare's 3-D electromagnetic, software. A design of experiments examined the effect of solenoid geometry on inductance, quality factor and AC resistance. Additionally, solenoids were fabricated with ferromagnetic cores in an effort to study the potential of enhancing the inductance and quality factor.

TABLE OF CONTENTS

Page

LIST OF FIGURES

LIST OF TABLES

Table Page

ACKNOWLEDGEMENTS

First and foremost, I give thanks and praise to the God and Father of my Lord Jesus Christ who has fashioned an amazing Creation for us to experience. The immense architectural complexity of the time and space of this universe which we find ourselves locked may one day be revealed to those who seek His presence in their lives and acknowledge His Son as Lord; but those answers will most likely be superfluous in comparison to His great glory. He has given many great minds a small glimpse at this complexity, yet to know its full brilliance would be beyond the capacity of a human brain. I am thankful to breathe in His wonders.

Second, my family deserves far more credit than me in completing this task. The many hours of sacrifice by my wife Carol in fashioning an atmosphere of love and caring are beyond measure. She is the model of unconditional love. And my boys, Jason and Brandon, have provided me with encouragement all the way; I hope that their college careers provide them with the steppingstones to a fulfilling future. To my parents, Bob and Helen, thanks most for the discipline you instilled in me through the many memorable years we have shared. Dad, although your memory is fading, your strength of character is forever with me. Mom, your encouraging words and expressed interest in my life always fill my cup.

Finally, special thanks go to my committee, who through example, and especially one-on-one conversations, has inspired me to push through to the end, keeping my eye on the prize.

I. Introduction

A. Motivation for work

The integration of passive components into electronic circuits is an essential aspect of circuit design at any level of integration, be it at the circuit board macroscopic level at RF (radio frequencies) or at the chip microscopic level at microwave frequencies. Circuit boards, populated with active chips and passive components are shrinking in size, and at the same time the number of surface mounted passives can far outnumber active components by nearly 50:1. As an example, consider the cell phone circuit board of a 3G i-phone shown in Fig. 1 [**1**] which is 100mm by 50mm in size and produces a carrier

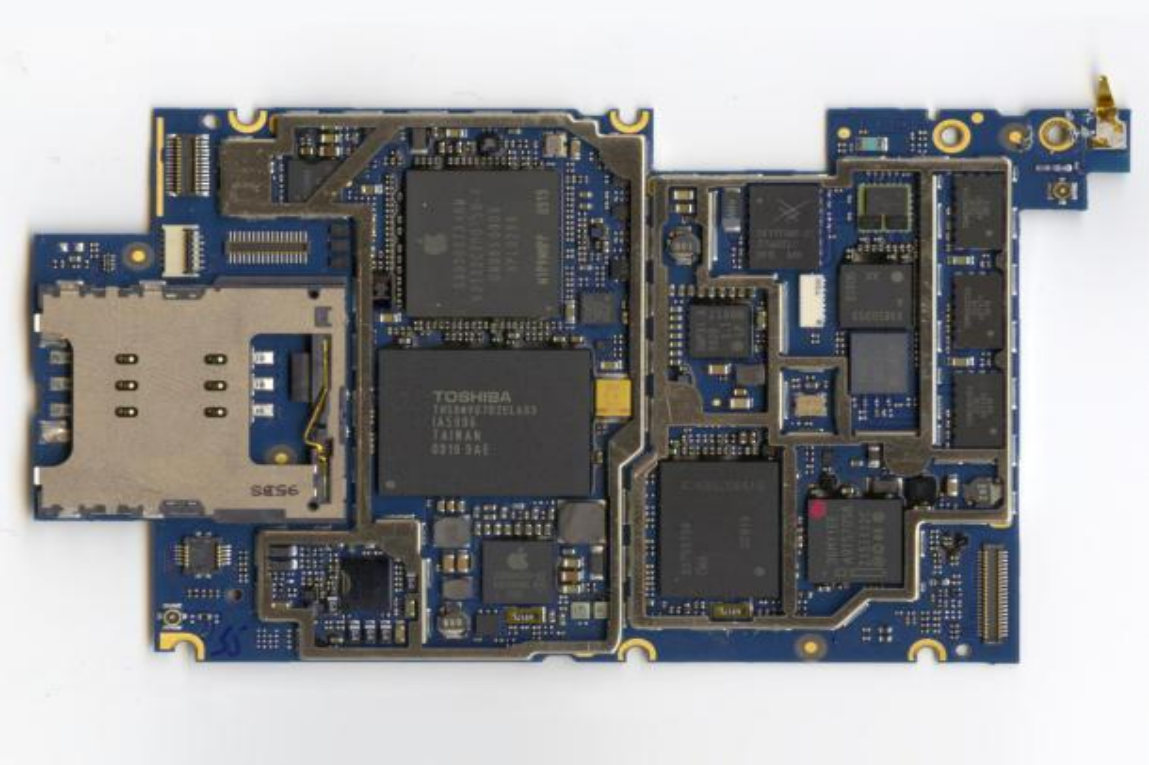

Fig. 1 3G i-phone main circuit board (100mm by 50mm).

frequency of 2.1GHz. In this case, robotic assembly is required to accurately place the smallest discrete passive components 0201 (20 x 10mils, 0.5 x 0.25mm) among active chip components. Surface mount technology (SMT) resistors, capacitors and inductors shown in Fig. 1 occupy nearly the same volume as the active components, and the size of these SMT's is at a minimum. As operating frequencies increase, the interconnect lengths decrease and require higher density packaging of the components. This can be accomplished through integration of the passive and active devices onto one substrate such as gallium arsenide (GaAs) as shown in Fig. 2 [**2**], where transmission lines are used

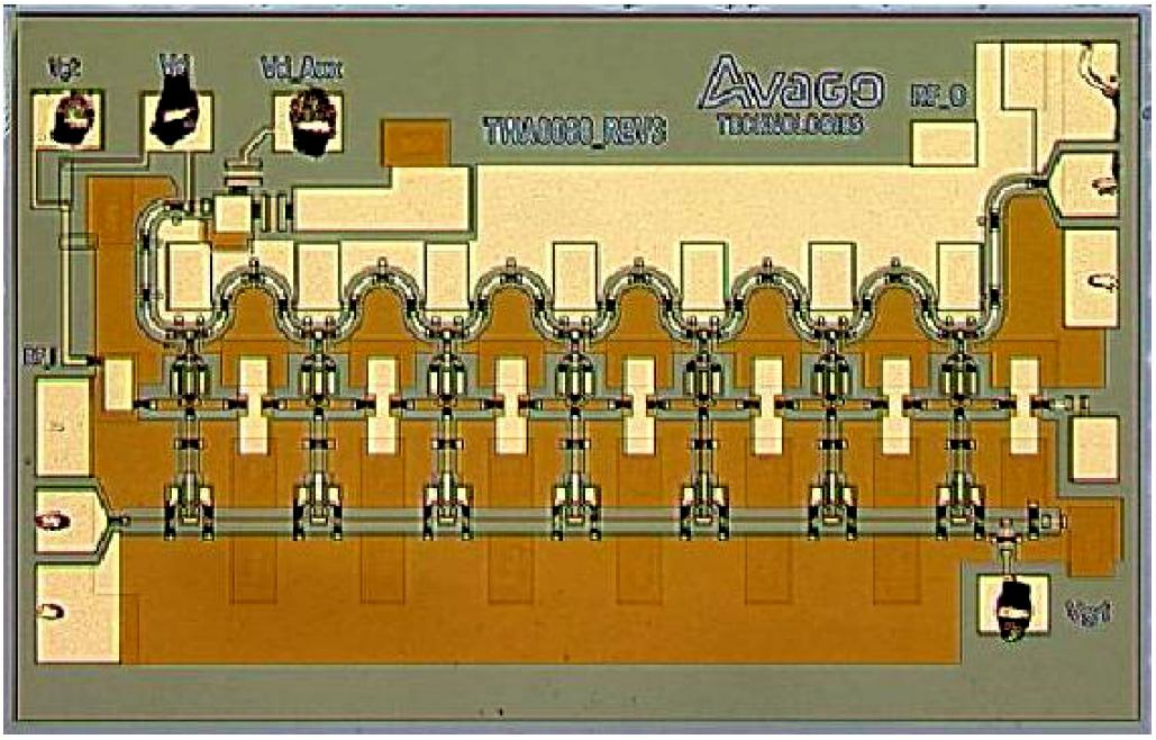

Fig. 2 Monolithic microwave integrated circuit (MMIC) which operates at 85GHz (dimensions are 1.6mm by 1.0mm).

for interconnects. The passives in this case are thin-film TaN resistors, capacitors with Si_3N_4 thin film interlayer dielectric, and inductors are Au spirals. This monolithic microwave integrated circuit (MMIC), traveling wave amplifier operates from DC up to 85 GHz. The cost of producing MMIC modules exceeds that of a standard RF circuits,

especially when highly advanced electron beam lithography for sub-micron gates are utilized that typically result in lower circuit yields than standard silicon processing. Therefore, an intermediate-level integration approach is necessary to bridge the gap between SMT passives and monolithically integrated passives.

Ulrich and Schaper [**3**] have elucidated technology and business model hurdles requiring savvy solutions to enable the benefits of passive component integration. The key reasons to integrate passives include reduced system mass, footprint and cost, improved electrical performance and reliability, and increased design flexibility [**3**]. With SMT's, the passive component values vary substantially offering this design flexibility. For example, capacitors range from less than 100pF to tens of uF's and inductors from 1nH to hundreds of uH's. Given that, for example, the existing i-phone active chip footprint total area is approximately the same as the passive component area, one could assume that the passives could be overlaid onto the active chips to cut the total circuit board area in half. Integration of the passives beyond surface mount technology requires embedding the passives into the substrate beneath the active chips. A technique to do this is to use an interposer layer or material that can house the active chips and in which passives can be fabricated. Materials such as benzocylobutene (BCB) and SiO_2 are used as the capacitor dielectric layer, and could be potentially used as an interposer layer. However, these materials are not photosensitive and can only be defined lithographically using other resists or sacrificial etch layers. A more advantageous approach is to use photosensitive, epoxy-based SU-8 which can be lithographically patterned with high aspect ratio results and anisotropic features. The SU-8 can be used as an electroplating form, an etch mask, and a dielectric layer. It thus serves as an ideal

interposer layer to embed active chips, and build interconnect vias and passives fabricated within the SU-8. This concept is illustrated in Fig. 3 where active chips are

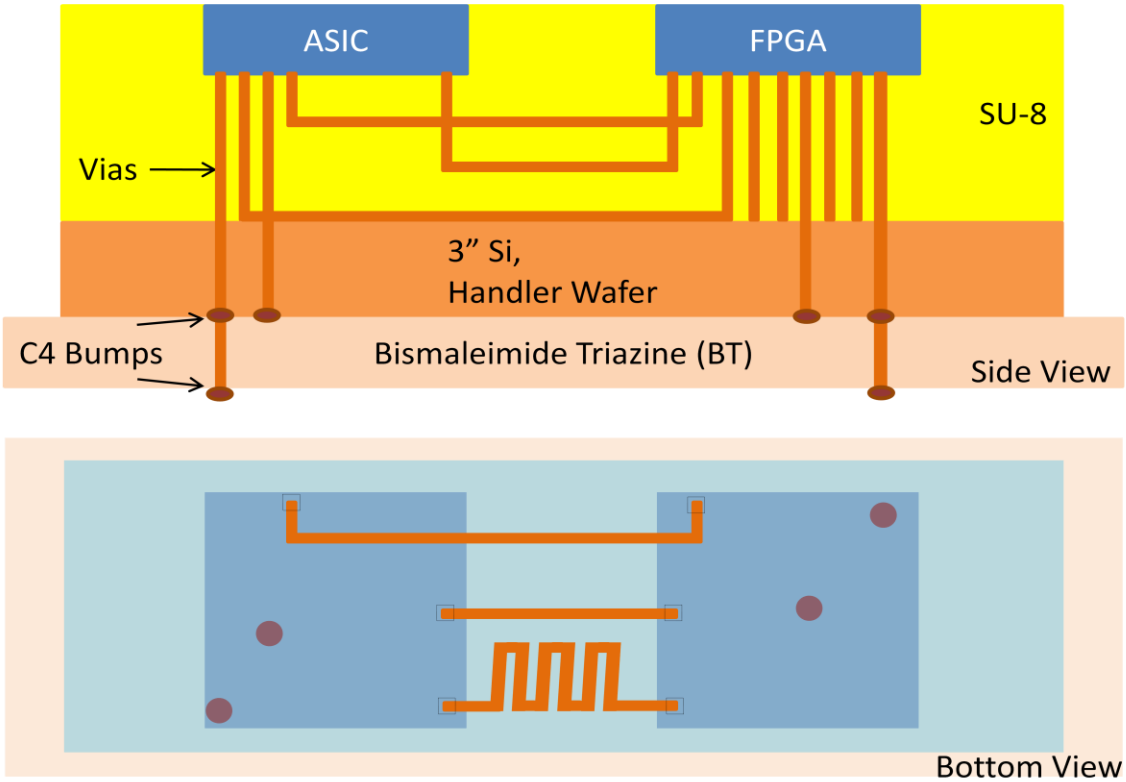

Fig. 3 Side and bottom views of embedded active and passive components in SU-8 interposer layer.

embedded into the SU-8 after vias and passive inductors are fabricated in the SU-8. The silicon handling wafer in this case will be mounted to a bismaleimide triazine (BT) substrate for final mounting to a printed circuit board (PCB) after encapsulation of the SU-8 region.

B. Gaps in existing capabilities

The huge gap in technology requires inductors with enhanced inductance values and high quality factor, yet a small footprint. The key figures of merit for integrated inductors are inductance (L), quality factor (Q), and the frequency at maximum Q, f_{max} at Q_{max}. To accomplish this task, accurate modeling is required as well as optimized

material properties of ferromagnetic materials acting as the magnetic field confining media. Should this gap be bridged, the major advantages listed above as well as the ability to specify an exact inductance value for a given circuit element, will significantly enhance circuit design capabilities and quality.

C. Objectives

There are three main objectives to be addressed in this dissertation. First, a better understanding is necessary of the effects of geometry on the key figures of merit, (inductance, quality factor and frequency at peak quality factor), for integrated solenoid inductors fabricated in an SU-8 interposer layer. Second, a method of fabricating solenoids with enhanced ferromagnetic cores should be developed, and a particular film, acting as the core, studied to determine its magnetic characteristics. Finally, the viability of SU-8 acting as an interposer layer for solenoids and active chips, through integration of these components on a silicon wafer, would lead to the possibility of rapid prototyping of 3-D circuits.

Next, to better understand the factors affecting the key figures of merit for integrated solenoids, the electromagnetic theory describing how these factors are derived is covered.

II. Electromagnetic Design Theory

The following section will discuss the development of the electromagnetic design theory as it applies to the simplest case of the inductance of a round wire filament. This theory is then extended to illustrate the inductance of a straight rectangular wire, the mutual inductance of two straight rectangular wires, the total inductance of a spiral inductor and a solenoid inductor, and finally the addition of a ferrite core to the solenoid. Presently, solid-state circuit designers incorporate square spiral planar inductors into RF integrated circuit low-noise amplifiers and mixers to optimize circuit parameters such as frequency response and center frequency tune. As operating frequencies increase, inductor value accuracy becomes even more important. Circuit models require accurate expressions for the inductance whether obtained from physics-based closed-form expressions, full or partial solutions of Maxwell's electromagnetic equations, current sheet representations, axial filament geometric mean distance (GMD) approximations, or monomial expressions from fitted data. Most of these techniques decompose the spiral into segments and take advantage of partial element equivalent circuit (PEEC) theory [**4**], which allows for inductance calculations of open-loop inductor segments. Rosa, in 1908, was one of the earliest developers of inductance formulas for linear conductors [**5**] through the application of the empirically derived Biot-Savart law. He points out that the self-inductance of an unclosed circuit has never been measured, but the self-inductance of an element is simply a "portion" of a closed circuit which can be measured.

A. Round Wire Filament

As a starting point, it is essential to understand how the magnetic flux surrounding a wire is determined. For the wire shown in Fig. 4 with uniform, time-independent

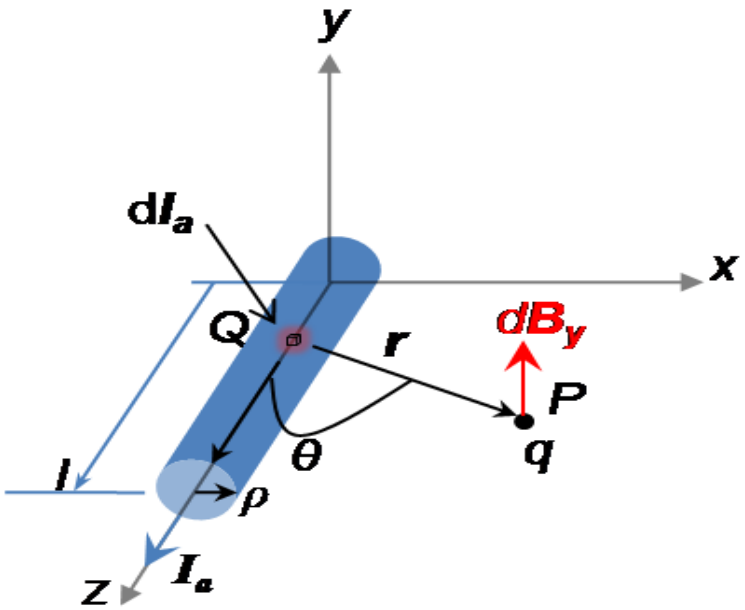

Fig. 4 Differential magnetic flux density at a point *P* outside a wire filament of length *l* and radius *ρ* due to moving charge *Q* or current of length dl_a.

current I_a, the differential magnetic flux density or magnetic field (dB_y) at a point *P* "outside" the wire, is given by the differential form of the empirically derived Biot-Savart law [**6**]:

$$dB_y = \frac{\mu}{4\pi}\frac{I_a\, dl_a\, sin\theta}{r^2} \tag{1}$$

where the angle θ is in the *xz*-plane, ρ is the wire radius which is assumed to be infinitesimal in comparison with the length *l*, and μ is the permeability of the material through which the flux passes. By integrating all of the infinitesimal filaments along the current path such that the vector ***r*** always points from the unit of moving charge (*Q*), to

the reference point *P*, the total magnetic flux density or magnetic field (B_y) can be determined. The geometry of the problem has been simplified by assuming the current flowing through the wire can be represented as the current through an extremely thin wire. This assumption reduces the integration from a 3-fold integral to a 1-fold integral in the *z*-direction which produces a magnetic field in the *y*-direction at the intersection of the positive *xz*-plane:

$$B_y = \frac{\mu I_a}{4\pi} \int_0^l \frac{dl_a \, sin\theta}{r^2}. \tag{2}$$

This result can also be represented in Fig. 4 as the magnetic force produced by the current (steadily moving, time-independent charge (Q) having velocity, v_z) in the filament and exerted on a reference charge q located at point *P*, where the magnetic force (F_y) is:

$$F_y = B_y I_a l = B_y Q v_z. \tag{3}$$

(3) indicates that a current moment ($I_a l$) is equivalent to a charge with velocity (Qv_z). It should be noted that the total force exerted on q includes the other component of the electromagnetic field, the electric field (E), which is Eq and is consistent with Lorentz's force equation. The solution of (2) is:

$$B_y = \frac{\mu I_a}{4\pi} \left[\frac{l - z}{x\sqrt{x^2 - (l - z)^2}} + \frac{z}{x\sqrt{x^2 + z^2}} \right] \tag{4}$$

and this result is plotted in Fig. 5 for a current of 1mA and the case where the wire is in vacuum ($\mu=\mu_0$). The physical reality of this situation is important to examine. At each end of the filament, where z is 0 or l, the magnitude of the field decreases faster than for

positions near the middle length of the wire. Also when *x* approaches infinity, the field also drops to zero. However, as one gets closer to the wire the field rapidly increases. Within the wire, the field drops linearly as a function of *x* according to

$$B_y = \frac{2Ix}{\rho^2}. \tag{5}$$

The plot in Fig. 5 illustrates the situation where ρ is 1μm, and x goes from 1 to 100μm's.

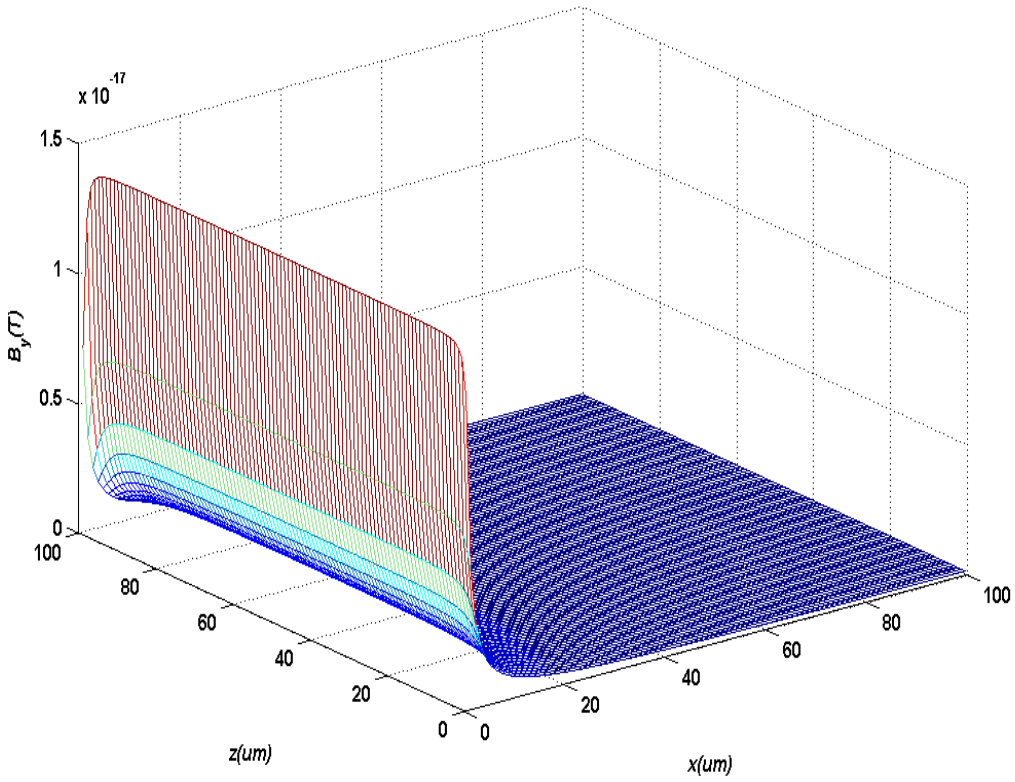

Fig. 5 Magnetic flux magnitude versus *xz*-position relative to 100 μm wire filament located along the *z*-axis.

The magnitude of the magnetic field is directly related to the inductance of the wire and the interaction of the field with its surrounding environment.

The inductance (L) of a circuit element is defined as the magnetic flux (Ψ_m) linking the current (I) generating the magnetic field, and is given by:

$$L = \frac{\Psi_m}{I}, \tag{6}$$

and

$$\Psi_m = \iint \boldsymbol{B} \cdot d\boldsymbol{S}, \tag{7}$$

where $\boldsymbol{B}$ is the magnetic flux density in vector form, and $d\boldsymbol{S}$ is the differential area through which the flux flows. For the wire of Fig. 4, there are two inductance values, which combined, produce the total inductance. The first is the internal inductance resulting from the interaction of the magnetic flux within the radius of the wire itself. The second is the external inductance due to the flux interaction with the medium outside the wire. The determination of L requires integration of the product of B_y with a differential area inside and outside the wire, dS_y. For the internal inductance, the surface integral limits are from 0 to ρ for the x-direction and from 0 to l for the z-direction. For the external inductance, the limits of the surface integral are from 0 to ∞ for the x-direction and from 0 to l for the z-direction. The geometry of this integration is illustrated in Fig. 6 where the magnetic field is only in the y-direction, but is a function of x and z. The result of this integration is the following equation [**5**]:

$$L = L_{int} + L_{ext} = \frac{l\mu_w}{2} + 2\mu_m \left[l * log\left(\frac{l + \sqrt{l^2 + \rho^2}}{\rho} \right) - \sqrt{l^2 + \rho^2} + \rho \right] \tag{8}$$

where μ_w is the wire permeability and μ_m is the permeability of the medium in which the wire is placed. This equation is routinely used to represent the inductance of round wires that are not in close proximity (i.e. $l >> \rho$). However, in reality, with shrinking geometries, this equation must be used with discernment.

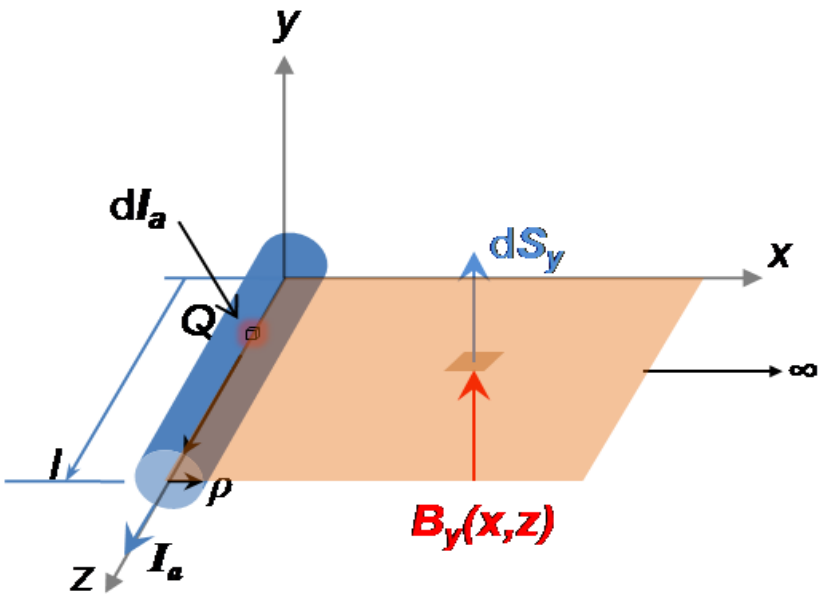

Fig. 6 Magnetic flux density generated by moving charge *Q* and the flux intersection with the differential area in the infinite plane of width *l*.

B. Straight rectangular wire: magnetic flux and vector potential

The next step towards building the necessary equations to represent the inductance of rectangular cross-sectioned metal circuit traces, which serve as the building blocks for spiral and solenoid shaped inductors, is to determine the inductance of a straight rectangular wire. The inductance of a straight wire, either circular or rectangular in cross-section, would seem to be a simple value to calculate, however the six-fold integral which results from the application of the Biot-Savart law has never been solved in closed-form. The closest approximation to a closed-form solution involves the assumption that all of the current flowing through the wire cross-section is in an infinitesimal filament at the center of the cross-section. As in the previous section, it is necessary to find the magnetic flux generated by the charge moving through the

conductor, and then calculate the resulting flux interaction with the conductor and its surrounding medium. Consider the rectangular trace of Fig. 7 with uniform current

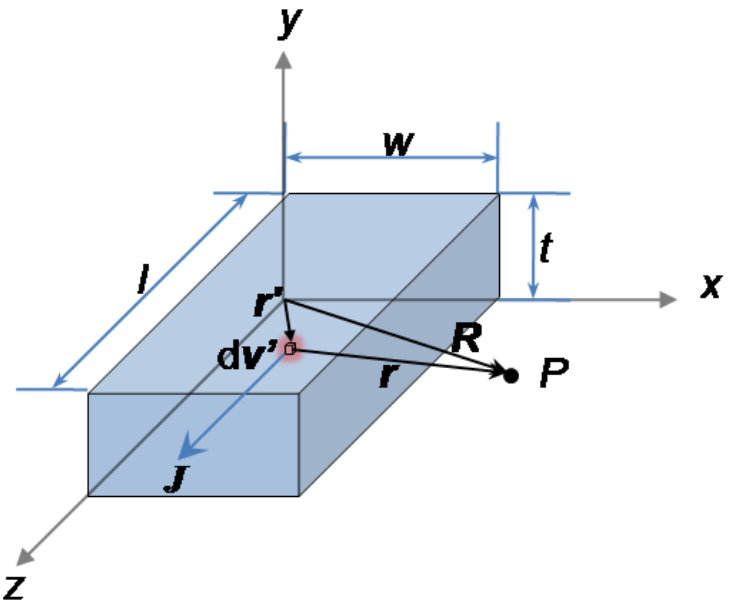

Fig. 7 Rectangular trace of finite width and thickness with uniform current density *J*.

density ***J***, finite width *w*, thickness *t*, and length *l*. The magnetic field at any point *P* is given by:

$$\boldsymbol{B} = \frac{\mu}{4\pi}\int_0^l\int_0^w\int_0^t \frac{\boldsymbol{J}\times\hat{\boldsymbol{r}}}{|\boldsymbol{r}|^2}\,dv', \tag{9}$$

where the location of the differential volume element of current, dv', is located within the conductor by the vector $\boldsymbol{r}'$, and $\hat{\boldsymbol{r}}$ is a unit vector pointing from dv' to *P*. $\hat{\boldsymbol{R}}$ and $\hat{\boldsymbol{r}}'$ are unit vectors pointing from the origin to *P* and dv', respectively. The difficulty in evaluating this integral can be noted by expanding its components. For the cross-product term, $\hat{\boldsymbol{r}}$ can be represented as the vector $(\hat{\boldsymbol{R}} - \hat{\boldsymbol{r}}')$ and $\boldsymbol{r}$ as the vector $(\boldsymbol{R} - \boldsymbol{r}')$. For the

assumption of uniform current density in the z-direction, the magnitude of $\boldsymbol{J}$ can be brought in front of the integral which results in the following integration:

$$\boldsymbol{B} = \frac{J\mu}{4\pi}\int_0^l\int_0^w\int_0^t \frac{\hat{\boldsymbol{z}}\times(\widehat{\boldsymbol{X}}-\widehat{\boldsymbol{x}}')+\hat{\boldsymbol{z}}\times(\widehat{\boldsymbol{Y}}-\widehat{\boldsymbol{y}}')}{[(X-x')^2+(Y-y')^2+(Z-z')^2]}dx'dy'dz'. \tag{10}$$

This integral has never been solved in closed-form, but it can be solved through numerical approximation.

The other method of determining the magnetic flux is to utilize Maxwell's equation $\boldsymbol{\nabla}\cdot\boldsymbol{B}=0$ which indicates that all magnetic fields are solenoidal and converge onto themselves. This fact leads to the definition of the vector potential $\boldsymbol{A}$ defined by $\boldsymbol{B}=\boldsymbol{\nabla}\times\boldsymbol{A}$. The vector Poisson's equation is the differential equation which governs the solution of Maxwell's equations and as such, the solution of the vector potential [**7**]. The vector Poisson's equation is:

$$\nabla^2\boldsymbol{A} = -\mu\boldsymbol{J}. \tag{11}$$

The technique for solving this equation, and thus the vector potential, involves the use of the dyadic Green function $\overline{\boldsymbol{G}}$ (see [**7**] for a description of this function and its utility in solving the Poisson equation). The resulting solution for the vector potential is the following:

$$\boldsymbol{A} = \frac{\mu}{4\pi}\int_0^l\int_0^w\int_0^t \frac{\boldsymbol{J}}{|\boldsymbol{r}|}dv', \tag{12}$$

which for the case at hand can be expanded to:

$$\boldsymbol{A} = \frac{J\mu}{4\pi}\int_0^l\int_0^w\int_0^t \frac{\hat{\boldsymbol{z}}}{[(X-x')^2+(Y-y')^2+(Z-z')^2]^{1/2}}\,dx'dy'dz'. \tag{13}$$

This integral, though appearing simpler than (10), also has never been solved in closed form. Note however, that there is only one component of $\boldsymbol{A}$ in the z-direction, and using Stoke's Theorem, the magnetic flux can be calculated using

$$\Psi_m = \oint \boldsymbol{A}\cdot d\boldsymbol{l} \tag{14}$$

where d$\boldsymbol{l}$ is a differential length along the wire in the direction of $\boldsymbol{J}$.

Again, for the rectangular conductor, a simplification is necessary to achieve expressions for the inductance of the wire. This is accomplished by considering first the mutual inductance between two adjacent wires and then using the axial filament approximation. The mutual inductance of a wire with itself then becomes the wire's self inductance. The equation which defines this mutual inductance is called Neumann's formula which is described below.

C. Rectangular Wire Inductance

1. Two parallel, straight rectangular wires: axial filament approximation

The two partial element equivalent circuits of Fig. 8 have uniform cross-sections and carry uniform currents I_a and I_b. For time independent conditions where a static current flows through the wires and each produces a magnetic field which exerts a force on the other wire the mutual inductance between two current carrying circuit loops can be calculated by applying the solution of the vector potential from above. In this case, the

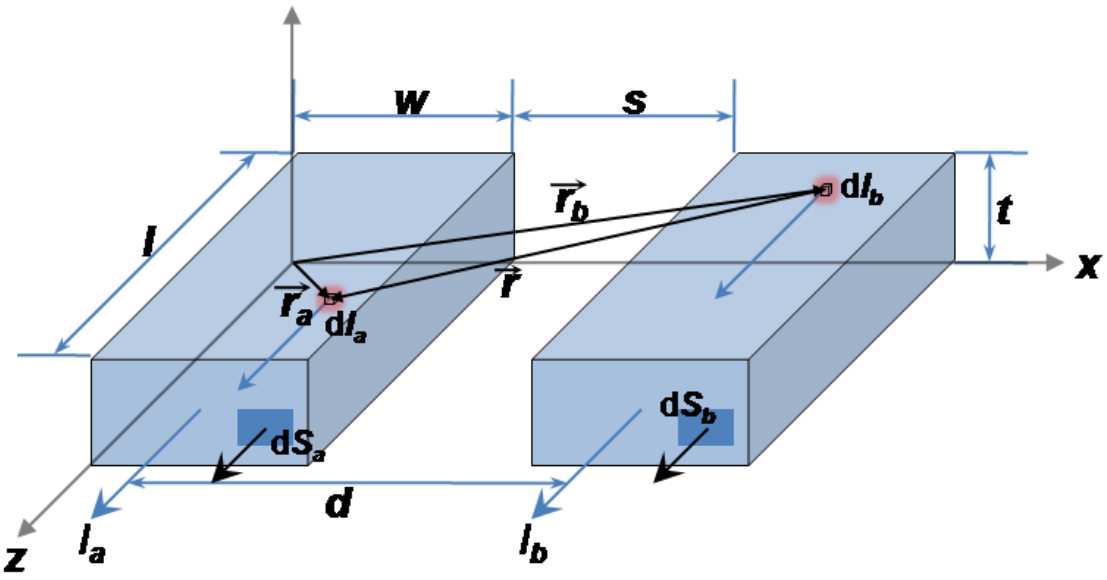

Fig. 8 Two partial element circuits of rectangular cross-section carrying equal, uniform currents.

vector potential produced by current element dl_b of circuit *b* is given by:

$$\boldsymbol{A}_{ab} = \frac{\mu I_b}{4\pi S_b} \oint_0^l \int_0^w \int_0^t \frac{dl_b dS_b}{r} \hat{\boldsymbol{z}} \tag{15}$$

with r being the magnitude of the vector pointing from the current element in circuit *b* to a position in circuit *a*, or $|\boldsymbol{r}_b - \boldsymbol{r}_a|$, and $\mathrm{dS_b}$ is a differential area on the cross-sectional area $S_\mathbf{b}$ orthogonal to the *z*-axis within the volume of circuit *b*. The average magnetic flux then in circuit *a* generated by circuit *b* is found by using (14) as follows:

$$\Psi_{ab} = \frac{1}{S_a} \iint \left[\oint \boldsymbol{A}_{ab} \cdot d\boldsymbol{l}_a \right] dS_a = \frac{\mu I_b}{4\pi S_b S_a} \int_0^l \int_0^l \int_0^w \int_0^t \int_0^w \int_0^t \frac{dl_a dl_b dS_b dS_a}{r} \tag{16}$$

and the mutual inductance is then simply (16) divided by the current I_b according to (6):

$$M_{ab} = \frac{\mu}{4\pi w^2 t^2} \int_0^l \int_0^l \int_0^w \int_0^t \int_0^w \int_0^t \frac{dl_a dl_b dS_b dS_a}{r} \tag{17}$$

where μ is the permeability of the wires. Here significant difficulties arise in evaluating all six integrals since $\vec{r}$ is a function of *x*, *y*, and *z*. The axial filament approximation considerably simplifies this integral, but requires three assumptions: 1) uniform current flows through each conductor, 2) each conductor reduces to a filament of wire representing the entirety of the current in the conductor, and 3) the filaments are separated from one another by the geometric mean distance GMD. As a result, in the limit as the conductor cross-section is reduced to zero, the six-fold integral becomes Neumann's equation expressed as

$$M_{ab} = \frac{\mu}{4\pi}\int_0^l \int_0^l \frac{dl_a dl_b}{r} \tag{18}$$

where the line integrals are evaluated along the closed-loops of circuits *a* and *b* (now treated as filaments). The GMD depends on the geometry being represented. For the rectangular cross- sections of Fig. 8, the GMD is given by the formula [**8**]

$$\ln(GMD) = \ln(d) + \ln(k) \tag{19}$$

where *d* is the center-to-center spacing, and *k*, which depends on the ratios *t*/*w* and *w*/*d*, is found from a table of values in [**8**]. For $w > t$, ln(*k*) is negative and the GMD is less than *d*, and for $w < t$, ln(*k*) is positive and the GMD is greater than *d*. Given this background, the mutual inductance between the two rectangular bars of Fig. 8, calculated using (18) is given by

$$M_{ab} = \frac{\mu}{4\pi}\left[2l\sinh^{-1}\left(\frac{l}{GMD}\right) - 2\sqrt{l^2 + GMD^2} + 2GMD\right]. \tag{20}$$

For two filaments, the mutual inductance is found from (20) where the GMD is the center-to-center spacing of the filaments. To calculate the self-inductance of a rectangular segment, the same formula (20) is used, however the GMD value is determined from a table of values in [**8**] for the self-GMD of a rectangular cross section. This is valid since the mutual inductance of two identical segments becomes the self-inductance of one of the segments as their centers coincide.

Grover provides a full summary of inductance formulas for various geometries as well as filaments with staggered ends and for segments not in the same plane. Some of these formulas will be used to develop the model for the three-dimensional solenoid inductor in a later section. Next, however, a closed-form solution for the inductance between two parallel, straight rectangular wires is presented, and it is compared with the results obtained using the GMD approach.

2. Two parallel, straight rectangular wires: closed form solution

In [**9**], Hoer and Love provide exact closed-form equations for calculation of self- and mutual inductance between parallel rectangular segments of any length, width, height, and separation. The derivation of mutual inductance is first determined for two parallel axial filaments using Neumann's equation. The result is integrated across the width of a thin strip of conductor, and then across the full thickness of a rectangular bar. They obtain an exact formula for the mutual inductance between two rectangular bars of length l_1 and l_2 whose lengths are parallel with the *z*-axis, thicknesses parallel with the *y*-axis and width's parallel with the *x*-axis. Bar l_1 is located at the origin and has width *a*,

and thickness b, whereas bar l_2 has thickness c, and width d. The lengthy equation is presented here:

$$
\begin{aligned}
&M_{l_1 l_2} \\
&= \frac{u_m}{4\pi w^2 t^2}\left[\left[\left[\left(\frac{y^2z^2}{4}-\frac{y^4}{24}-\frac{z^4}{24}\right)x\ln\left(\frac{x+\sqrt{x^2+y^2+z^2}}{\sqrt{y^2+z^2}}\right)\right.\right.\right. \\
&+\left(\frac{x^2z^2}{4}-\frac{x^4}{24}-\frac{z^4}{24}\right)y\ln\left(\frac{y+\sqrt{x^2+y^2+z^2}}{\sqrt{z^2+x^2}}\right) \\
&+\left(\frac{x^2y^2}{4}-\frac{x^4}{24}-\frac{y^4}{24}\right)z\ln\left(\frac{z+\sqrt{x^2+y^2+z^2}}{\sqrt{x^2+y^2}}\right) \\
&+\frac{1}{60}(x^4+y^4+z^4-3x^2y^2-3y^2z^2-3z^2x^2)\sqrt{x^2+y^2+z^2} \\
&-\frac{xyz^3}{6}\tan^{-1}\frac{xy}{z\sqrt{x^2+y^2+z^2}}-\frac{xy^3z}{6}\tan^{-1}\frac{xz}{y\sqrt{x^2+y^2+z^2}} \\
&\left.\left.\left.-\frac{x^3yz}{6}\tan^{-1}\frac{yz}{x\sqrt{x^2+y^2+z^2}}\right](x)_{E+d-a,E}^{E-a,E+d}\right](y)_{P+c-b,P}^{P-b,P+c}\right](z)_{l3+l2-l1,l3}^{l3-l1,l3+l2}
\end{aligned}
\tag{21}
$$

where

$$
\left[\left[[f(x,y,z)](x)_{q_2,q_4}^{q_1,q_3}\right](y)_{r_2,r_4}^{r_1,r_3}\right](z)_{s_2,s_4}^{s_1,s_3}=\sum_{i=1}^{4}\sum_{j=1}^{4}\sum_{k=1}^{4}(-1)^{i+j+k+1}f\left(q_i,r_j,s_k\right).
$$

The value of E is the x-dimension of the innermost yz-surface of l_2; P is the y-dimension of the innermost xz-surface of l_2; and l_3 is the z-dimension of the innermost xy-surface of l_2. Numerical calculation of this equation involves evaluation of singularities which arise due to zero denominators and this slows the computation time considerably. This same formula can be used to calculate the self-inductance of a rectangular bar by setting P=E=l_3=0, a=d, and b=c.

D. Spiral

A spiral inductor shape provides high inductance per area, is a commonly used design, and for on-chip designs is constrained to be planar. The total inductance between two segments of the square spiral planar inductor of Fig. 9 is the sum the self-inductance

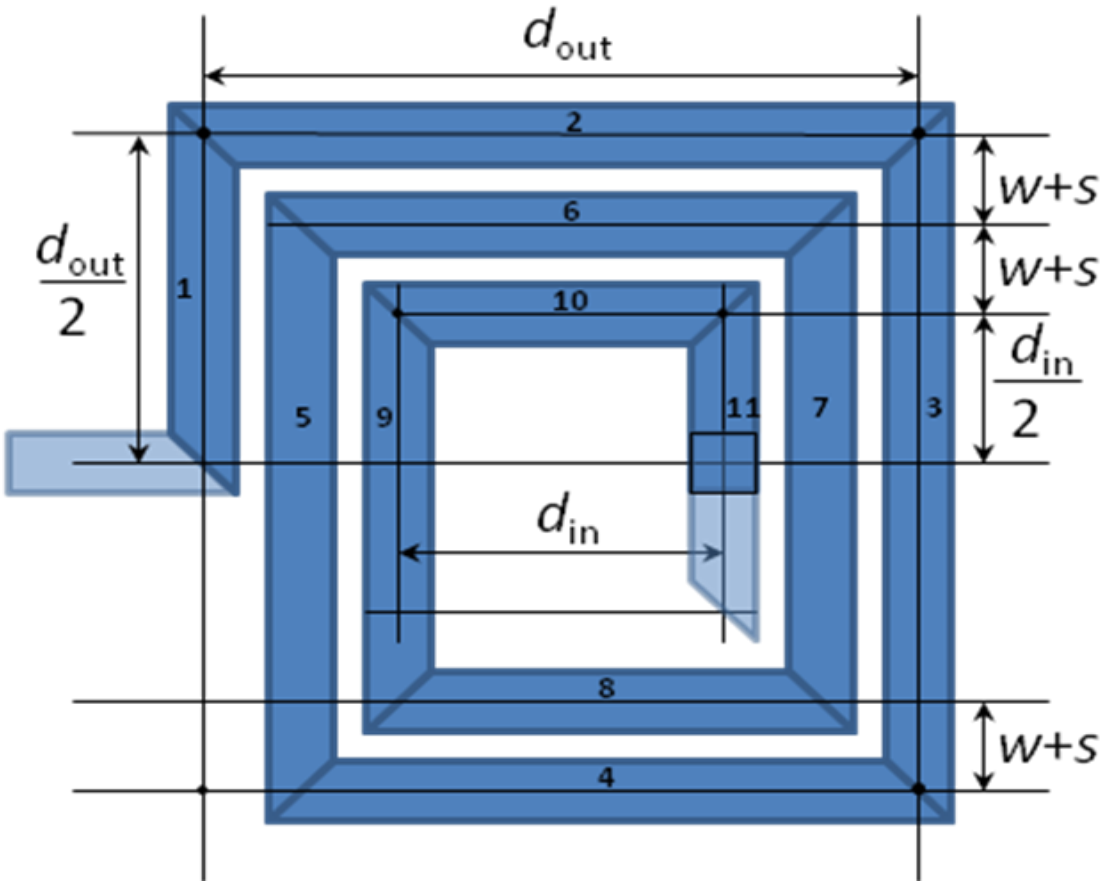

Fig. 9 A 2.5-turn spiral inductor

terms L of each segment and either the positive mutual inductance M^+ term if currents flow in the same direction or the negative mutual inductance M^- term if currents flow in opposite directions. The difficulty with these calculations is in combining all the possible combinations of mutual inductance interactions. For the inductor geometry presented in Fig. 9, there are two complete turns with an additional half-turn (segments 10 and 11) to feed the via and underpass metal. Given N complete turns, there are $4N^2+2N$, M^+ terms,

$4N^2+6N+2$, M^- terms, and $4N+3$, self-inductance terms to evaluate. In 1974, Greenhouse [**10**] developed the first approach to a computer-based solution of the inductance for rectangular geometries as in Fig. 9 to account for all inductance terms. Three general formulas used to represent the self and mutual inductance between spiral turns will be discussed next.

An analysis of the results from spiral inductors fabricated by Kuo [**11**] who used the exact closed-form solution (21) to determine the inductance values is presented in a letter pending publication in Microwave Theory and Techniques entitled, "Comparison of Closed Form Expressions for Square Planar Spiral Inductors" submitted by Fitch and Kazimierczuk. Fig. 10 illustrates the error in the calculation of spiral inductance determined by Jenei's average segment length formula [**12**], the Analysis and Simulation of Inductors and Transformers for IC's (ASITIC) [**13**] simulator, and Hoer's closed-form expression. The ASITIC software utilizes a partial analytical and numerical solution of Green's function to determine the magnetic potentials for the circuit elements. It also employs Week's [**14**] method to account for high frequency skin and proximity effects in the conductors, which greatly affects the current distributions within the inductor and adjacent metal components, such as a ground plane, to give a more accurate inductance value and quality factor.

The primary result is that error increases in representing the inductance as the width of the conductor increases and as the separation between the conductor's increases. Jenei's formula, which over-simplifies the overall calculation of inductance, results in significant errors, and should be used with caution. The axial filament approximation results in less error except when the width and or the separation between turns are large.

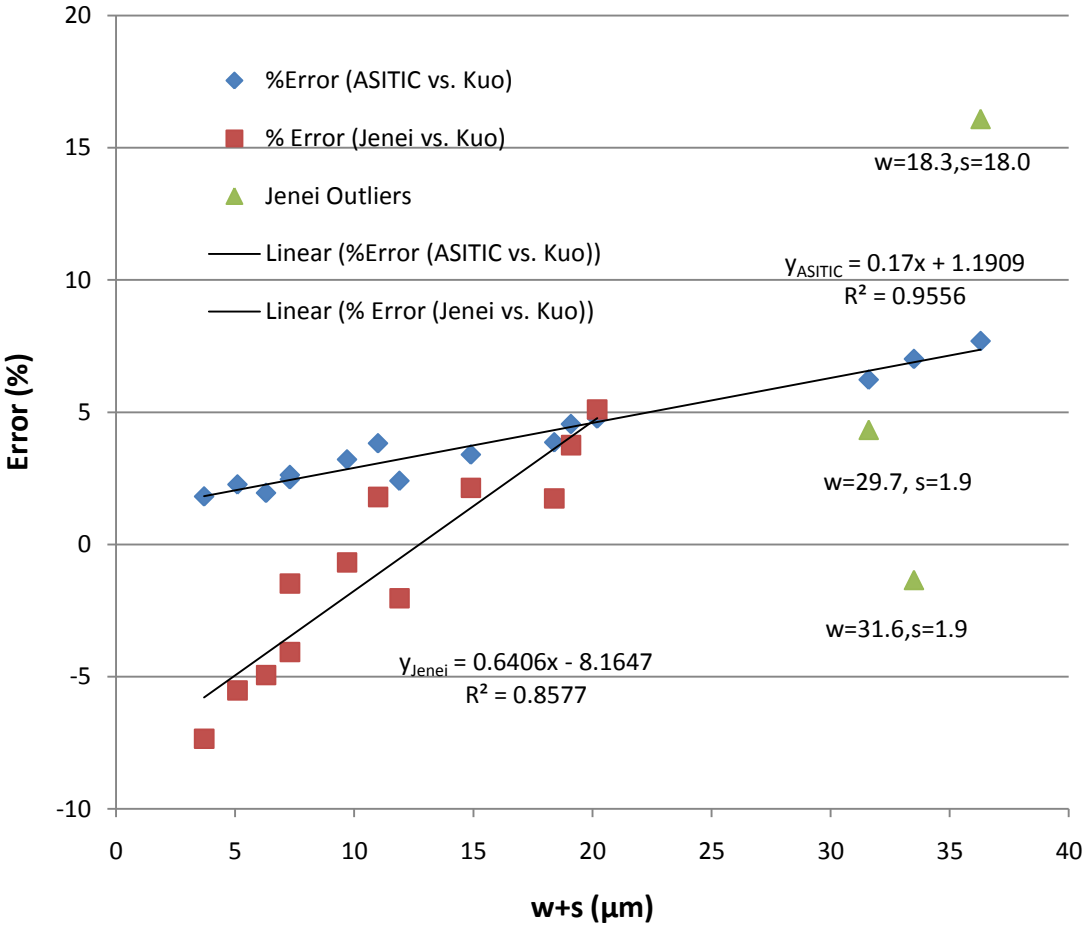

Fig. 10 ASITIC and Jenei's inductance error versus segment width plus spacing versus Kuo's measured values.

E. Solenoid

The preceding development provided the necessary theory behind calculating the inductance of rectangular metal traces which are the primary building blocks for inductor model design. The next component branches into 3D design, and is the solenoid geometry, which confines the magnetic flux within the volume along the central axis of the turns (each turn adds to the magnetic flux and L is proportional to N^2 and the area of the loop). Bayraktaroglu [**15**] demonstrated a quality factor of 25 and 2nH inductance at 6GHz for an air-core solenoid fabricated in gold-turns. The solenoid layout is conducive

to adding a ferrite or ferromagnetic core and as such to studying the magnetic characteristics of the core material to enhance the inductance and quality factor. The next major section describes the development of the solenoid model.

F. Ferromagnetic Core

The solenoid core is ideally comprised of a magnetic material which has a large permeability to enhance the overall inductance, and minimal conductivity to reduce proximity effects (eddy currents) and provide a high quality factor. Characterization of $Ni_{16.3}Fe_{83.7}$ core (a soft ferromagnetic material having large permeability) has been accomplished in [**16**] with results that indicated a 20% increase in inductance at 100MHz. The real part of the effective permeability for NiFe was determined through transmission line measurements to be near 300 at 100MHz [**17**]. The ferromagnetic resonance of NiFe was determined to be near 2.1GHz. In [**18**] FeCoAl thin films were studied and determined to have a permeability around 1000. In a later section, FeCoAl-core solenoid inductors are fabricated and characterized.

The next section utilizes the self and mutual inductance, closed-form equations derived in this chapter as building blocks of a model describing the frequency dependent behavior of the solenoid inductor. Also included are the other essential elements of capacitance and resistance, which when combined with inductance, more accurately represent the electromagnetic nature of the solenoid.

III. Hybrid Inductor Model Design

A. Introduction

There has been considerable effort placed on the development of on-chip spiral inductors for design of advanced CMOS communication circuit components such as the low-noise amplifier, mixer and high frequency amplifier. Additionally, evaluation of on-chip solenoid inductors is gaining momentum due to advances in MEMS technology. Fang presents a detailed model for high-Q MEMS solenoid inductors which accounts for inter-winding capacitance, substrate loss and self-resonance loss [**19**]. However, the model presented does not include the effects of increasing frequency on the solenoid inductance. This section presents a model to include the effects of frequency on solenoid inductors fabricated in an SU8 interposer layer. Inductors are characterized based upon the solenoid geometry as well as physical properties of the metal traces and SU8. Additionally, the model indicates that inductance values are significantly enhanced with the incorporation of ferromagnetic core materials with low conductivity values.

B. Solenoid Inductor Geometry

The solenoid inductor consists of parallel vertical posts, and parallel and anti-parallel horizontal spans as illustrated in Fig. 11. The variables defining the geometry are shown as spacing's and thicknesses. The spacing's are center-to-center distances either between posts *W* and *D*, or between spans *H*. The width of posts and spans is *w*, the depth of posts is *d*, and the thickness of spans is *t*. Additionally, it is assumed the vertex

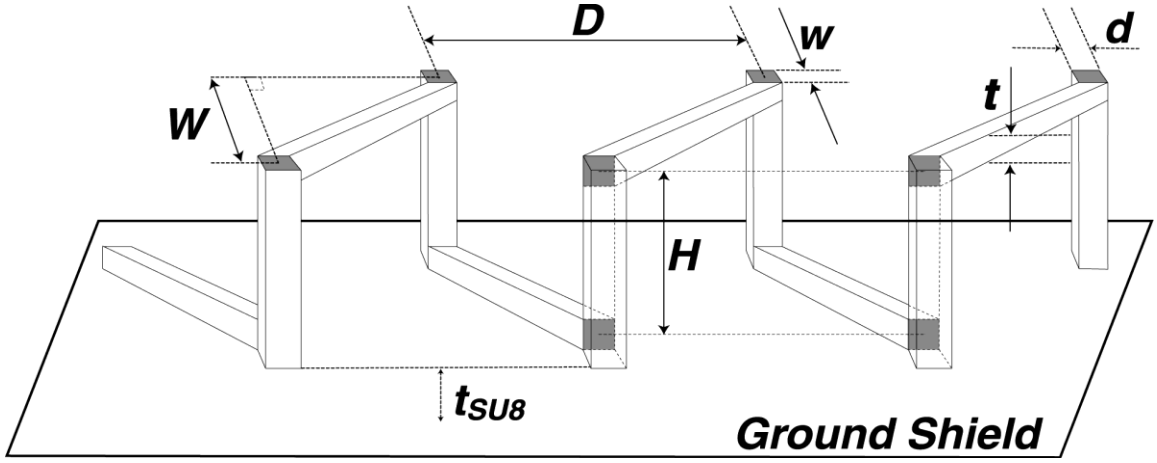

Fig. 11 Characteristic dimensions for basic solenoid geometry positioned above a ground shield.

angles between spans are equal for all turns and that posts are evenly distributed in increments of one-half of *D* such that adjacent top and bottom posts form a perfect isosceles triangle.

C. Closed-Form Inductor Model

1. Solenoid Inductance Calculations

The solenoid inductance is calculated from closed-form expressions for the inductance of rectangular metal traces obtained from Grover [**8**]. These formulas are based on an axial filament approximation and the use of the geometric mean distance between filaments. The approximation is accurate when the segment lengths are much greater than their center-to-center distance and when the length is much greater than the segment width, thickness or depth.

The framework to calculate the solenoid inductance depends on the variables of Fig. 11, as well as metal permeability, number of turns, operating frequency, segment self-inductance, segment-to-segment mutual inductance, turn-to-turn capacitance, interposer layer permittivity, and metal resistivity (affected by skin and proximity

effects). Additional variables to be included in future model development are magnetic core permeability and permittivity.

The total DC inductance of the solenoid consists of the summation of positive mutual inductance terms, negative mutual inductance terms and self-inductance terms. For posts on opposite sides of the solenoid, the terms are negative, whereas posts on the same side have positive mutual inductance terms. Spans on top/bottom have positive mutual inductance terms with top/bottom spans, whereas spans on opposite levels have negative mutual inductance terms.

The number of segments T in the solenoid is a function of the number of complete turns N:

$$T = 4N \tag{22}$$

There are $2N$ posts and $2N$ spans.

When using the axial filament approach to represent mutual inductance between equal length posts, closed-form expressions differ for geometries where the segments are closely spaced and short/long in length versus distantly spaced and short/long in length. Grover [**8**] provides these closed-form expressions for all cases.

For two parallel, rectangular metal traces of equal length the mutual inductance is given by

$$M_A = \frac{\mu_w}{4\pi}\left[l \sinh^{-1}\left(\frac{l}{s}\right) - \sqrt{l^2 + s^2} + s\right] \tag{23}$$

where l is the length of the segments, and s is their long-axis, center-to-center separation. This axial approximation is accurate when $0.1 \leq {}^{l}/_{s} \leq 10$. For the case when ${}^{l}/_{s} \geq 10$ the following expression is accurate:

$$M_B = \frac{\mu_w l}{4\pi}\left[ln\left(\frac{2l}{s}\right) - 1 + \frac{l}{s} - \frac{1}{4}\frac{l^2}{s^2} + \cdots\right] \tag{24}$$

The last case occurs when ${}^{s}/_{l} \geq 10$ and

$$M_C = \frac{\mu_w}{2\pi}\frac{s}{l}\left[1 - \frac{1}{12}\frac{l^2}{s^2} + \frac{1}{40}\frac{l^4}{s^4} + \cdots\right]. \tag{25}$$

These three equations can be employed to calculate all of the mutual inductance terms for the vertical posts. The top view of the solenoid is shown in Fig. 12 where the angle ζ is

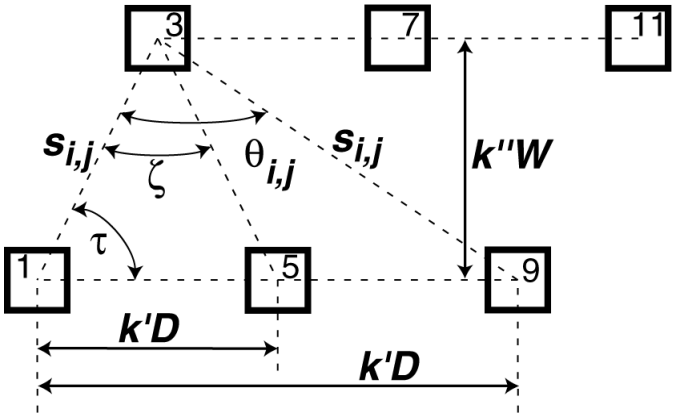

Fig. 12 Geometric configuration of staggered, parallel post segments.

the vertex angle between horizontal spans, and τ is the base angle between a horizontal drawn through the posts on one side of the solenoid and a top or bottom span. For a solenoid with N complete turns, the total mutual inductance contributed by the vertical posts is calculated using the following summations for odd numbered i (where the index i

corresponds to the first segment of the mutual pair and the index *j* corresponds to the second segment of the mutual pair):

$$M_V = \sum_{i=1}^{T-2} \sum_{j=i+2}^{T} (-1)^{k''} M_{Y(i,j)} \tag{26}$$

where $k'' = 1$ if mod[(*i*+*j*)/4]=0, else $k'' = 0$, the subscript *Y* corresponds to the subscript from equation (23), (24), or (25) depending on the ratio l/s, where *l*=*H*, the distance between mutual segments, *s* is given as

$$s_{i,j} = \sqrt{(k'D)^2 + (k''W)^2}, \tag{27}$$

and $k' = (j - i)/4$. The $(-1)^{k''}$ term accounts for negative and positive mutual inductance terms.

The mutual inductance between horizontal spans involves the calculation of parallel and non-parallel segments, and these equations are also provided by Grover. The illustration of Fig. 13 shows the first case of parallel segments in the same plane, but with

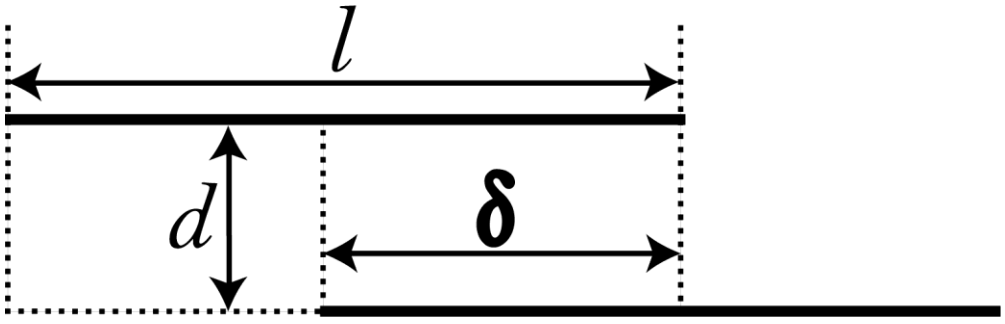

Fig. 13 Top-view of solenoid span geometry and defining angles and separations.

staggered ends. The positive mutual inductance terms are calculated from the following equation [**8**]

$$M_P = \frac{\mu_w}{2\pi}\left[\alpha \sinh^{-1}\left(\frac{\alpha}{s}\right) - 2\beta \sinh^{-1}\left(\frac{\beta}{s}\right) + \delta \sinh^{-1}\left(\frac{\delta}{s}\right) - \sqrt{\alpha^2 + s^2} + 2\sqrt{\beta^2 + s^2} - \sqrt{\delta^2 + s^2}\right] \quad (28)$$

where α=2l+δ, β=l+ δ, and δ is negative for overlapping segments given by

$$\delta = -abs(l - k'D\cos(\tau)). \quad (29)$$

For the rare case that a solenoid has a large vertex angle and sufficient terms that $\theta_{i,j}$ increases to greater than 90°, then δ becomes positive.

For the non-parallel case, Fig. 14 illustrates the geometric configuration of mutual

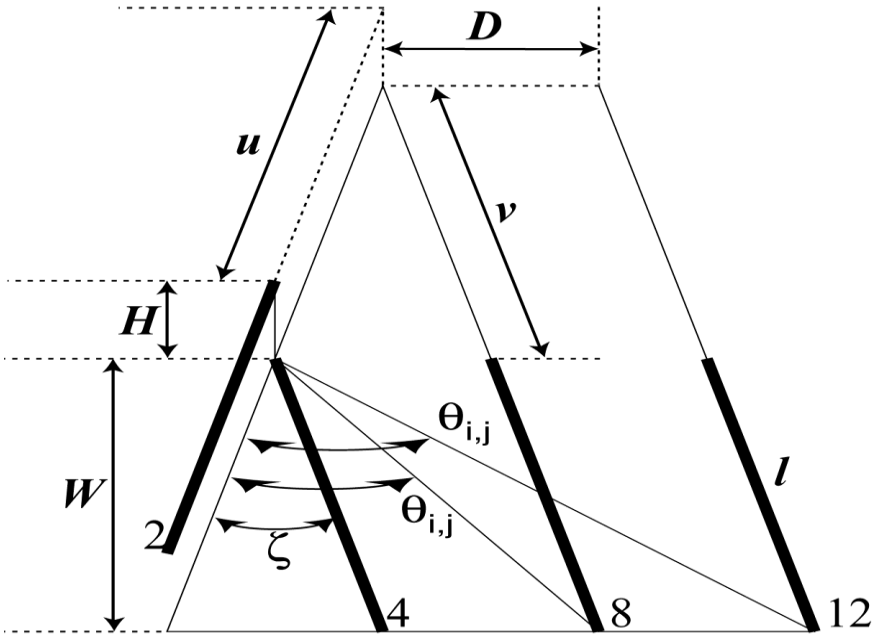

Fig. 14 Geometric configuration for non-parallel, non-coplanar span segments.

segments in two separate planes, for example segments 2 and 8. Grover provides an equation for the mutual inductance for this case as follows:

$$M_{NP} = \frac{\mu_w}{4\pi}\cos\zeta\left[(u+l)\tanh^{-1}\left(\frac{l}{R_1+R_2}\right)+(u+l)\tanh^{-1}\left(\frac{l}{R_1+R_4}\right)\right.$$
$$\left.-u\tanh^{-1}\left(\frac{l}{R_3+R_4}\right)-u\tanh^{-1}\left(\frac{l}{R_2+R_3}\right)\right]-\frac{\Omega h}{\sin(\zeta)} \quad (30)$$

where

$$\Omega = \tan^{-1}\left\{\frac{H^2\cos(\zeta)+(u+l)^2\sin^2(\zeta)}{HR_1\sin(\zeta)}\right\}$$
$$-\tan^{-1}\left\{\frac{H^2\cos(\zeta)+u(u+l)\sin^2(\zeta)}{HR_2\sin(\zeta)}\right\}$$
$$+\tan^{-1}\left\{\frac{H^2\cos(\zeta)+u^2\sin^2(\zeta)}{HR_3\sin(\zeta)}\right\} \quad (31)$$
$$-\tan^{-1}\left\{\frac{H^2\cos(\zeta)+u(u+l)\sin^2(\zeta)}{HR_4\sin(\zeta)}\right\}$$

and

$$R_1^2 = H^2+2(u+l)^2-2(u+l)^2\cos(\zeta), \quad (32)$$

$$R_2^2 = H^2+u^2\,(u+l)^2+u^2-2u(u+l)\cos(\zeta), \quad (33)$$

$$R_3^2 = H^2+2(u)^2-2(u)^2\cos(\zeta), \quad (34)$$

$$R_4^2 = H^2+u^2+(u+l)^2-2u(u+l)^2\cos(\zeta). \quad (35)$$

Additionally, the angle ζ is given by

$$\zeta = 2\tan^{-1}\frac{D}{2W} \quad (36)$$

and *u* and *v* by

$$u = v = (k'-0.5)l. \quad (37)$$

For a solenoid with *N* complete turns, the total mutual inductance contributed by the horizontal spans is calculated using the following summations for even numbered *i*

(where the *i* corresponds to the first segment of the mutual pair and the *j* corresponds to the second segment of the mutual pair):

$$M_H = \sum_{i=2}^{T-2} \sum_{j=i+2}^{T} (-1)^{k'''} M_{X(i,j)} \tag{38}$$

where k'''=1 if mod[(*i*+*j*-2)/4]=0, else k'''=0 to account for the sign of negative (non-parallel segments) mutual inductance and positive (parallel segments) mutual inductance, and the subscript *X* corresponds to the appropriate equation (28) or (30), subscripted by *NP* or *P*. Finally, the self-inductance of the solenoid is provided by the following equation from Rosa:

$$L = \frac{\mu_a}{4\pi} m \left[ln\left\{\frac{2m}{GMD}\right\} - 1 \right] + \frac{\mu_w}{4\pi} GMD \tag{39}$$

such that for spans, *L* is calculated using *m*=*l*, GMD is a function of *d* and *t* and the total span inductance (L_{spans}) is 2*NL*, and for posts, *L* is calculated using *m*=*H*, and GMD is a function of *d* and *w* and the total post inductance (L_{posts}) is 2*NL*.The total solenoid inductance is therefore the sum of L_{spans}, L_{posts}, M_V and M_H.

2. Solenoid Resistance and Capacitance Calculations

The solenoid of Fig. 11 consists of multiple inductances and capacitances between multiple metal segments; capacitances between metal segments and the ground shield; and resistance of the traces. This resistance can increase substantially if the skin effect is included as a factor in the inductor design. Also, the proximity effect, which results in eddy currents in adjacent metal layers, will be considered as a factor in the high frequency resistance.

The capacitance terms are generated by considering the effect of the SU-8 dielectric surrounding the entire coil. For two adjacent vertical posts (numbered 1 and 5) of Fig. 12, the capacitance is given by:

$$C_{1-5} = \frac{\varepsilon_{SU-8} w(H-t)}{D-d}. \tag{40}$$

The capacitance between off-diagonal posts (numbered 1 and 3) is given by:

$$C_{1-3} = \frac{\varepsilon_{SU-8}\sqrt{w^2+d^2}(H-t)}{\sqrt{W^2+\left(\frac{D}{2}\right)^2}}, \tag{41}$$

whereas the capacitance between off-diagonal posts (numbered 1 and 7) is given by:

$$C_{1-7} = \frac{\varepsilon_{SU-8}\sqrt{w^2+d^2}(H-t)}{\sqrt{W^2+\left(\frac{3D}{2}\right)^2}}. \tag{42}$$

Consideration of the capacitance between spans of Fig. 13Fig. 14 involves three configurations: one for interaction between adjacent parallel spans either on the top or the bottom of the solenoid, another for interaction between top and bottom, adjacent anti-parallel spans, and a third for top and bottom, adjacent-turn, anti-parallel spans. The first capacitance (between spans 4 and 8) is given by:

$$C_{4-8} = \frac{\varepsilon_{SU-8} t\sqrt{W^2+\left(\frac{D}{2}\right)^2}}{D-d}, \tag{43}$$

the second (between 2 and 4) is given by:

$$C_{2-4} = \frac{\varepsilon_{SU-8} t\sqrt{W^2+\left(\frac{D}{2}\right)^2}}{\sqrt{D^2-H^2}}, \tag{44}$$

and the third (between 2 and 8) is given by:

$$C_{2-8} = \frac{\varepsilon_{SU-8} t \sqrt{W^2 + \left(\frac{D}{2}\right)^2}}{D}. \tag{45}$$

For a pair of solenoid turns, the capacitance terms are given by the sum of twice of each term numbered 40 through 45.

Finally, the total resistance of the coil consists of the DC and AC portions. The DC resistance is a function of the geometry and the metal resistivity. The trace DC resistance ($R_{w,dc}$) is given by:

$$R_{w,dc} = \frac{\rho_w l_w}{S_w}, \tag{46}$$

where ρ_w is the metal trace or wire resistivity, l_w is the length of the wire, and S_w is the cross-sectional area of the trace. The AC resistance involves much more complicated terms due to the skin effect and proximity effect that lower the fundamental cross-section of the wire trace at high frequency. Grandi et al [**20**] provide an excellent model of laminated core inductors at high frequency with the following terms representing the skin and proximity effects, respectively ($R_{skin,ac}$. and $R_{prox,ac}$). The wire's skin depth δ_w is a function of the metal resistivity, the metal permeability, and the frequency of operation f and is represented by:

$$\delta_w = \sqrt{\frac{\rho_w}{\pi \mu_w f}}. \tag{47}$$

The first AC resistance term ($R_{skin,ac}$) accounts for the skin effect and is given by:

$$R_{skin,ac} = R_{w,dc}A\left[\frac{e^{2A} - e^{-2A} + 2\sin(2A)}{e^{2A} + e^{-2A} - 2\cos(2A)}\right], \tag{48}$$

where A is the geometry dependent quantity given by:

$$A = \frac{t}{\delta_w}\sqrt{\frac{d}{D-d}}, \tag{49}$$

for a span of width d and thickness t separated from adjacent spans by D-d. The second term ($R_{prox,ac}$) accounts for the proximity effect of adjacent turns and is given by:

$$R_{prox,ac} = R_{w,dc}A\left[2\frac{N_l^2 - 1}{3}\frac{e^{A} - e^{-A} - 2\sin(A)}{e^{A} + e^{-A} + 2\cos(A)}\right], \tag{50}$$

where N_l is the number of layers, which for an integrated solenoid is usually only one, therefore this term goes to zero.

3. Summation of Solenoid Parasitic Terms

The inductance, capacitance and resistance equations presented in the previous sections represent the DC values for the solenoid inductor when combined with the proper lumped-element model of the solenoid and surrounding components (ground pads, substrate, etc.). Other terms include the capacitance to ground between the bottom inductor spans, the capacitance to ground between the top inductor spans, and the capacitance between posts and the ground test pads. The solenoid layout is shown below in Fig. 15.

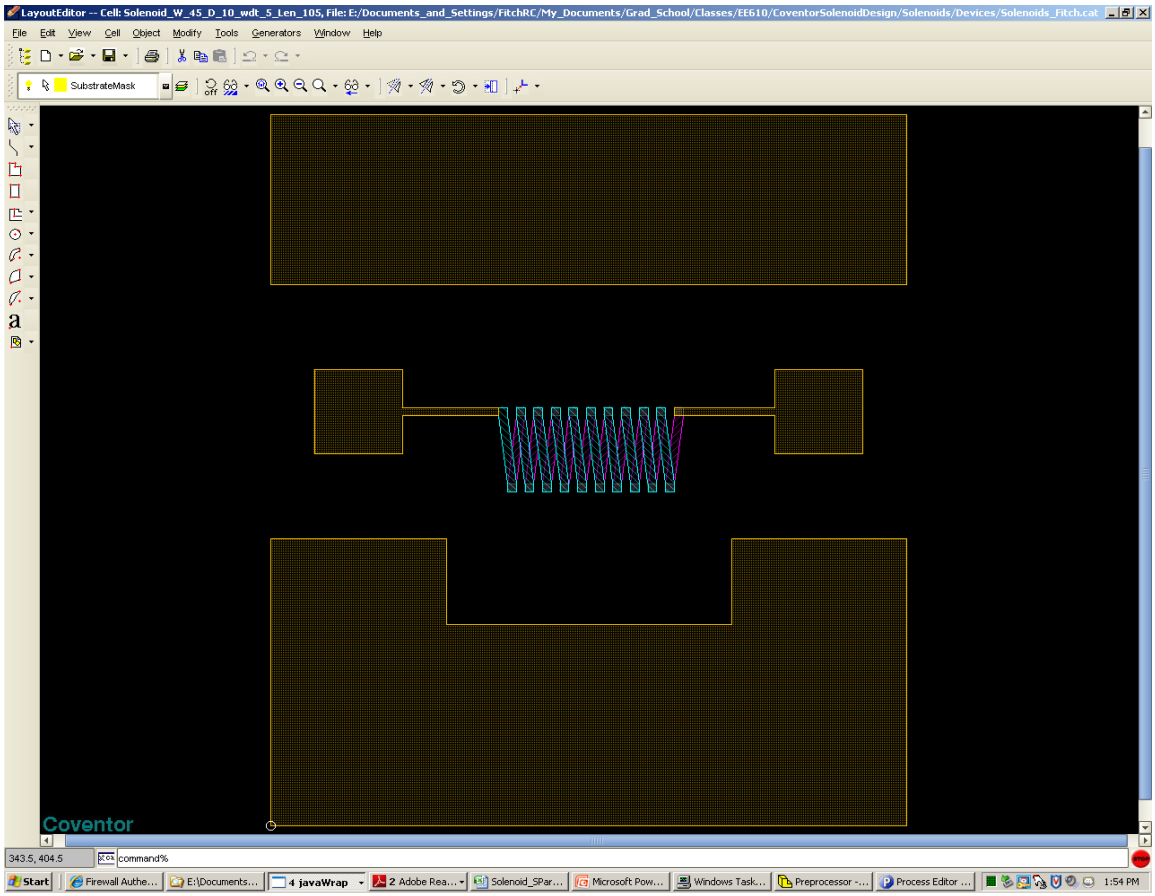

Fig. 15 Solenoid layout with surrounding ground pads (top and bottom) and input and output signal pads.

4. Solenoid DC and AC Equivalent Circuits

The physical layout of the solenoid of Fig. 15 can be represented by the lumped element components placed into a DC circuit model. These lumped element terms are represented in the DC equivalent circuit of Fig. 16. The figure also includes the input and output ports which are designed to be 50 ohms and ultimately whose impedance is extracted from small signal, scattering parameter measurements. This results in determination of the solenoid inductance value independent of the test structure impedance. The only effect of the input and output pads would be a small inductive or

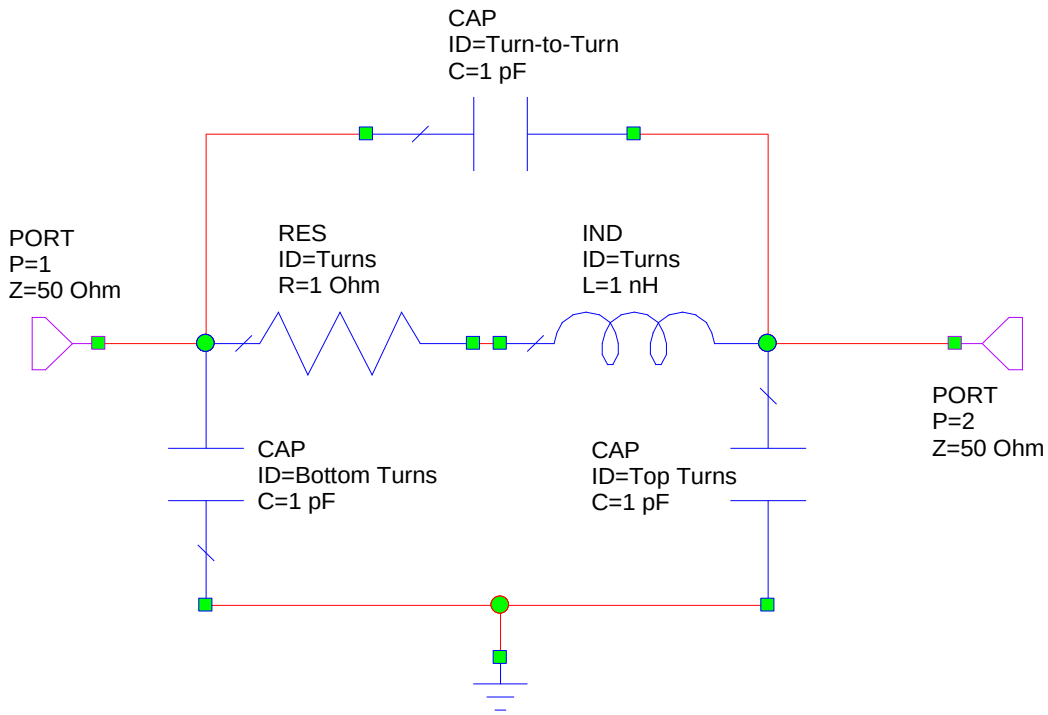

Fig. 16 DC equivalent circuit model for solenoid and test structure with ground pads above substrate ground.

capacitive reactance with the end solenoid turns. Similarly, the large ground pads would interact with the vertical posts at high frequencies.

As the frequency of operation increases, the capacitances of Fig. 16 begin to conduct current and thus start to play a significant role in the overall impedance of the solenoid circuit. The AC equivalent circuit for the solenoid is represented in Fig. 17, which is similar to the model for a spiral inductor presented by Yue [**21**] and solenoid inductor by Fang [**19**]. Fang's model did not account for the frequency dependence of the solenoid's inductance value, which is a shortcoming of the model. This work accounts for the value by evaluating the impedance as a function of frequency. In

addition, the resistor in the model also is a function of frequency due to the proximity effects of adjacent components as well as the skin effect of the metal turns.

5. Solenoid Impedance and Quality Factor

The impedance (Z) of the solenoid circuit of Fig. 17 is comprised of the inductive

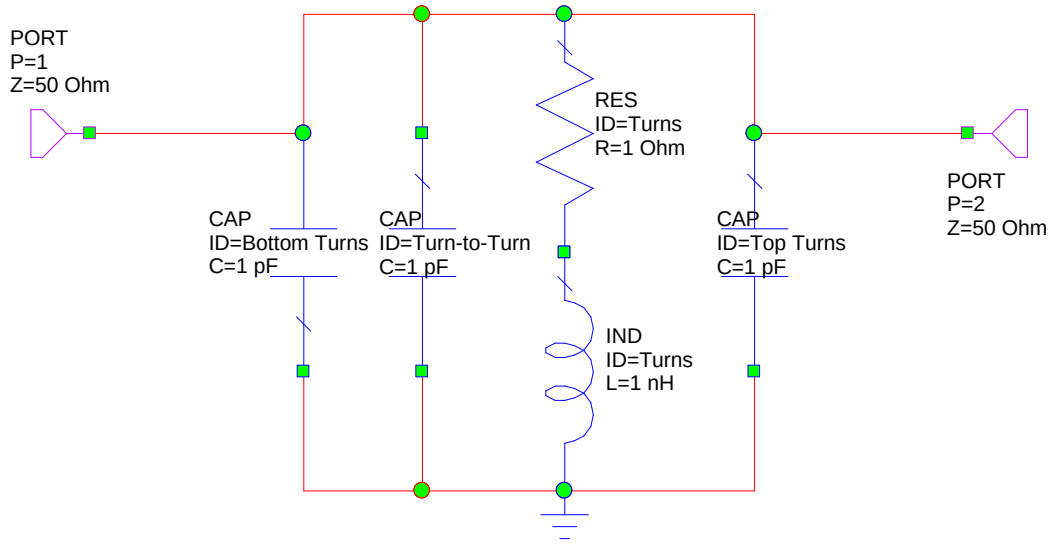

Fig. 17 AC equivalent circuit model for solenoid and test structure with ground pads above substrate ground.

reactance, X_L given by ωL, the capacitive reactance, X_C given by $1/\omega C$ where C is the parallel combination of the capacitances of Fig. 17, and the turn resistance, R. Z is represented by the following expression:

$$Z = \frac{-jX_C(R + jX_L)}{(R + jX_L - jX_C)}. \tag{51}$$

The quality factor Q, given by Fang [**19**]

$$Q = \frac{\omega L}{R}\,(SLF)(\,SRF), \tag{52}$$

includes both a substrate loss factor *SLF*, that is essentially unity for high resistivity substrates, such as borosilicate glass (BSG) or for solenoids with the substrate removed, and the self-resonance factor *SRF*, which is given by:

$$SRF = \left[1 - \frac{\mathrm{R}^2(C_{IS} + C)}{L} - \omega^2 L(C_{IS} + C)\right], \tag{53}$$

where C_{IS} is the substrate capacitance. From the impedance, one can determine the frequency dependent reactance and resistance. For an inductor, this reactance is inductive until the frequency reaches the self-resonance point, at which the quality factor goes to zero, and the reactance turns capacitive. The frequency dependent inductance is therefore calculated by taking the imaginary part of the impedance, Z and the AC resistance is calculated by taking the real part of Z.

The Matlab code for the solenoid model is presented in Appendix A.

6. Solenoid Model Results

In order to verify the quality of the Matlab solenoid model, a design of experiments was performed to evaluate the hypothesis suggesting that closely spaced solenoid turns result in lower inductance values and lower quality factor for a fixed number of turns. The general specifications for a portion of the DOE are shown in Table I where the variation in turn-to-turn spacing (*D*) is the primary variable for the first six designs. For the last five designs, the number of turns was decreased from 10 to 2, and the distance from input to output kept constant at 105 μm's. The inductance versus frequency for the first five designs is shown in Fig. 18. Clearly, the inductance is a strong function of frequency and of the turn-to-turn spacing. The most tightly-spaced

Table I

DESIGN OF EXPERIMENTS EXAMINING SOLENOID TURN-TO-TURN SPACING VARIATIONS

Design	Turns	W(μm)	D(μm)	H(μm)	w(μm)	d(μm)	t(μm)	Length(μm)
1	10	145	10	10	5	5	5	3233
2	10	145	20	10	5	5	5	3240
3	10	145	30	10	5	5	5	3251
4	10	145	40	10	5	5	5	3264
5	10	145	50	10	5	5	5	3281

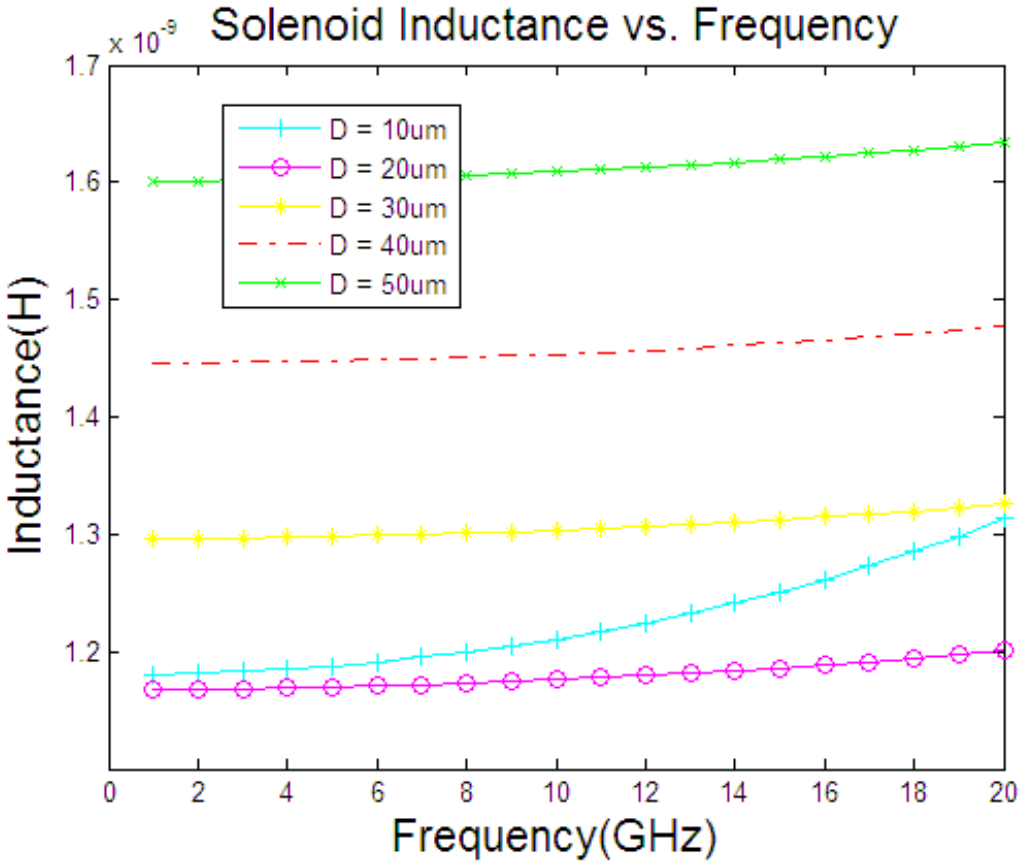

Fig. 18 Inductance versus frequency for the first five solenoid designs of Table I.

inductors exhibit the lowest inductance values, an indication that the capacitance between turns and or the negative mutual inductance between turns dominates the reactance of the

solenoid for this case. For the solenoid quality factor, Fig. 19 illustrates the relationship

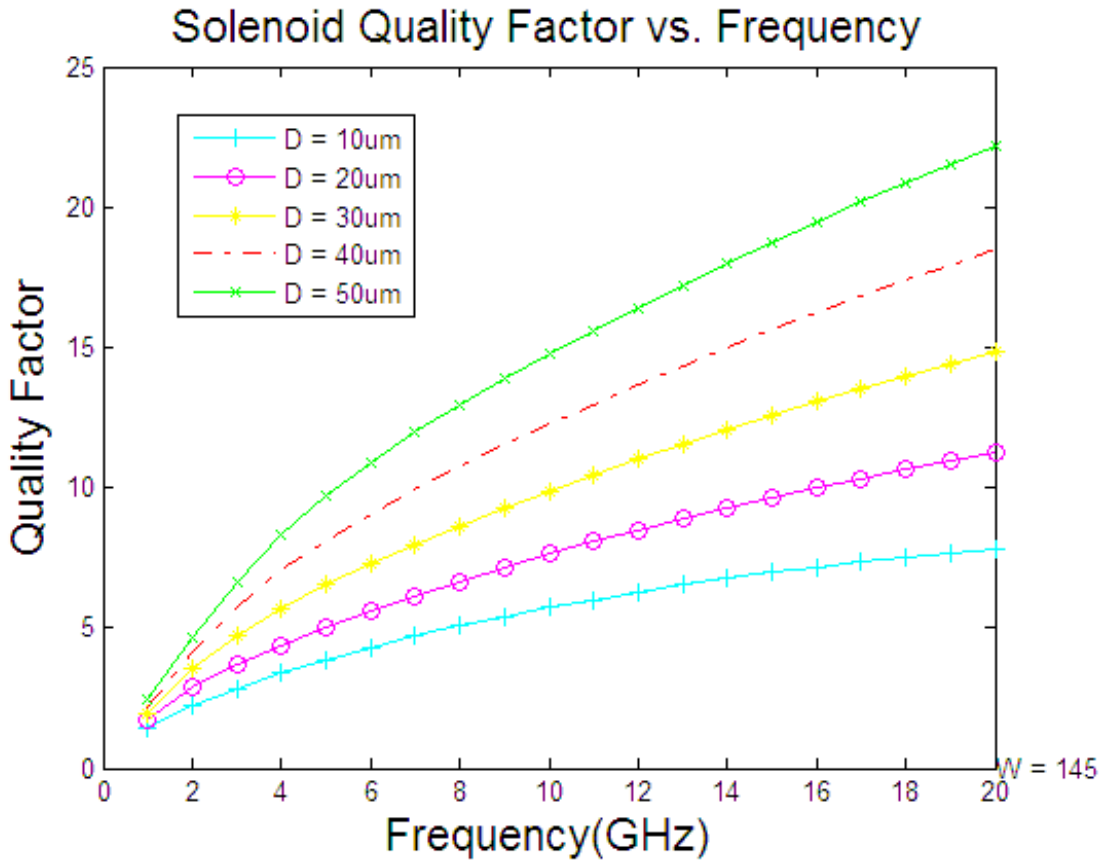

Fig. 19 Quality factor versus frequency for the first five solenoid designs of Table I.

between *Q* and frequency and turn-to-turn spacing. The *Q* value is strongly dependent on spacing, and increases even more rapidly with increasing frequency. This can be explained by examining the terms in (52) and (53). An increase in frequency has the effect of increasing *Q*, but also of reducing the *SRF* which reduces *Q*. Also, *C* will reduce *Q* by reducing the *SRF*. These competing factors result in the curves of Fig. 19. Finally, the reduction in quality factor with more tightly-spaced turns is clearly related to the AC resistance of Fig. 20. AC resistance has a strong frequency dependency, even more so as the turn-to-turn spacing approaches 5 microns (D = 10μm).

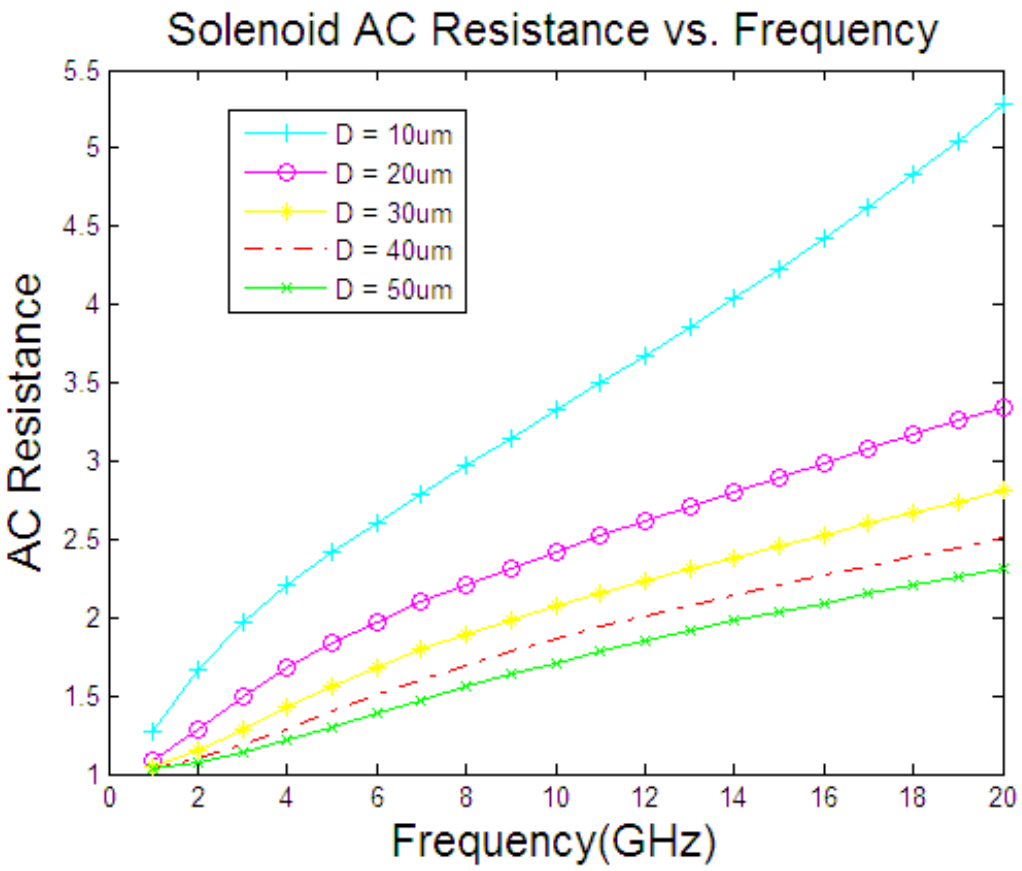

Fig. 20 AC resistance versus frequency for the first five solenoid designs of Table I.

A review of Fig. 18 reveals that by stretching the solenoid *D* value from 10μm to 20μm, the inductance actually decreases. Then, upon further increase of *D*, the inductance continues to increase. The factors causing this effect are related to the self and mutual inductance values, the capacitance, and the total width (*W*) of the turns.

The Matlab model can be readily configured to simulate inductance values for higher frequencies as well. The results presented in Fig. 18 and Fig. 19 reveal that the inductors did not reach their resonant frequency at which point the quality factor reaches zero and the solenoid reactance changes from inductive to capacitive. Therefore, simulations were performed in the range from 1 to 40 GHz to determine the resonance

frequency. The designs in Table I correspond to the largest solenoids that were experimentally fabricated and tested (see next section) and thus had the best chance of exhibiting resonance. Correlation of the resonance point, both with the model and experimental data, helps fine tune the Matlab model. A comparison of modeled and measured data is presented in a later section to complete this correlation process. The next section compares results from a full 3-D finite element electromagnetic wave solver with the Matlab model developed in this thesis. A portion of the DOE is examined here to verify the physics developed for the Matlab model.

D. CoventorWare Model

CoventorWare utilizes finite element analysis to solve the proper electromagnetic equations governing the fields through and around the solenoid turns and dielectric medium. The process of building a 3-D solenoid model involves first defining a technology materials file that describes the physical properties of the solenoid building blocks. These include the conductivity, permeability and thermal resistivity of the conductor, such as the gold turns, or the permittivity of the dielectric, such as the SU-8. From this point, a description of the layout or 2-D representation of the layers defining each processed layer of the solenoid is required. Fig. 21 illustrates the layout in L-Edit format which was later converted to gds (graphical data system) format for use directly in CoventorWare. This conversion is readily accomplished, at which point the layer names must be specified to match those in CoventorWare. The first layer (metal 1or M1) is formed by electroplating gold from a seed layer which serves as a continuity layer. The form or mold in which the gold plates, is created in a layer of SU-8 photosensitive epoxy which has a dielectric constant of 3.9. The SU-8 thickness is 5μm and the gold

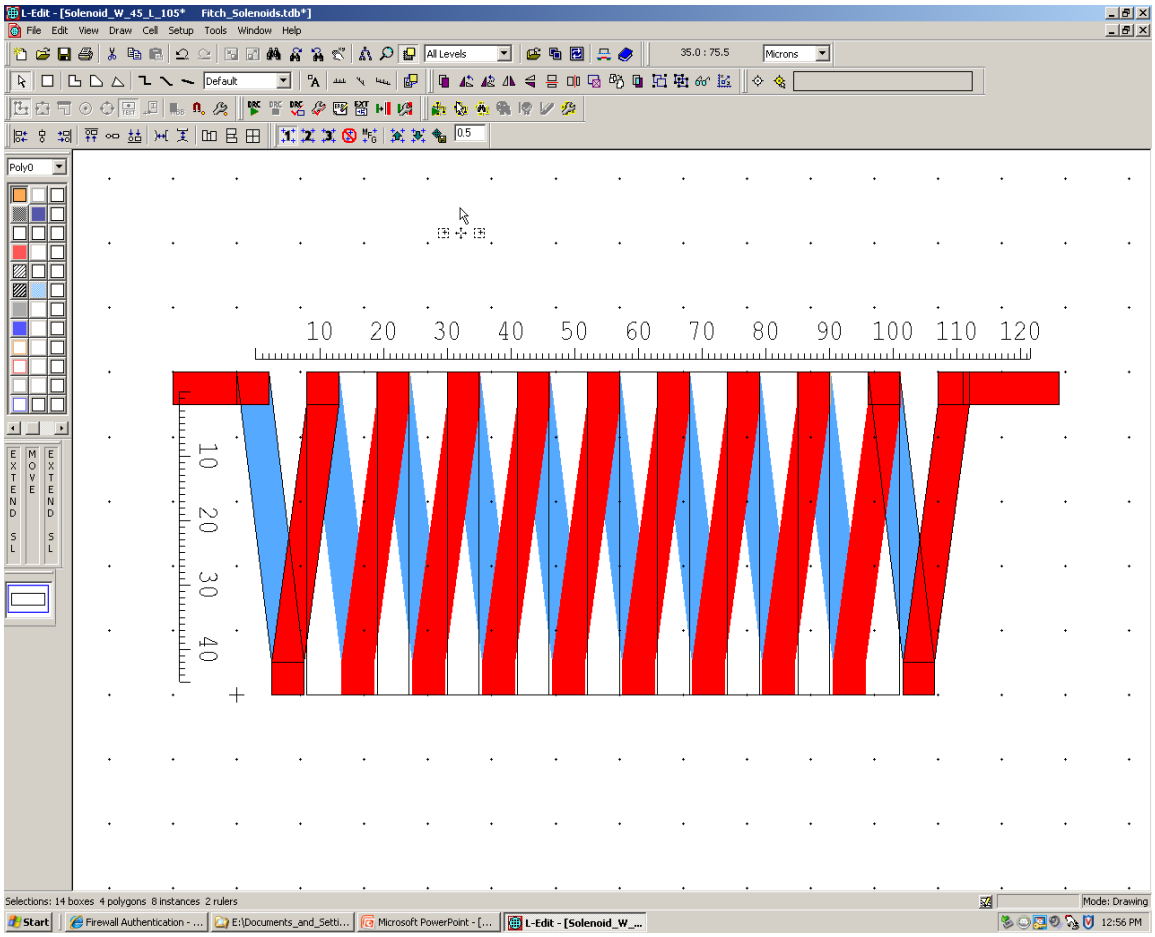

Fig. 21 2-D layout of the solenoid layers (bottom span, posts, and top spans).

plates to the top of the form leaving a planar surface. The second layer (POST) consists of the vertical columns which are also electroplated using the bottom seed layer. The final layer (metal 2 or M2) is formed after a second seed layer is deposited over the post SU-8 layer. The process description file highlights each of the fabrication steps, and is shown in Fig. 22. The layout file and process description file are used by CoventorWare to form a 3-D physical model of the solenoid which can be meshed into extruded bricks for the finite element analysis portion of the simulation. A ten-turn solenoid mesh model is shown in Fig. 23. To perform the electromagnetic simulation, the mesh model requires input and output patches or 2-D surfaces attached to a 3-D extruded brick that are each at

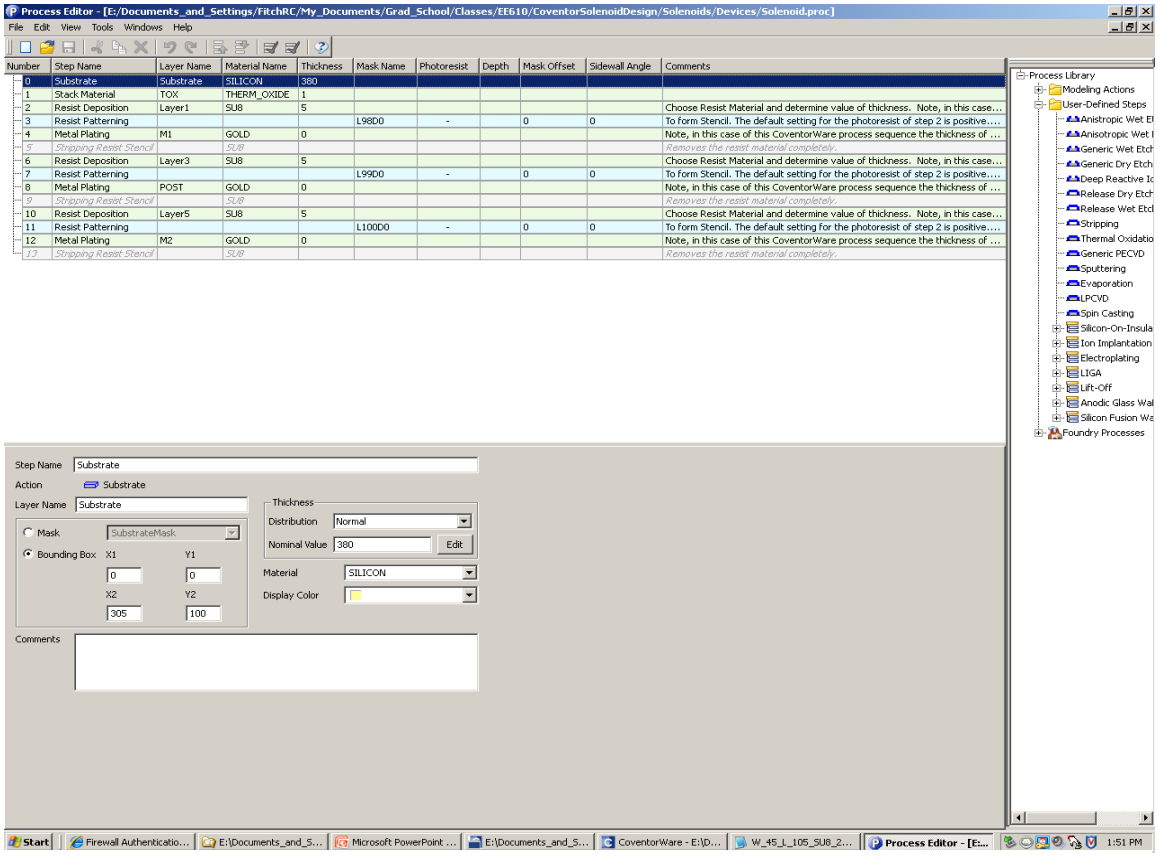

Fig. 22 CoventorWare process description file for electroplated solenoid designs.

a fixed potential. The MemHenry simulation is then run to obtain the inductance and AC resistance versus frequency. A typical simulation for a ten-turn solenoid at eight frequencies requires 10 to 45 minutes of computer time.

For the DOE designed to examine turn-to-turn spacing variations, upon completion of the process description, the .gds layout files were imported into CoventorWare and then a mesh model was made for each design. The first mesh attempted was made from extruded bricks with 1μm features as shown in Fig. 23 (note that the SU-8 layer was also meshed but was removed from the picture for clarity). This design proved to be too tight of a mesh for the simulator to converge on a solution without the computer running out of memory; therefore the extruded brick feature size

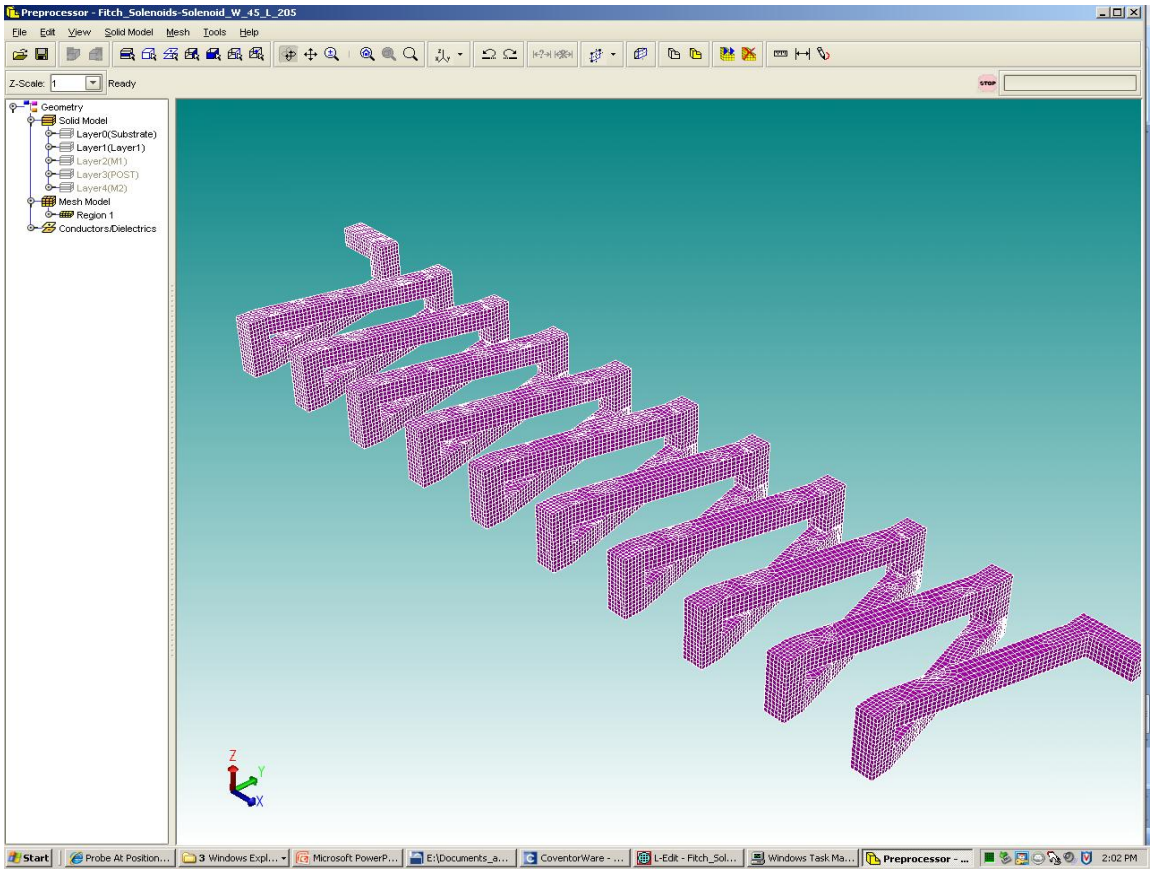

Fig. 23 Extruded brick mesh model for the solenoid designs.

was increased to 5μm. The resulting simulations converged in approximately 20 minutes each. The "MemHenry" analysis tool was used for the simulations since it provided the inductance and AC resistance values for the solenoids. This tool takes into account the skin effect which causes an increase in resistance as frequency increases due to current confinement to the outer edges of the conductor. This effect also causes a decrease in the self-inductance of the wire. The tool also will generate a 3-dimensional representation of the current density through the structure. Since the material description file includes the critical parameters for the gold conductor layers and the SU-8 dielectric layers, the displacement current in the SU-8 can also be visualized. The real and imaginary

components of current density in each of the three coordinate directions are illustrated as well, and this provides a nice tool in evaluating hot spots in current density.

A visualization of this 3-D current density is shown in Fig. 24. The current

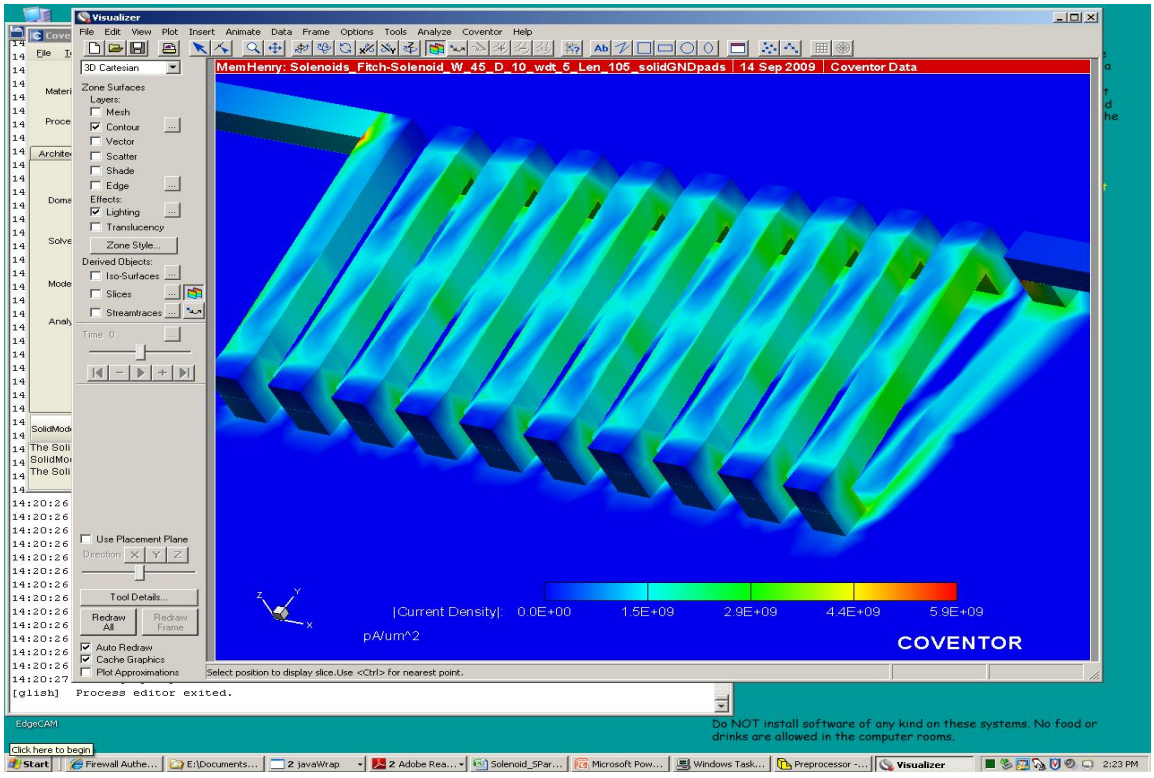

Fig. 24 Electromagnetic simulation results showing current density distribution through gold solenoid turns and displacement current in dielectric SU-8 layer surrounding the solenoid.

clearly does not flow entirely inside the conductive gold layer, but also flows as a displacement current in the SU-8 dielectric layer. In this picture the top and middle layers of SU8 have been removed leaving only the bottom layer for clarity. Current crowding is noted along the inside bends of the solenoid, and is highlighted more distinctly in Fig. 25. The software also allows one to rotate the 3-D structure into any orientation to examine the current distribution in regions of interest, such as the inside corners between posts and spans. The current distribution can also be broken into the real and imaginary portions and viewed as in Fig. 24 and Fig. 25. The frequency dependent

inductance and resistance values of design 1 are shown in Fig. 26, and clearly illustrate the decrease in inductance and increase in resistance due to the skin effect.

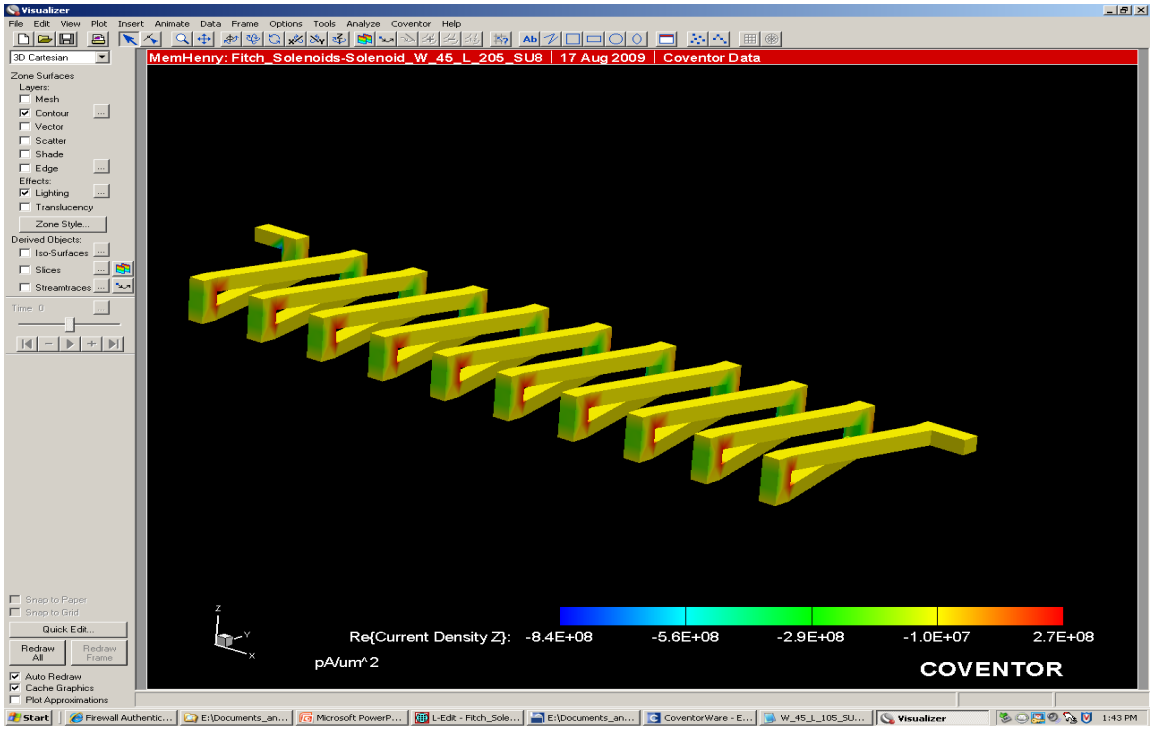

Fig. 25 Enhanced view of the current distribution in the solenoid turns.

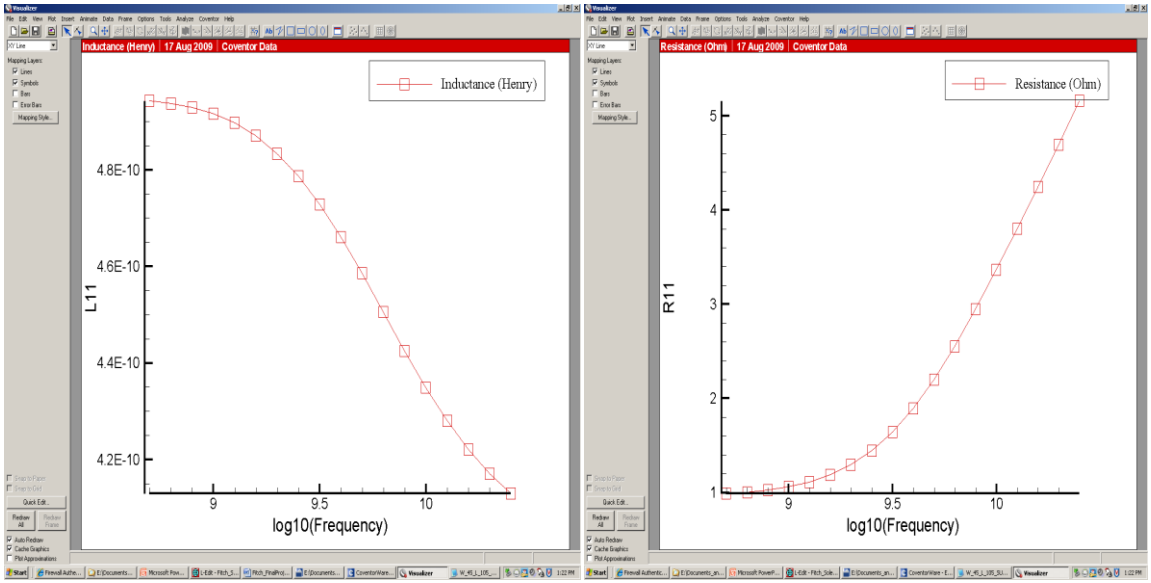

Fig. 26 Simulated inductance (Henries) and AC resistance (ohms) versus log frequency for solenoid design 1.

IV. Experimental Study

A. Introduction

This section addresses the modeling, fabrication and testing of solenoid inductors for microwave circuits composed of active and passive components embedded in an interposer layer of SU-8. To date much research has focused on on-chip spiral and solenoid inductors and subsequent substrate losses and proximity effects [**19**] [**21**] [**22**]. In this work, the model has the flexibility of removing the effect of the substrate. Also, the substrate was removed physically using deep reactive ion etching of silicon, to verify the intrinsic performance of the solenoid and clarify geometric variation effects. The conductor skin effect was also accounted for in the electromagnetic modeling of the coils.

B. Solenoid Design Matrix

In order to study the effects of geometry on inductor performance and to verify the Matlab and CoventorWare models and simulations, a design of experiments was performed to include variations in the dimensions of the solenoid shown in Fig. 11. The design matrix was laid out in .gds (graphic data system) format for subsequent import from Tanner Research's L-Edit (for .gds generation) to Coventor's CoventorWare (for finite element electromagnetic simulation). A technology file describing the process flow to account for the vertical dimensions (i.e. the gold and SU-8 layer thicknesses) was created in CoventorWare which combined the lateral and vertical device dimensions to generate a 3-D mesh of the solenoid and the SU-8 epoxy. This mesh provided a

framework for the electromagnetic finite element simulations to determine the inductance and AC resistance of the coil versus frequency, *f*. The simulations were performed for designs with no ground shield (i.e. $t_{SU8} = \infty$). Table II illustrates the design matrix which

Table II

SUMMARY OF SOLENOID DESIGNS

Design	*w(μm)*	*d(μm)*	*t(μm)*	*W(μm)*	*D(μm)*	*H(μm)*	Turns
1-5	5	5	5	45	10,20,30,40,50	10	10
6-10	5	5	5	95	10,20,30,40,50	10	10
11-15	5	5	5	145	10,20,30,40,50	10	10
The layouts of these designs are illustrated in Appendix B.							

focused on variations in turn-to-turn spacing for *w*=*d*=5μm. The variables *t* and *H* were held at 5 and 10μm, respectively, for all designs, and the number of turns was fixed at 10.

C. Solenoid Fabrication Technique

The fabrication process developed to achieve completed gold solenoids shown in Fig. 27 and Fig. 28 is described in the following section (Appendix C gives a cross-sectional and top-down illustration of the entire process flow). The silicon substrates utilized were 380μm thick with 1μm of thermal oxide on both sides. The thermal oxide acted as an etch-stop layer for the DRIE of the backside pockets of removed silicon that were formed after the front-side solenoids were fully fabricated. The seed layer (Ti/Au 200Å/1000Å) for the bottom turns of the solenoid was deposited using a Denton Discovery 18 DC Magnetron plasma system. The SU-8 2005 photosensitive epoxy resist was dispensed onto the wafer and after a 10 second ramp to 3000rpm was held at that

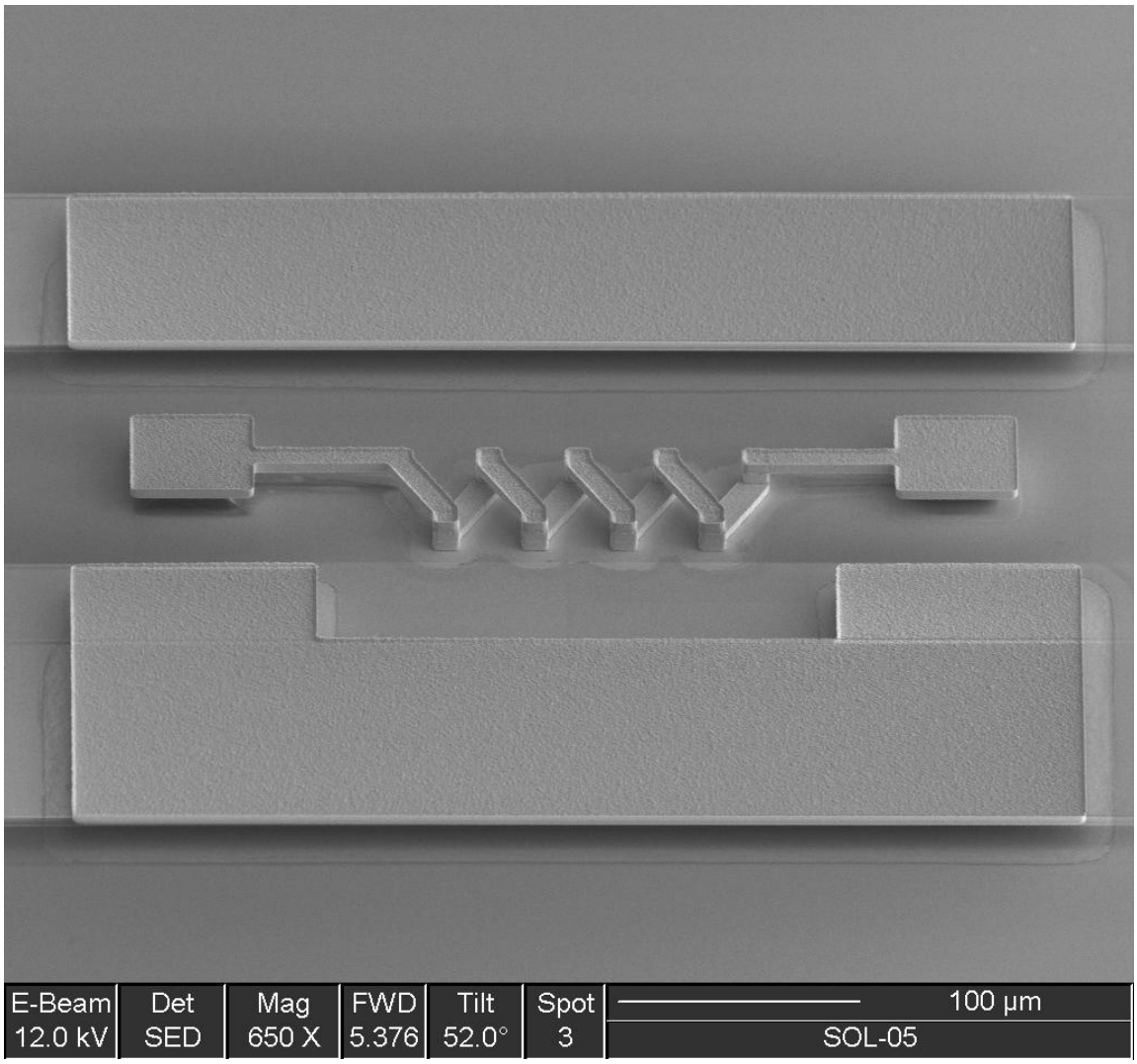

Fig. 27 Scanning electron microscope photo showing a completed solenoid structure and ground-signal-ground test pads (SU-8 removed for clarity).

rpm for 30 seconds. This provided a 5.2µm thick layer of SU-8. The pre-exposure bakes were sequential at 65°C and 110°C for 3 minutes each. This ramp in temperature was one factor in assuring proper adhesion of the SU-8 to the SiO_2. A Karl Suss MA6 Backside Aligner was used to expose the SU-8 at 7mW/cm^2 with 365nm ultraviolet radiation for 10 seconds to create an acid that initiated the epoxy cross-linking during the post-exposure bakes which were identical to the pre-exposure bakes. SU-8 developer was used to spin/puddle develop the negative resist for one minute and quenched with an

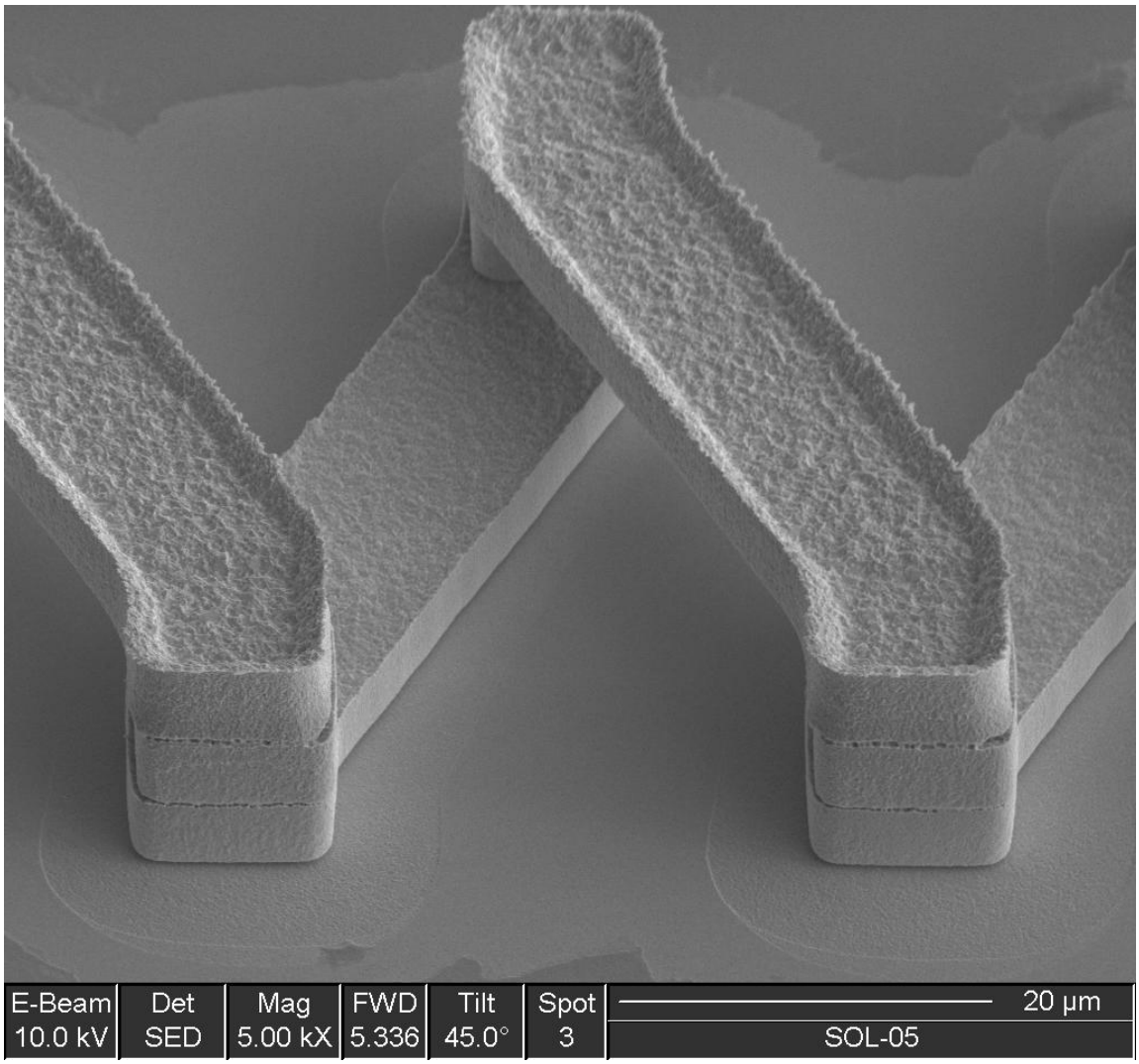

Fig. 28 Scanning electron microscope photo showing a higher magnification image of the solenoid turns.

isopropyl alcohol rinse. Slight fissures occurred at sharp edges in the pattern, but were removed after sequential post-develop bakes of 110°C and 200°C for three minutes each. This resist form was subsequently electroplated with gold in a Technic Inc. 25E plating bath using a 40% duty cycle and 2mA/cm^2 current density. The vertical posts of the solenoids were similarly electroplated using a second layer of SU-8, also 5µm thick, while using the same initial seed layer for continuity. The top metal traces and probe pads required a second seed layer of Ti/Au (200Å/1000Å) deposited on top of the post

SU-8 layer. The top metal mask was similarly formed and filled with 5μm thick electroplated gold.

Removal of both seed layers was required to produce testable devices, therefore two approaches were used. To remove the top seed, the top SU-8 layer was etched in a barrel asher oxygen plasma at 170W, 750sccm and 3Torr for one hour. The exposed top seed layer was removed in two steps: 45 seconds in KI solution Au etch followed by 20 seconds in buffered oxide etch, BOE:DI (1:10) to remove the Ti. The silicon beneath the solenoids was removed to facilitate removal of the bottom seed layer. The backside of the wafer was patterned with the pocket mask using 25μm thick SU-8 (identical bakes as SU-8 2005, but exposure time of 20 seconds). The silicon was removed in a Plasma-Therm Versaline Deep Reactive Ion Etcher using a Bosch passivate and etch process to form an open pocket beneath each structure. The silicon etch rate was 6μm per minute, and the etching stopped selectively to the front-side SiO_2 layer. The SiO_2 layer was removed in a Plasma-Therm 790 Reactive Ion Etcher (RIE) in a 30 minute etch. The resulting pocket exposed the front-side's bottom seed layer through the back-side of the wafer, and this seed layer was subsequently removed using BOE:DI (1:10) for 20 seconds to etch the Ti and KI for 45 seconds to remove the Au. The devices and open pads were testable at this point. See Appendix C for a photo of the open suspended solenoids.

D. Solenoid Design Characterization

The electromagnetic simulation of the design matrix was carried-out using CoventorWare and the MemHenry analyzer which provided the inductance values as well as the AC resistance versus frequency. Fig. 29 illustrates the inductance versus

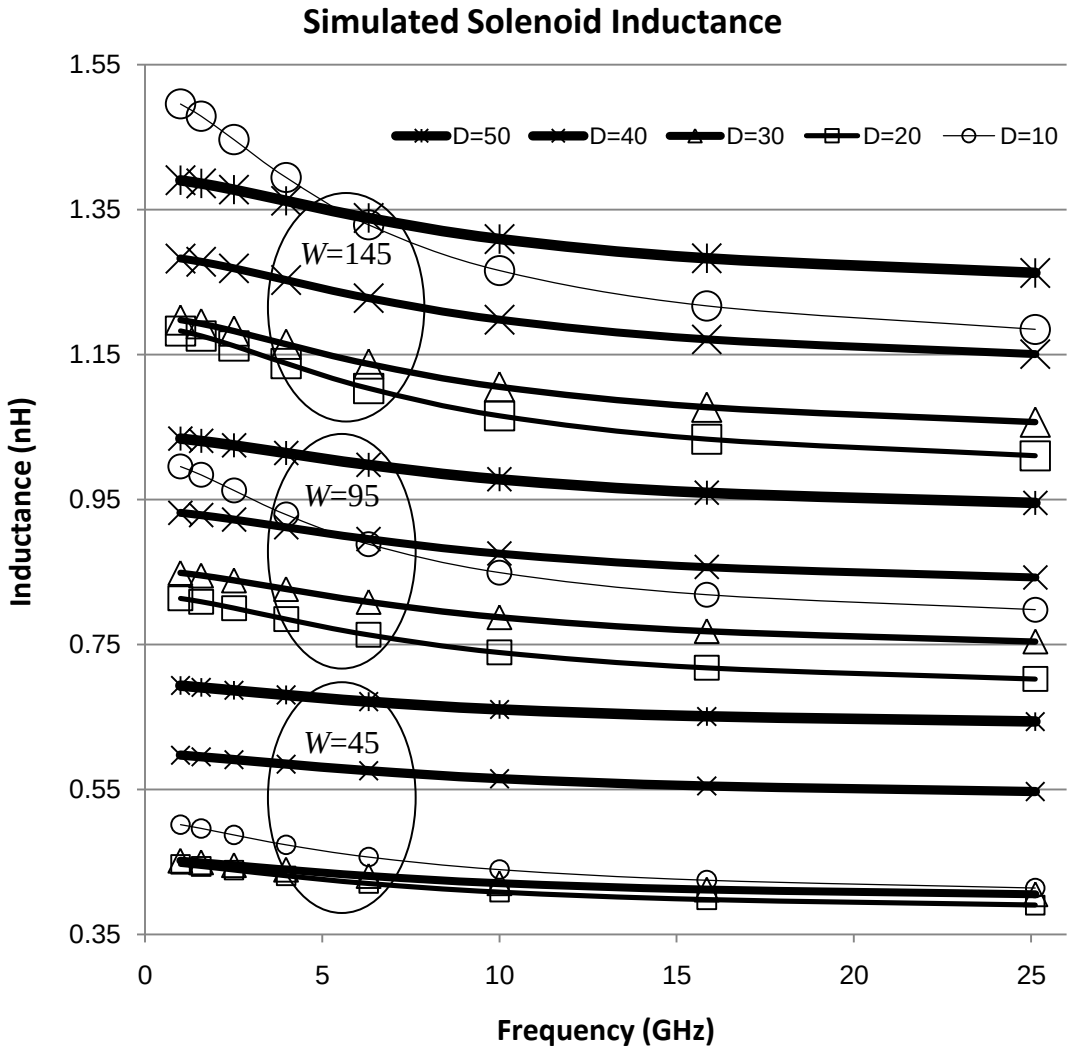

Fig. 29 Simulated inductance values versus frequency for the 15 designs of Table I.

frequency results for the 15 designs of Table II. Note that within each group of constant solenoid widths, *W*, as the turn-to-turn spacing, *D*, increases from 10µm to 20µm the inductance decreases abruptly, but then for *D* of 30µm and above, the inductance increases. The overall spread in inductance for each group is approximately the same, however, for the most tightly spaced solenoids, *D* of 10µm, the overall change in inductance versus frequency is the greatest and becomes even more pronounced as the solenoid width increases. Another observation is the consistent decrease in inductance with increasing frequency.

The matrix of solenoids was tested using an HP 8510 network analyzer to obtain the small-signal S-parameters from 1-26 GHz. The ground-signal-ground pad structure for each solenoid design was also tested to account for the pad parasitic's which were subtracted from the intrinsic solenoid data. The inductance, AC resistance and quality factor were calculated from the S-parameters, and Fig. 30 illustrates the inductance

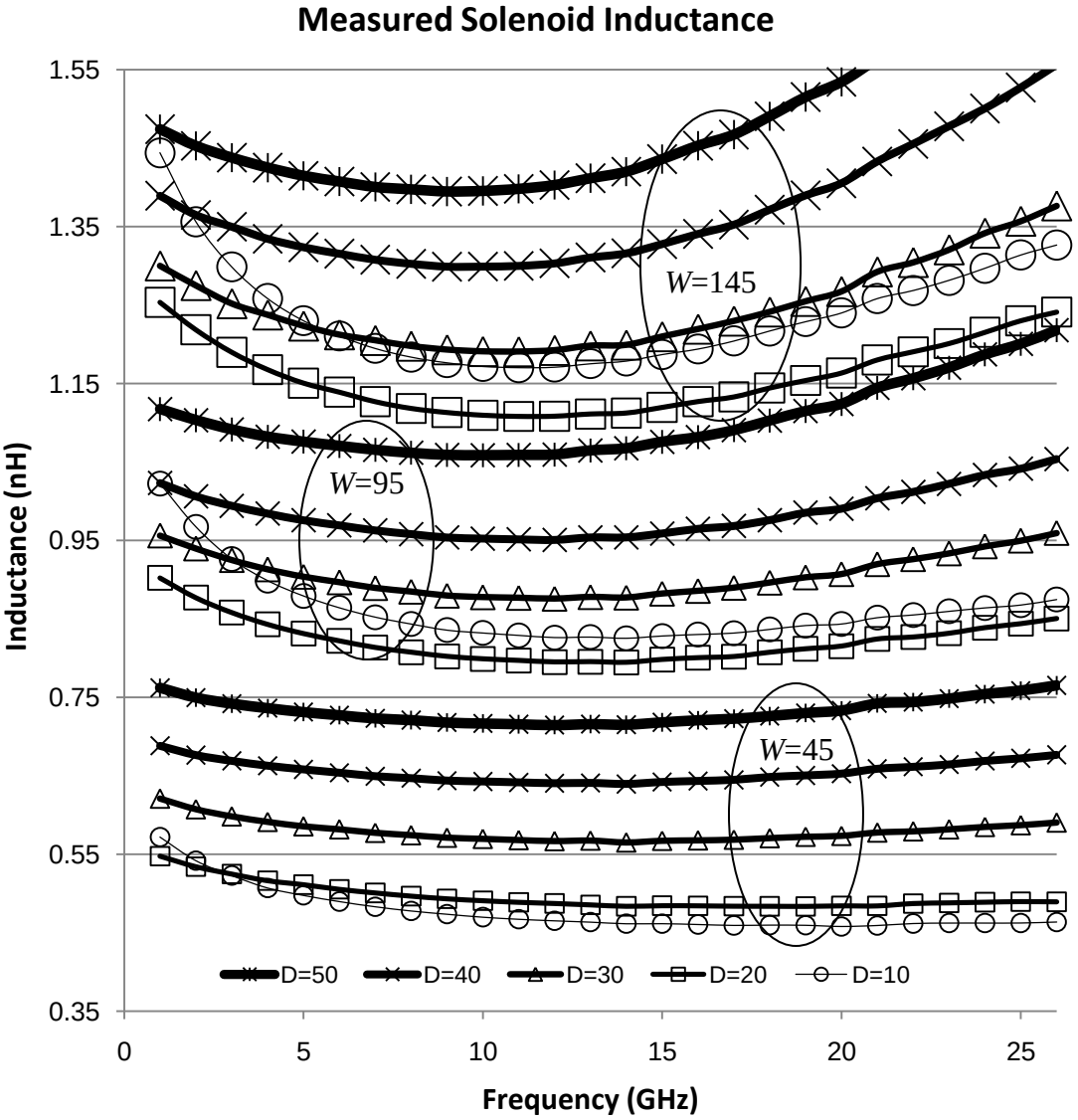

Fig. 30 Extracted inductance values versus frequency from measured S-parameter data for the 15 designs of Table I.

values versus frequency for the 15 designs of Table I. The primary difference between

the simulated and measured data is the increase in inductance with increasing frequency for the measured data, most significant for the wider solenoids. Also, the overall spread in inductance becomes more pronounced as the width increases. Finally, the 45µm wide group simply shows an increase in inductance with increasing turn-to-turn spacing except at the very lowest frequencies.

The simulated quality factor versus the measured value for the 145µm-wide group of solenoids is shown in Fig. 31. Only this group is illustrated since the same trends were

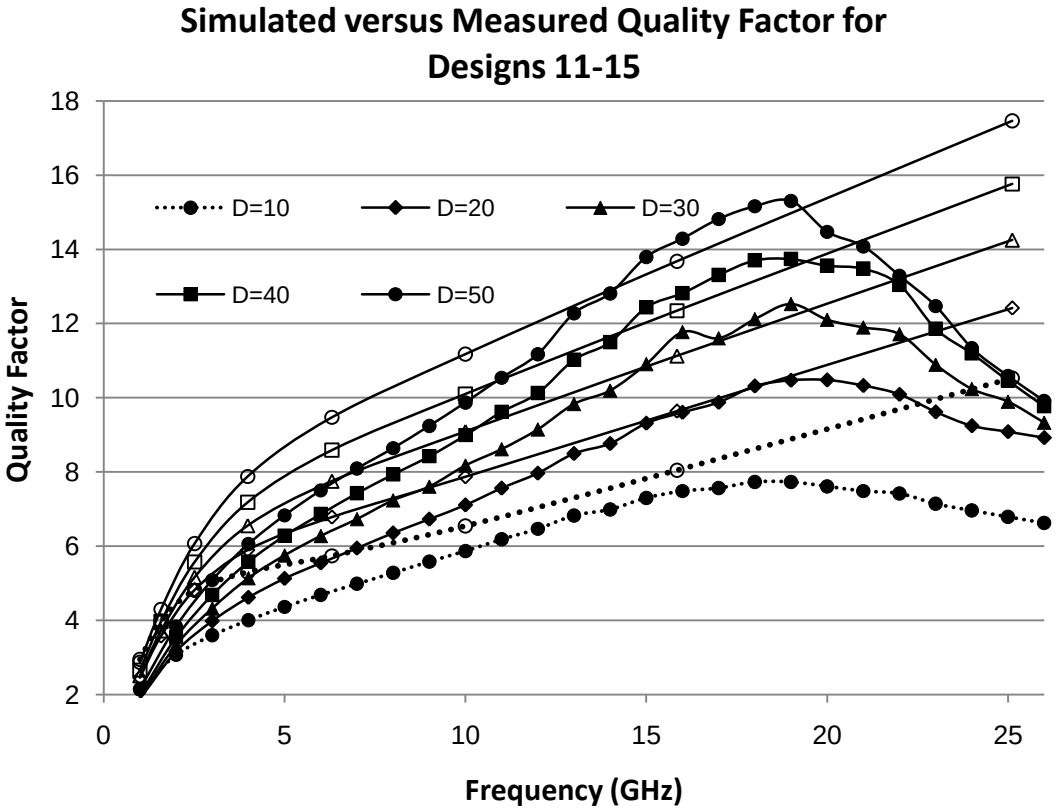

Fig. 31 Simulated quality factor (open markers) versus measured value for 145µm-wide solenoid designs 11-15.

noted for the 45µm and 95µm width groups. Most notable is the peak in quality factor for the measured data whereas the simulated values do not peak. Fig. 32 shows the simulated versus measured AC resistance where a marked increase in AC resistance at

frequencies above the peak Q is noted for the measured data. The simulated data shows only a slight increase in AC resistance versus frequency.

A summary of f, L and R_{AC} at peak and minimum Q is shown in Table III.

Table III

SUMMARY OF MEASURED SOLENOID PARAMETERS

Design	D (μm)	W (μm)	f (GHz)	L (nH)	R_{AC} (ohms)	Q
1	10	45	22	0.46	4.0	11
5	50	45	22	0.66	4.2	24
6	10	95	22	0.85	12.7	9
10	50	95	19	1.1	7.2	19
11	10	145	18	1.2	17.8	8
15	50	145	19	1.5	11.8	15

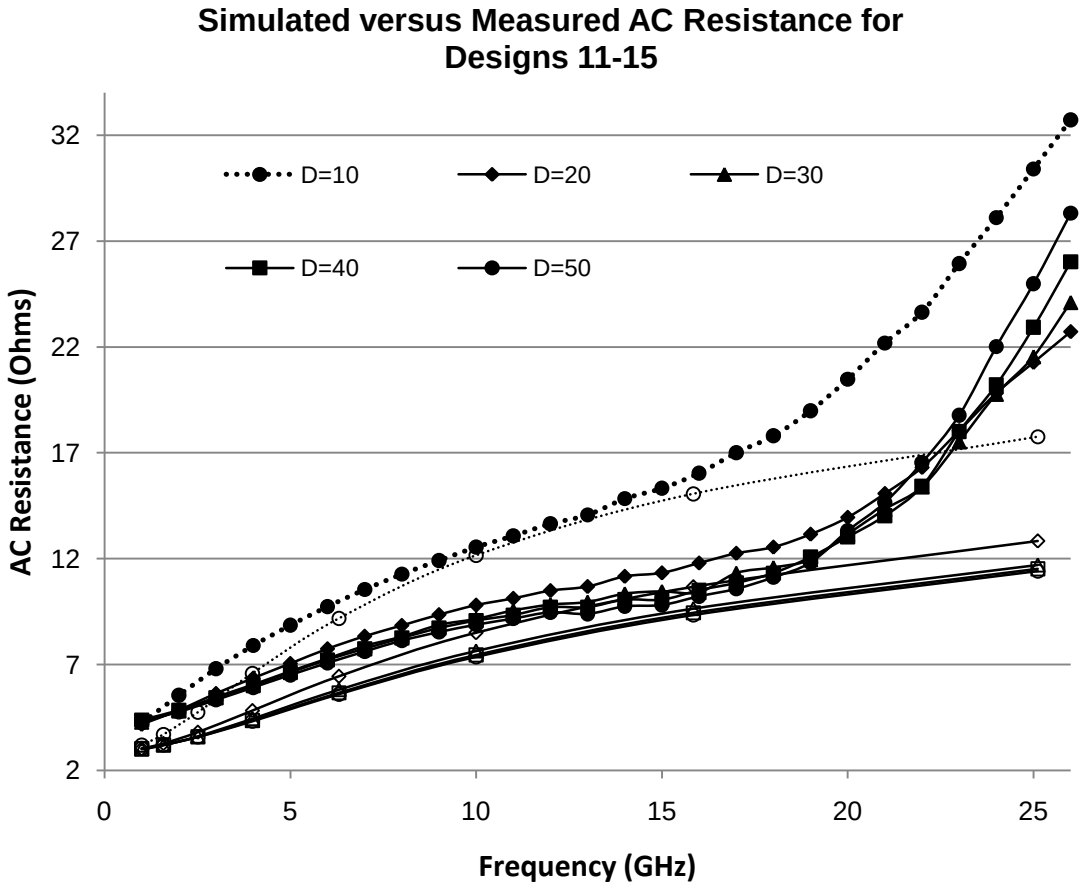

Fig. 32 Simulated (open markers) versus measured ac resistance for 145 μm-wide solenoids designs 11-15.

E. Discussion

The simulated inductance values for all three design groups demonstrate the same trend of an initial decrease as turn-to-turn spacing is increased, and then an increase when the spacing exceeds 20μm's. The advantage of increasing the turn-to-turn spacing is illustrated by the marked increase in quality factor. All designs demonstrated the lowest quality factor for the 10μm-spacing solenoids. The quality factor peaked and then decreased above the 18-20GHz range. This decrease is due to the self-resonance factor

[**21**] given as the following bracketed term in (54) which significantly reduces Q above the resonant frequency:

$$Q = \frac{\omega L_s}{R_s}\left[1 - \frac{R_s^2 C_s}{L_s} - \omega^2 L_s C_s\right] \tag{54}$$

where C_s is the turn-to-turn capacitance, R_s is the series resistance, and L_s is the series inductance of the coil. An increase in L_s, C_s or R_s affect the peak value of Q and the rate at which Q drops at points above the resonant frequency. L_s and C_s have a stronger affect on this drop in Q than R_s. The simulations were performed using a relative dielectric constant of 3.9 (at 10MHz per the data sheet) for the SU-8, however this value may be strongly frequency dependent and could account for the drop in Q. A decrease in L_s will increase this rate, but neither the simulations or measured data indicated a sufficient enough decrease in inductance with frequency to bring about this drop, therefore the most probable cause is higher than expected turn-to-turn capacitance at the higher frequencies. The simulated data accounts for an increase in AC resistance due to the skin effect, however it does not account for the higher rate of AC resistance increase above the resonant frequency seen in the measured data. This may be due to a frequency dependent change in the metal resistivity at higher frequencies. The added resistance and increased turn-to-turn capacitance account for the rapid drop in Q at these frequencies.

F. Additional Fabrication, High Frequency Testing and Model Comparison

The solenoids were initially tested from 1 to 26GHz using a vector network analyzer, however according to simulations and this testing, none of the solenoid designs

reached their resonance value where the quality factor becomes zero and the reactive part of the impedance changes from inductive to capacitive. The effect of a substrate under the solenoid also lowers the resonant frequency, therefore additional solenoids were fabricated on insulating borosilicate glass (BSG) substrates. The fabrication process was varied to accommodate the BSG substrate, and the resulting solenoid structure is shown in Fig. 33 and Fig. 34. The physical dimensions of each solenoid design remained the

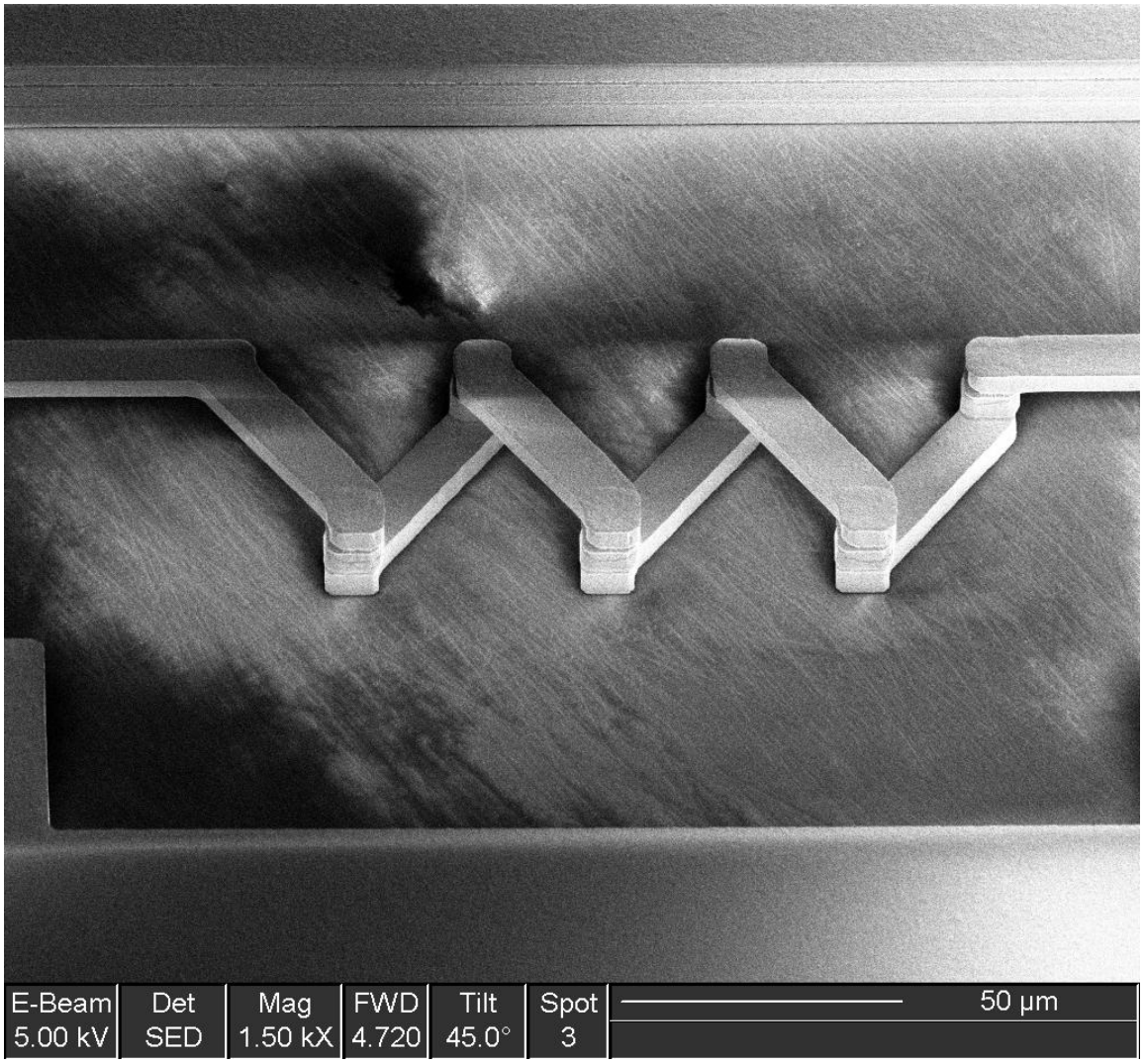

Fig. 33 Scanning electron microscope image of solenoid on a BSG substrate

same, the only difference was the presence of a substrate beneath the solenoid. To verify this point, the solenoids were tested out to 40GHz. The simulated inductance for the

largest solenoid set in the DOE, with parameters *W* of 145μm, *D* of 10, 20, 30, 40 and

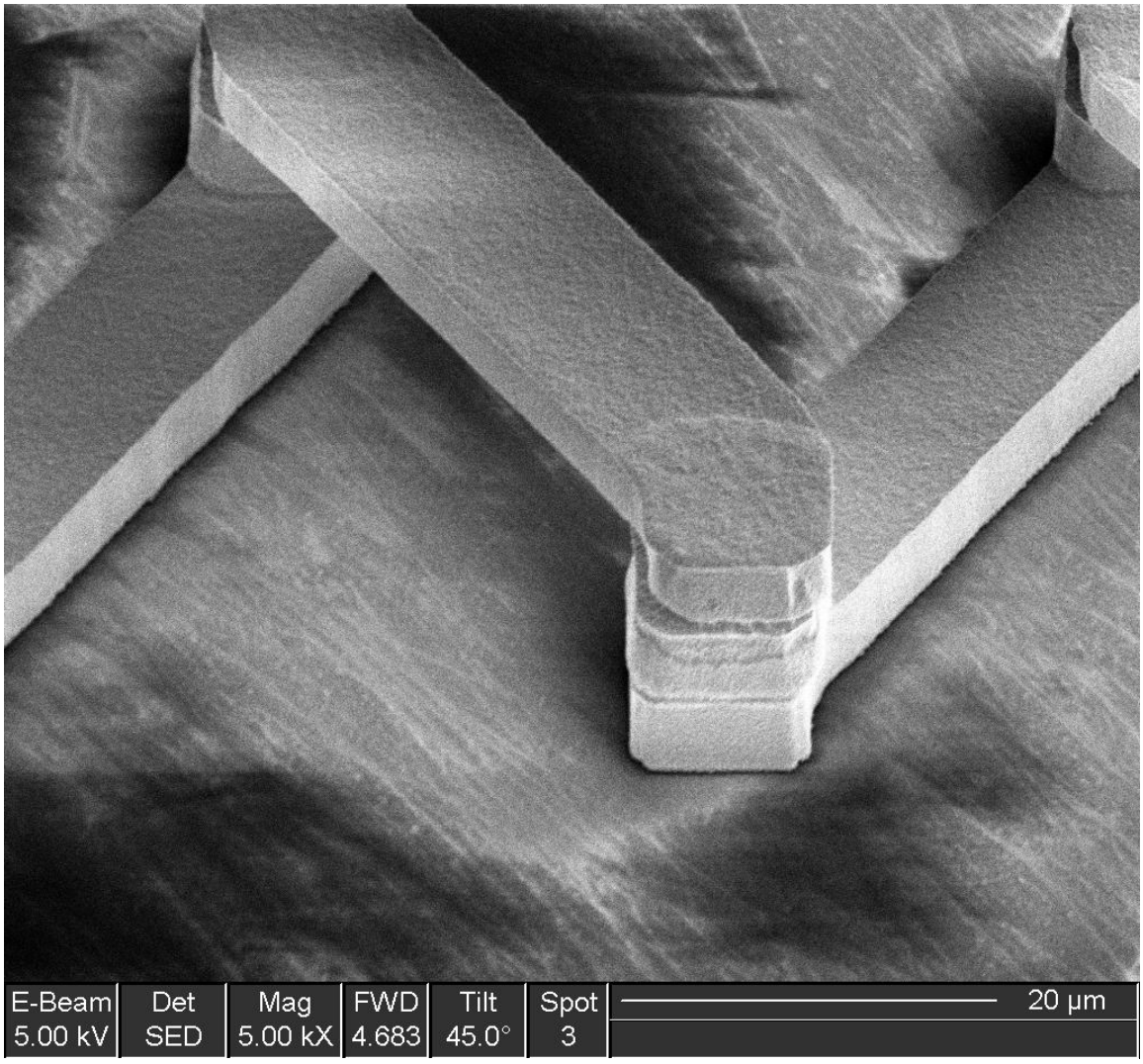

Fig. 34 Higher magnification SEM image of a solenoid on BSG substrate.

50μm and 10 turns, is shown in Fig. 35. Note the resonant peaks for designs *D* of 10 and 50μm's occur below 40GHz. The inductance for the 10μm turn-spacing inductor reaches a lower resonant peak than the 50μm turn-spacing inductor due to the higher capacitance for the former. The inductance over almost the entire frequency range from 1 to 40GHz is also lower for the first design. Fig. 36 shows the extracted inductance of these designs, which compares closely to the simulated data. The most tightly-spaced design did not yield during the solenoid fabrication; therefore empirical data was not available. Also,

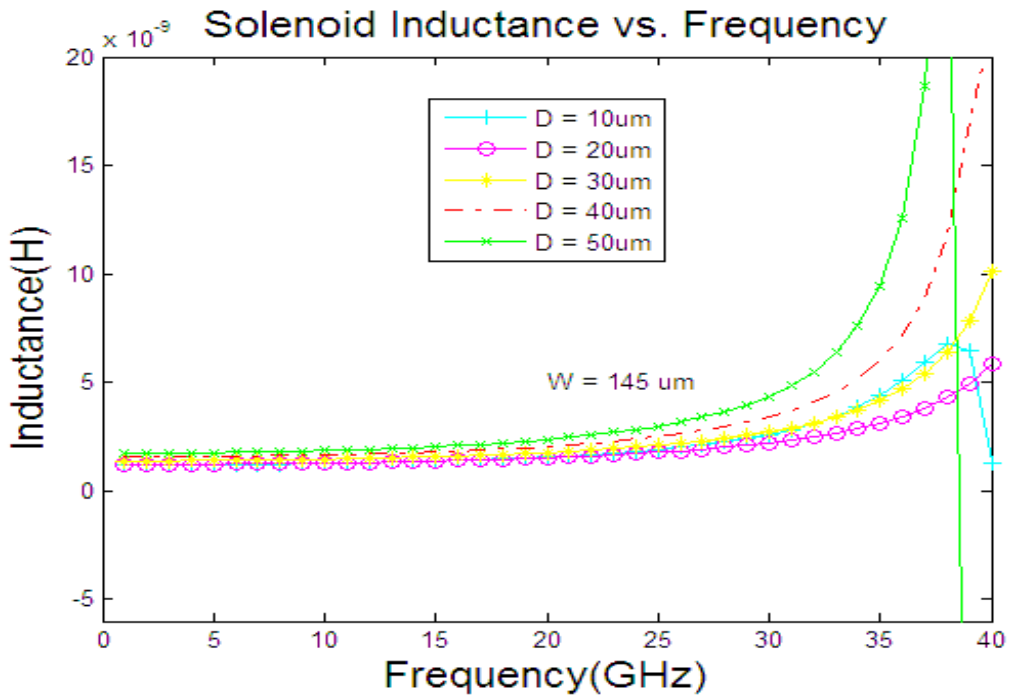

Fig. 35 Matlab simulation of inductance for largest series of solenoids in DOE.

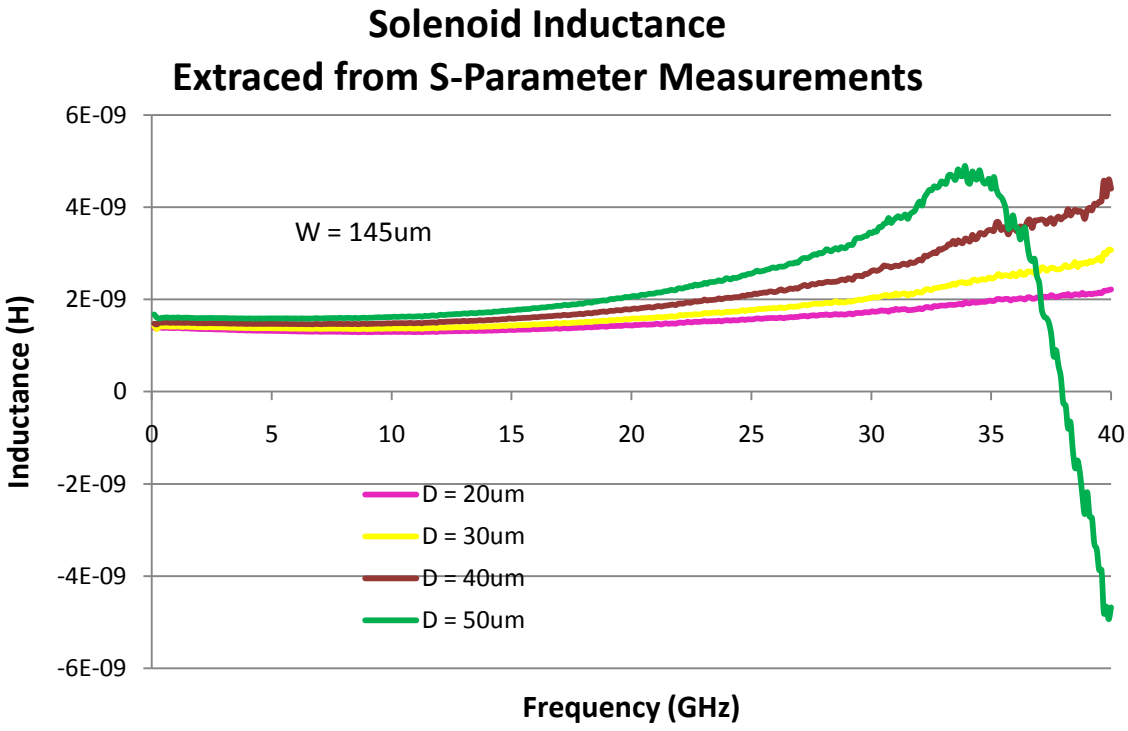

Fig. 36 Extracted inductance from s-parameter measurements of largest solenoid designs.

Fig. 37 through Fig. 40 show the quality factor and AC resistance for the simulated and

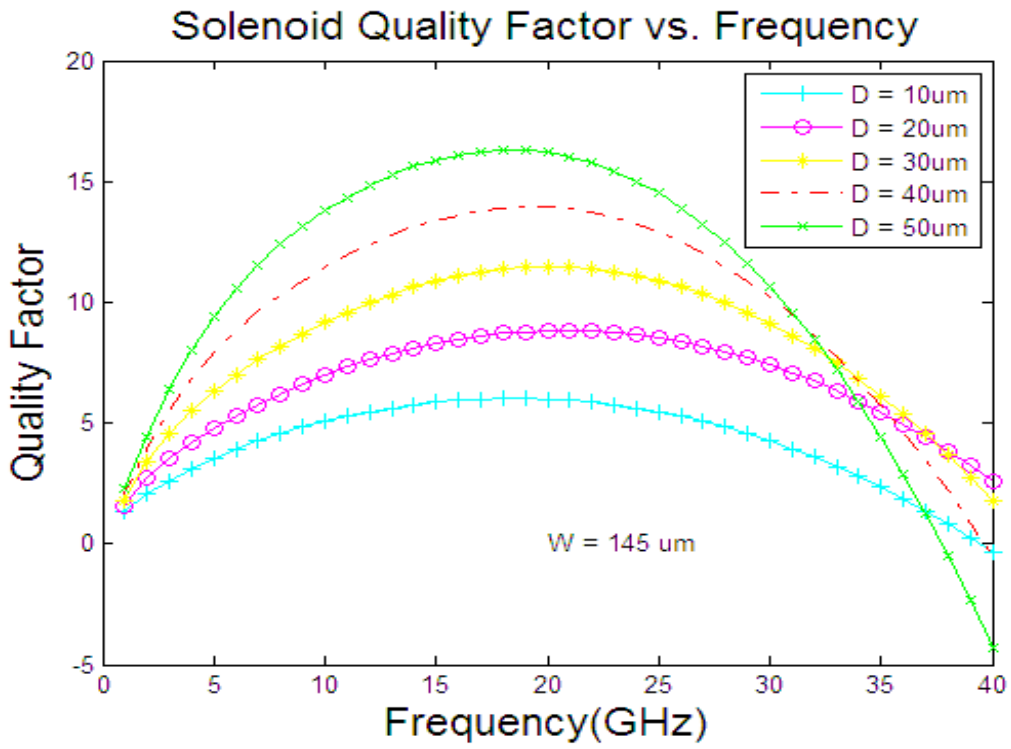

Fig. 37 Matlab simulation of quality factor for largest series of solenoids in DOE.

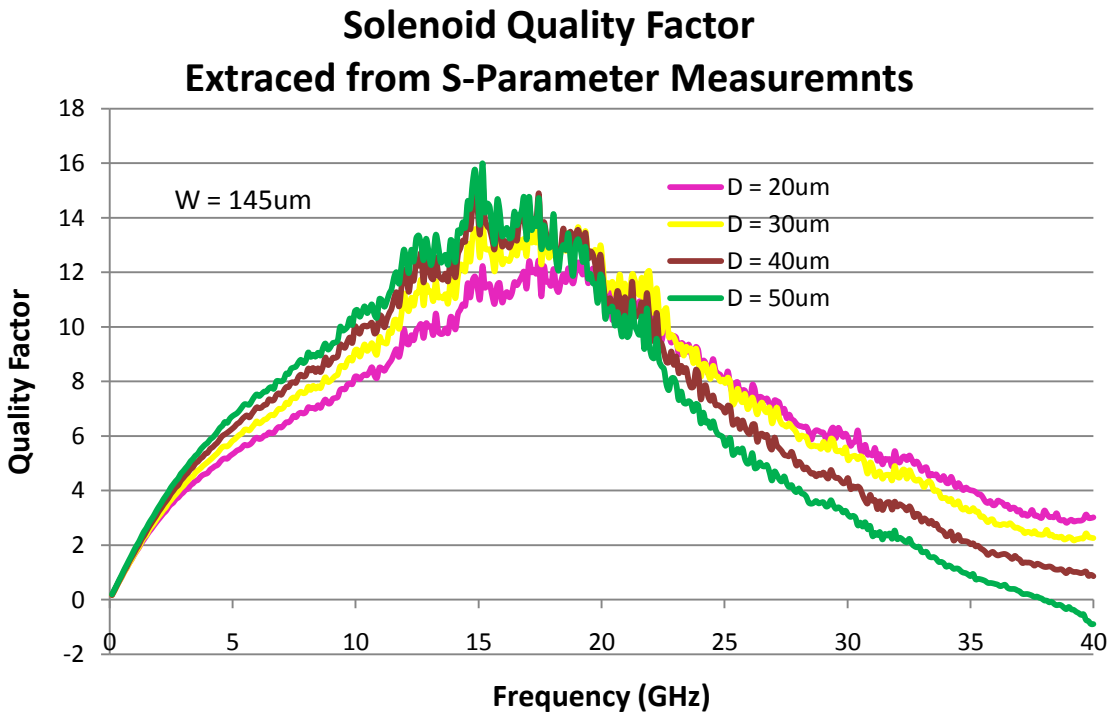

Fig. 38 Extracted quality factor from s-parameter measurements of largest solenoid designs.

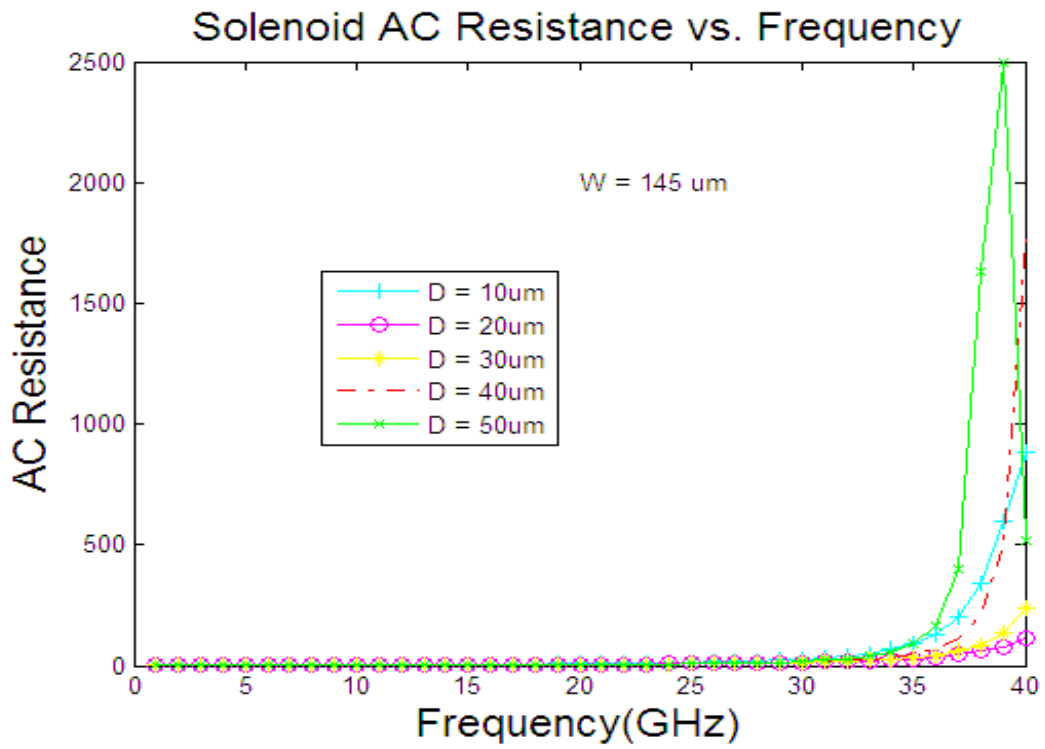

Fig. 39 Matlab simulation of ac resistance for largest series of solenoids in DOE.

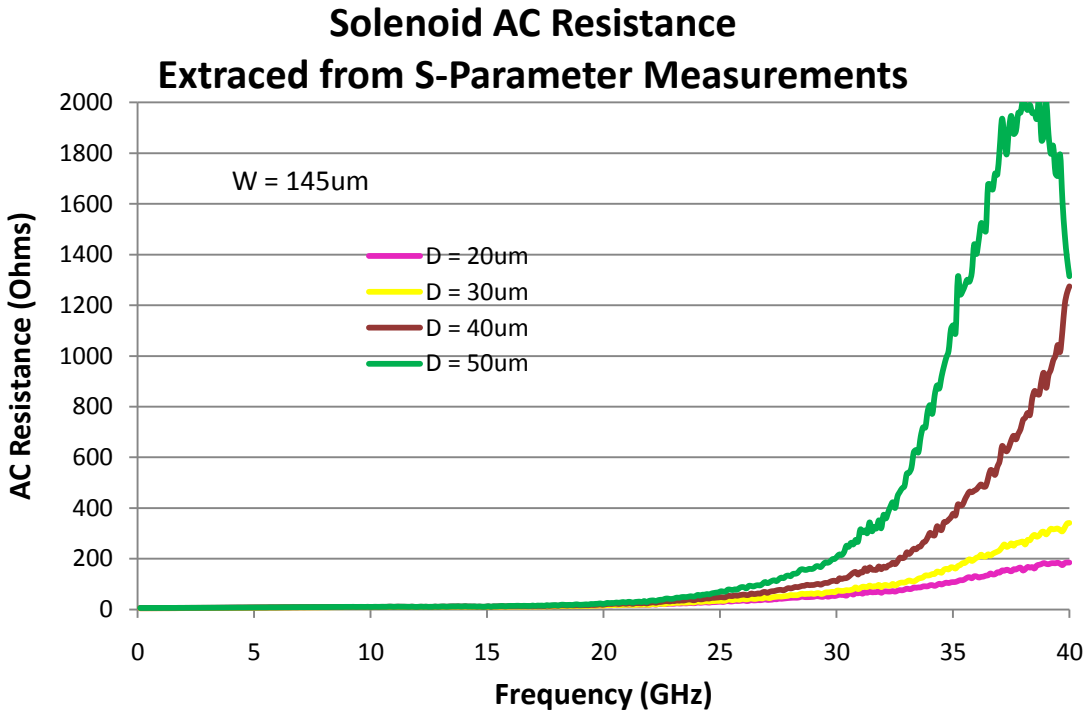

Fig. 40 Extracted ac resistance from s-parameter measurements of largest solenoid designs.

extracted designs. It is clear the highest quality factor is attained with the largest turn-to-turn spacing, yet the resonant frequency is the lowest. The AC resistance peaks first for this design as well.

An optimum inductance and quality factor for a given frequency range can be readily designed through the use of the Matlab simulation code. The model predicts a slower rate of increase in AC resistance than the measured data, and as a result the higher frequency roll-off of the quality factor does not match the measured value. The trend in decreasing quality factor with decreased turn spacing does accurately match the measured values, which was a key question regarding the geometric design of the solenoid.

1. Comparison of Inductance Values with and without a Substrate

As a final comparison of the model to measured data, two solenoid samples were fabricated with the same dimensions, however one had the silicon substrate beneath removed (SOL08) and the other was fabricated on a BSG substrate (HID29). The solenoid was the largest (W of 145μm and D of 50μm) in the DOE. Fig. 41 illustrates the measured inductance values versus frequency for the two samples. Clearly, the inductance values for the solenoid with the substrate removed are nearly constant over the entire frequency sweep. The model predicts this solenoid will reach LC resonance at a frequency of 65GHz. The solenoid on the BSG substrate resonated at 34GHz, close to the predicted value of 36GHz from Fig. 35. The peak quality factor for sample SOL08 was 27 at 19GHz with an inductance of 1.6nH, whereas for sample HID29 it only reached 16 at 15GHz with an inductance of 1.7nH.

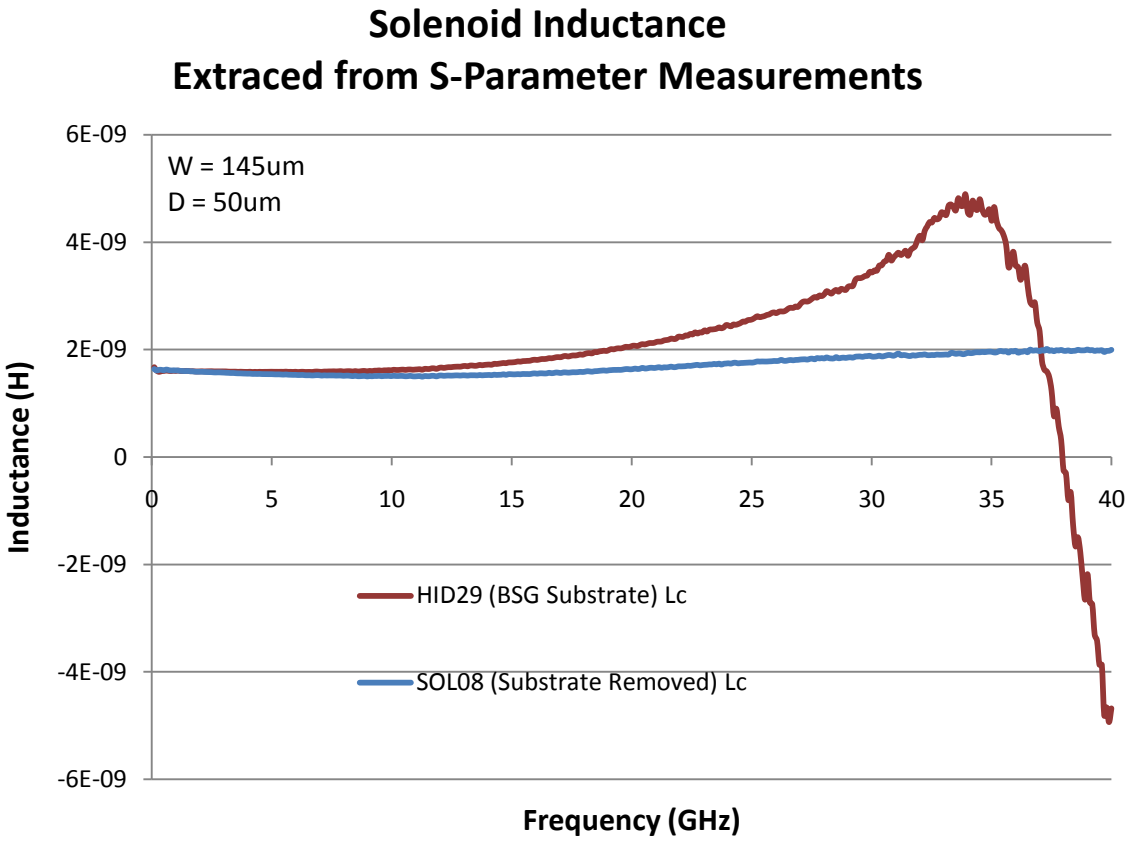

Fig. 41 Solenoid inductance for two samples with (HID29) and without (SOL08) a subtrate.

G. Addition of an FeCoAl Magnetic Core to the Solenoid

1. Characterization of FeCoAl Core Material

The addition of a magnetic core material to the center of the solenoid significantly complicates its electromagnetic characteristics, yet the inductance per unit area can be increased significantly [**23**]. If the core material, such as air or SU-8, were simply replaced by a high permeability, low permittivity, low electrical conductivity one, then the Matlab model developed here could be readily used to predict the inductance value and quality factor. However, this material presently does not exist since most ferromagnetic (FM) materials are highly conductive, such as NiFe. As a result, eddy

current losses due to image currents in the core significantly reduce the overall inductance and quality factor. Also, a demagnetization field forms inside the core; this field reduces the overall relative permeability of the core. As a result, the development of a Matlab model to include a core is left for future work. However, empirical data was obtained from solenoids fabricated with FeCoAl cores as described in the next section. Prior to fabrication of the FeCoAl-core solenoids, the FeCoAl material permeability, coercivity, magnetic moment, and high frequency response were characterized. This was accomplished via B-H loop measurements and the fabrication of transmission line test structures.

To facilitate the addition of a FM core, experiments were performed to deposit FeCoAl and NiFe using a Denton RF Plasma Sputtering System. The solid targets, obtained from Kurt J. Lesker, had composition's of $Ni_{80}Fe_{20}$ and $Fe_{36}Co_{36}Al_{28}$. The deposition of NiFe required an RF power of 250W, an argon flow of 4 standard cubic centimeters per minute (sccm) at a pressure of 4mTorr, to obtain a deposition rate of 4.4Å/sec. The same conditions resulted in a rate of 5.9Å/sec for FeCoAl.

The magnetic characteristic of the NiFe and FeCoAl thin films were characterized using a Quantum Design SQUID (Superconducting Quantum Interference Device) MPMS-XL Magnetometer. From the resulting B-H loops of the NiFe and FeCoAl films, the DC permeabilities were 108 and 97, the coercivities were 57.5 and 22.6Oe, and the saturation magnetizations were 748 and 294emu/cc, respectively. The values for the FeCoAl film were lower than expected, but future enhancements of the core may be attained through annealing in a magnetic field or applying a magnetic field during the deposition process.

Two BSG characterization wafers, labeled HID30 and HID31, were fabricated without and with an FeCoAl thin film sandwiched between a bottom ground plane and top-side transmission line test structures [**24**]. Additional wafers processed with NiFe as the core material were intended to serve as a standard comparison with previously published work. However, these wafers did not yield testable devices, therefore only FeCoAl transmission line test structures and FeCoAl-core solenoids are discussed.

These transmission line test structures (shown in Fig. 42) were

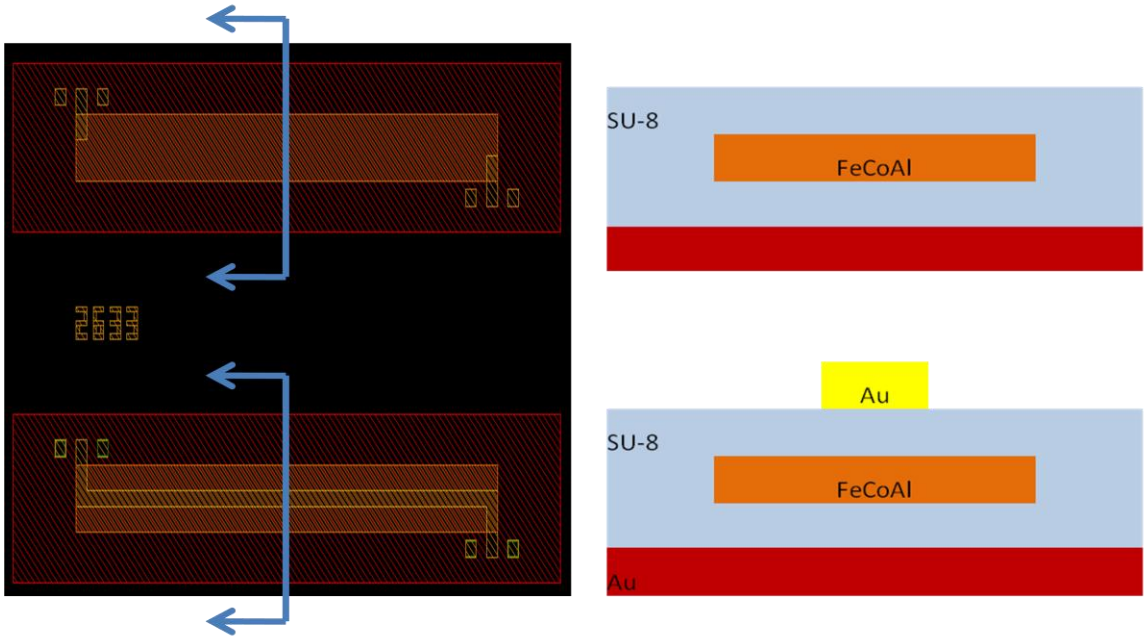

Fig. 42 Transmission line test structures (top are de-embedding structures, bottom are 10μm-wide Au transmission lines) with magnetic thin film (orange) sandwiched between the top (yellow) and bottom metal (red) layers (top-down views on left and cross-sections on right).

used to obtain the attenuation constant and propagation wavelength for the FM film according to [**25**] [**17**]. The top metal traces (shown in yellow) consist of ground-signal-ground input and output pads and a 10μm-wide, Au transmission line. The upper structure in Fig. 42 is for de-embedding the pad parasitic values from the s-parameter measurements of the lower structure which includes the full transmission line over the

magnetic film. The top metal thickness is 2µm separated from the FM layer by 2µm of SU-8. The 4600Å thick FM layer is separated from the bottom ground plane by 11µm of SU-8. The bottom Au ground plane is 1µm thick.

The transmission lines were tested using an Agilent Vector Network Analyzer by applying a small signal at the input port from 10MHz to 20GHz to obtain the two-port, s-parameters of the structures. The distributed R, L, C and G parameters versus frequency were calculated from these s-parameters according to [**24**]. The inductance for 10µm-wide transmission lines with and without FM material are shown in Fig. 43. As much as

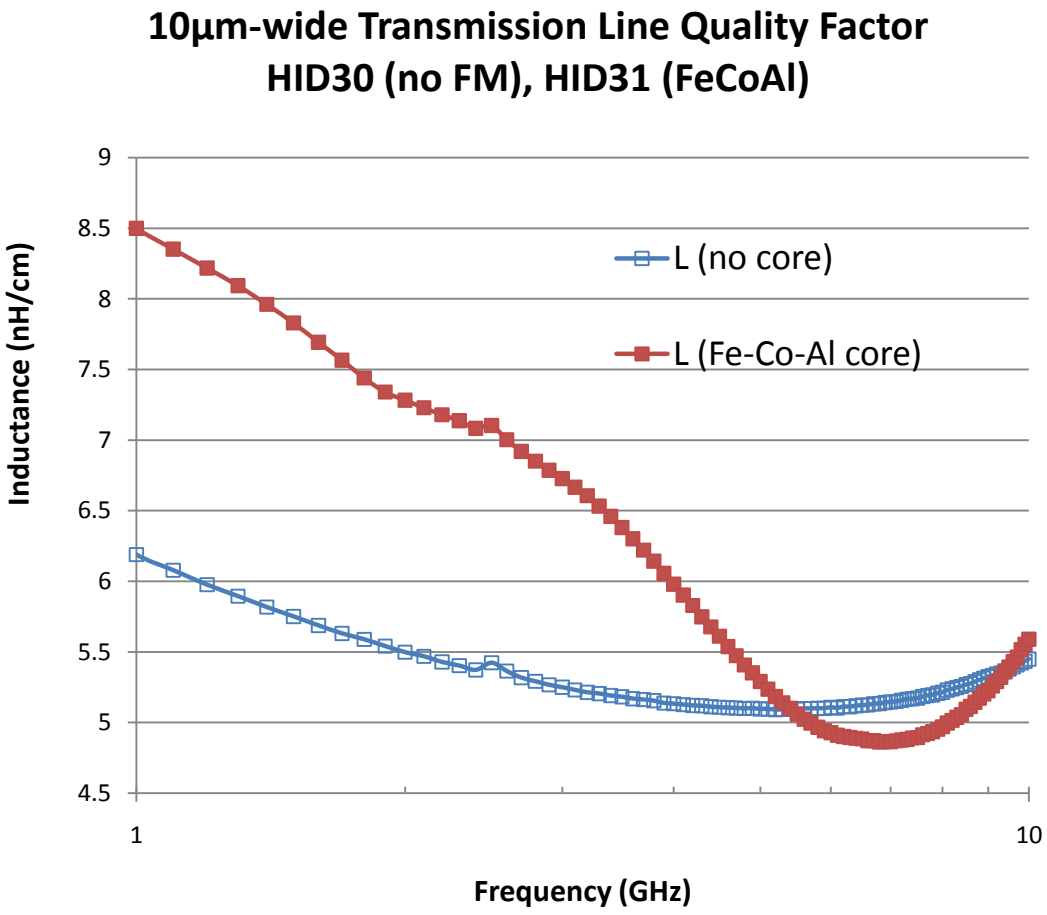

Fig. 43 Extracted inductance of 10um-wide transmission lines with and without FeCoAl FM material beneath them.

a 37% improvement in inductance was noted in the range of 10MHz to 2.6GHz. The no FM transmission line resonated at 19.7GHz, whereas the transmission line with FeCoAl beneath resonated at 11.7GHz (not shown in the graph). The quality factors for these two transmission lines are shown in Fig. 44 and clearly the FM material significantly introduces significant eddy current losses due to the conductivity of the film, above the 2.6GHz range. Below that range, the Q is slightly better than the no FM transmission line. The Q reached a value of zero at 14GHz and 21GHz for the FM and no FM transmission lines, respectively (not shown in the graph to provide clarity up to 10GHz).

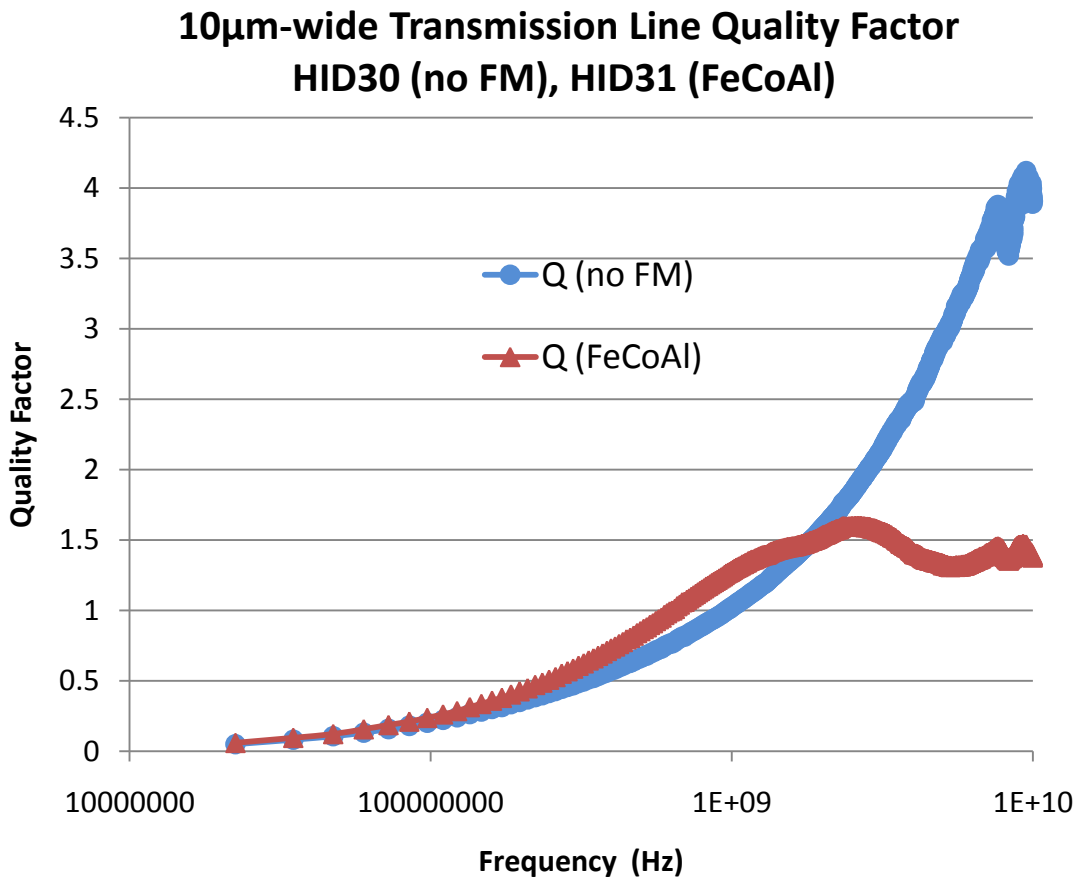

Fig. 44 Quality factor for 10um-wide transmission lines with and without FeCoAl beneath them.

2. Fabrication of Solenoid with FeCoAl Core

The fabrication process was similar to that for SU-8 core solenoids except for a modification to the POST level. One additional BSG wafer (labeled SOL33) was processed with FeCoAl as the core of the solenoid DOE previously studied. Also, a second BSG wafer (labeled SOL34) was processed in the standard manner, but without the FM layer included. The process to fabricate this final FM-core wafer is described in the following. The BSG wafer was first processed up through the M1 (metal 1) plating step as in the standard solenoid fabrication technique. The SU-8 was removed using CF_4/O_2 plasma and then the Au seed layer was etched with KI solution. A 2.5μm layer of SU-8 was blanketed onto the wafer, cured and patterned with the POST mask. The wafer was then sputter coated with 4600Å of FeCoAl. An etching technique was developed to clear the photoresist patterned magnetic film through the use of ten control wafers. These wafers had similar thicknesses of FeCoAl and a combination of wet and dry etching was used to clear the film without damaging the SU-8 beneath. The DOE for this etch characterization resulted in a dry/wet process to clear the FeCoAl. A "blast etch" using a Plasma-Therm Inductively Coupled Plasma Reactive Ion Etch tool was followed by a 3 minute wet etch in HNO_3:H_3PO_4:H_2O_2. The blast etch was performed at 5mTorr with 15sccm of Cl_2 and 5 sccm of Ar at 150W of reactive ion etching power and 750W of inductively coupled plasma power. It was determined that this "blast etch" was necessary to condition the FM surface such that the wet etch would subsequently initiate uniformly across the wafer surface. Following the FM layer definition, another 2.5μm SU-8 via layer was blanketed over the wafer and patterned with the POST photo mask. At this point the standard solenoid processing resumed with the deposition of the second Au seed

layer and electroplating of the top metal. The completed solenoid with ferromagnetic core is shown in Fig. 45. This figure shows a five-turn solenoid with 10μm-wide traces and 20μm center-to-center spacing, on a BSG substrate.

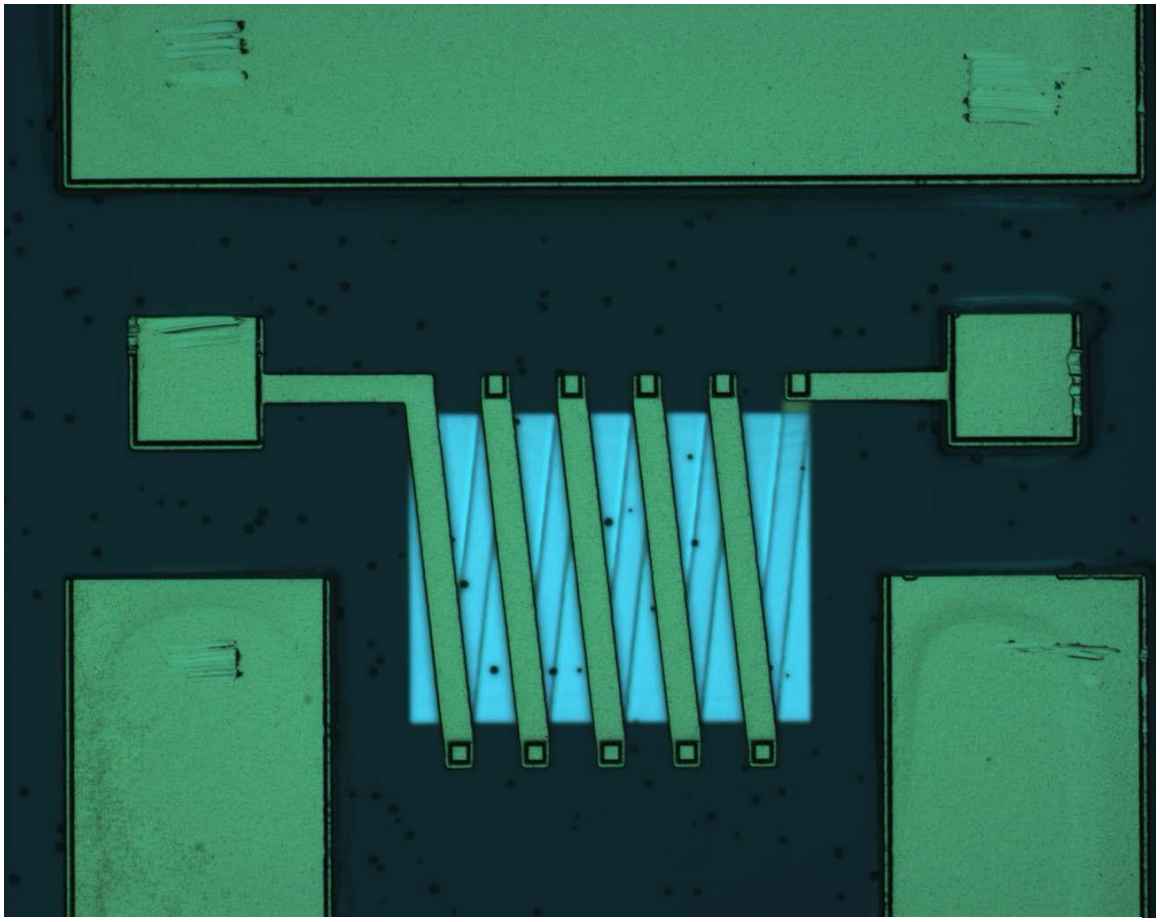

Fig. 45 Solenoid with FeCoAl core fabricated on a BSG substrate.

3. Testing of Solenoid with FeCoAl Core

The inductance, quality factor and AC resistance of the widest solenoid series (W=145μm, D=10μm through 50μm, 10-turns) was determined from s-parameter measurements as previously described. Both the no FM-core and FeCoAl-core solenoids were tested. The variation in inductance over the frequency range of 1GHz to 10GHz for three solenoids of different lengths, with and without a FM core is shown in Fig. 46. The

largest increase in inductance for the FeCoAl-core solenoid occurred for the geometry with the tightest turn-to-turn spacing where *D* was 10µm. The percentage increase in inductance varies from 8-15% over the 1-10GHz range. There is only a 2-9% increase in

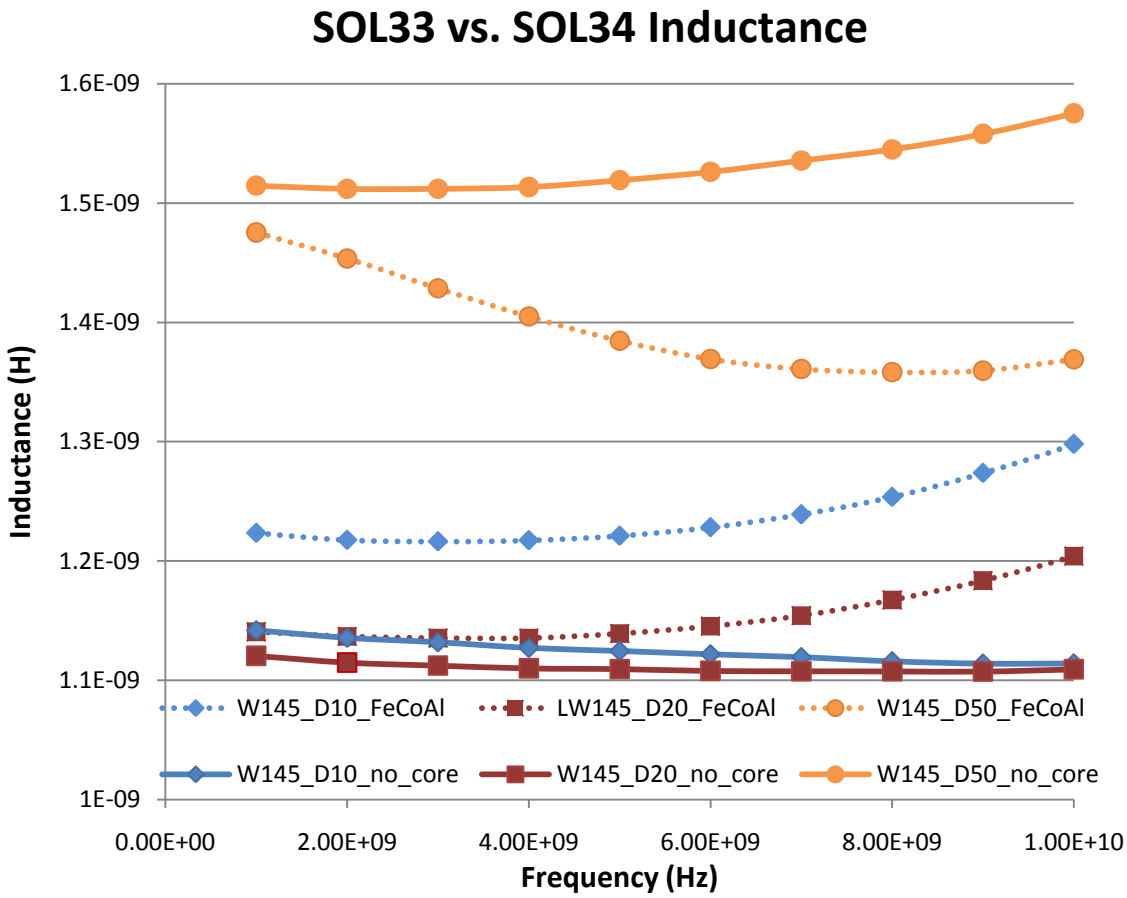

Fig. 46 Inductance of largest width solenoid series for no FM-core and FeCoAl-core solenoids.

inductance for the next wider spaced coil (*D*=20µm). The increase in inductance diminishes to zero for the coil with *D* of 30µm (not shown in the figure), then to a decrease in inductance for *D* of 40µm and *D* of 50µm. The figure shows the latter case where the decrease is most significant (2-14%). These results indicate the optimum turn-to-turn spacing is 10µm to achieve a higher inductance when a core is utilized. The physical significance of this result is that eddy current losses induced in the FM core

material dominate the rate in inductance degradation. The widely-spaced coils require larger rectangular cores that exhibit a higher degree of eddy currents and thus lower inductance values.

The eddy current losses induced in the FM material also result in a significant change in the quality factor compared with the no-FM solenoids as shown in Fig. 47.

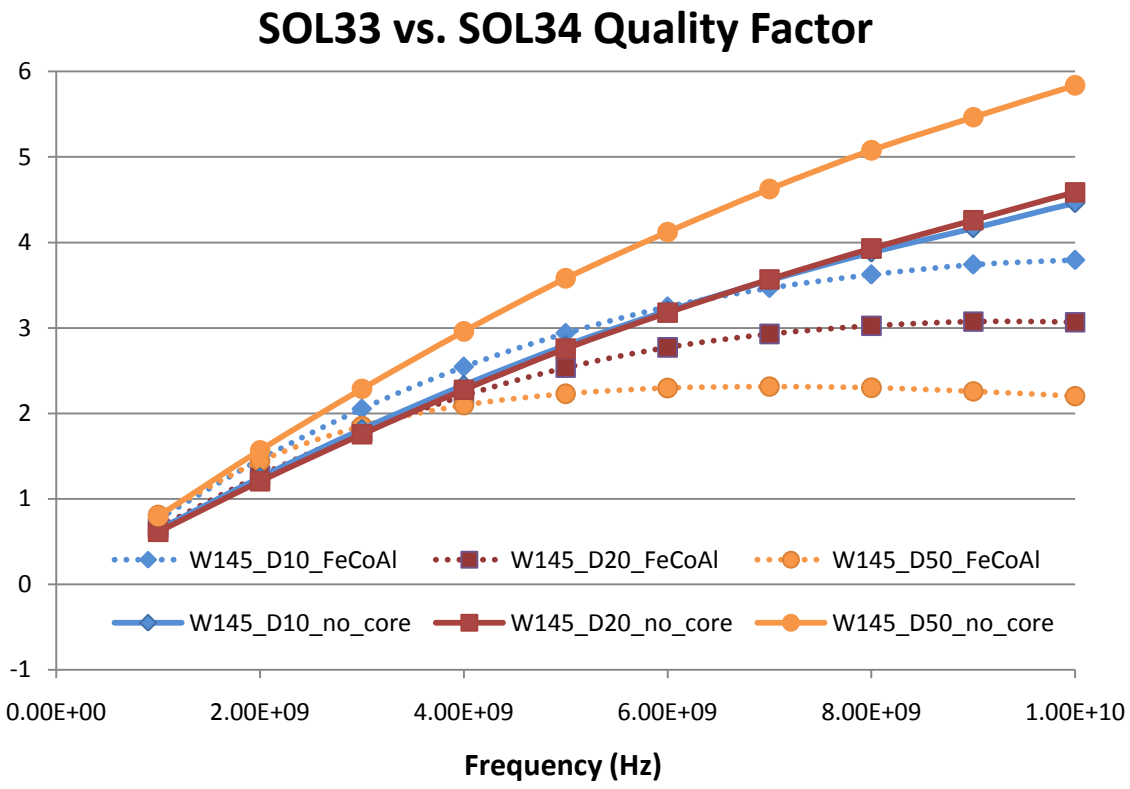

Fig. 47 Quality factor for three solenoid designs with and without FM FeCoAl core.

Note that the quality factor for the no-FM solenoids increases with increased turn-to-turn spacing, as previously determined. However, the quality factor decreases with increased turn-to-turn spacing for the FeCoAl-core solenoids. This result is due to the higher AC resistance for the solenoids with a FM core.

Since the magnetic core was not preferentially magnetized along its hard axis (the axis parallel with the induced magnetic field of the coil), the effective permeability of the

FeCoAl film was only influenced by the shape anisotropy field [**16**]. Additional enhancement of the inductance and quality factor can be attained through magnetization of the core along the soft axis.

H. Hybrid Circuit Development Using SU-8 Interposer Layer with Active GaN Field Effect Transistor

In an effort to evaluate the RF performance of SU-8 as an interposer layer, a process was developed to incorporate AlGaN/GaN high electron mobility (HEMT) field effect transistors (FETs) into a 3-D circuit. Fabrication of the hybrid circuit (shown in Fig. 48) started with the definition of 100µm deep pockets in a 100mm diameter, <100>

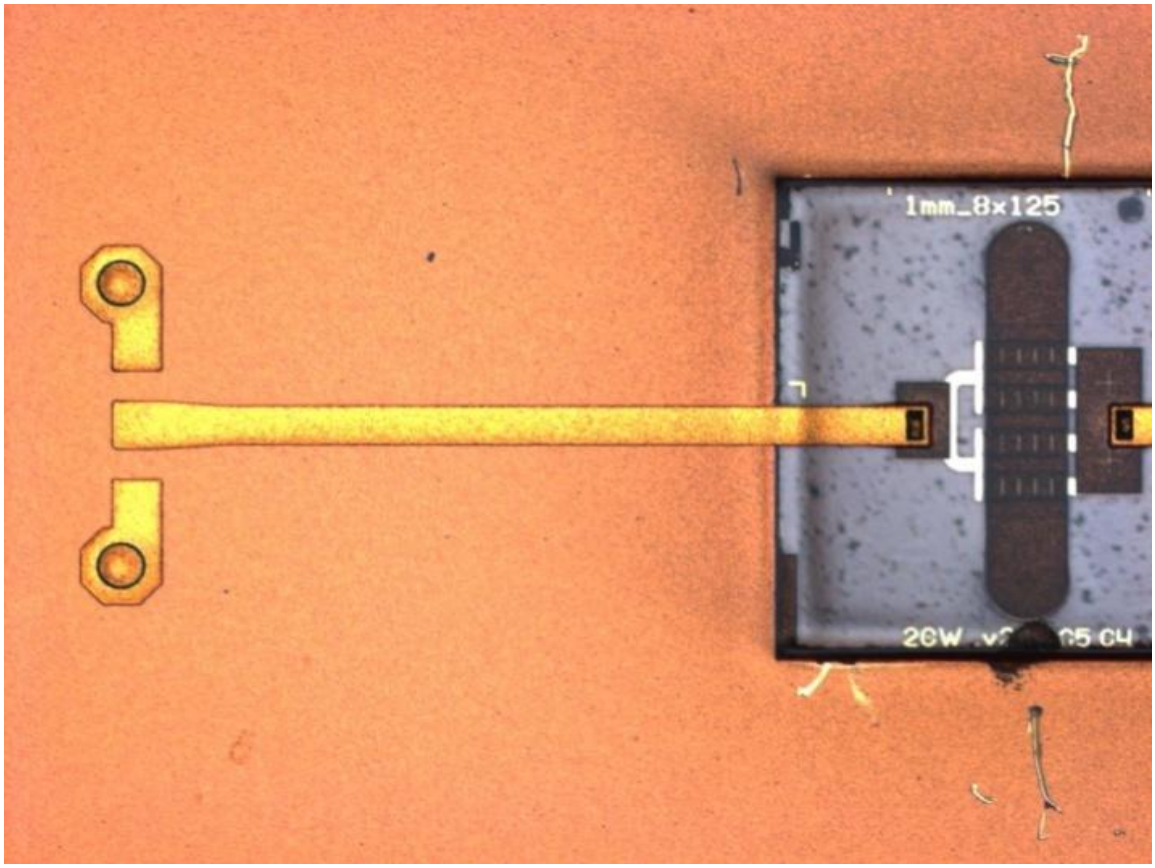

Fig. 48 Embedded GaN chiplet with gold transmission line gate feed over 19µm thick SU-8 interposer layer.

silicon substrate, volumetrically sized to match the HEMT chiplet (thinned die with SiC

vias and backside ground). A Plasma-Therm Versaline DRIE employing the Bosch passivate and etch process cut the pockets at 6µm's per minute. A uniform, 2µm thick gold ground layer was plated across the entire silicon wafer. The known-good HEMT chiplets were bonded into the pockets using silver epoxy resulting in a chiplet surface that was flush with the silicon's metal ground plane. A 19µm thick SU-8 layer was dispensed on top of the wafer and patterned with via holes down to the top-side gate and drain contacts of the HEMT. The vias and transmission lines were electroplated with 5µm's of gold. The circuits were tested using a DC/RF test station and an HP 8510 network analyzer. The HEMT's cutoff frequency exhibited no degradation after integration and was accurately matched to the transmission line feeds. Fig. 49 shows that the gain for the

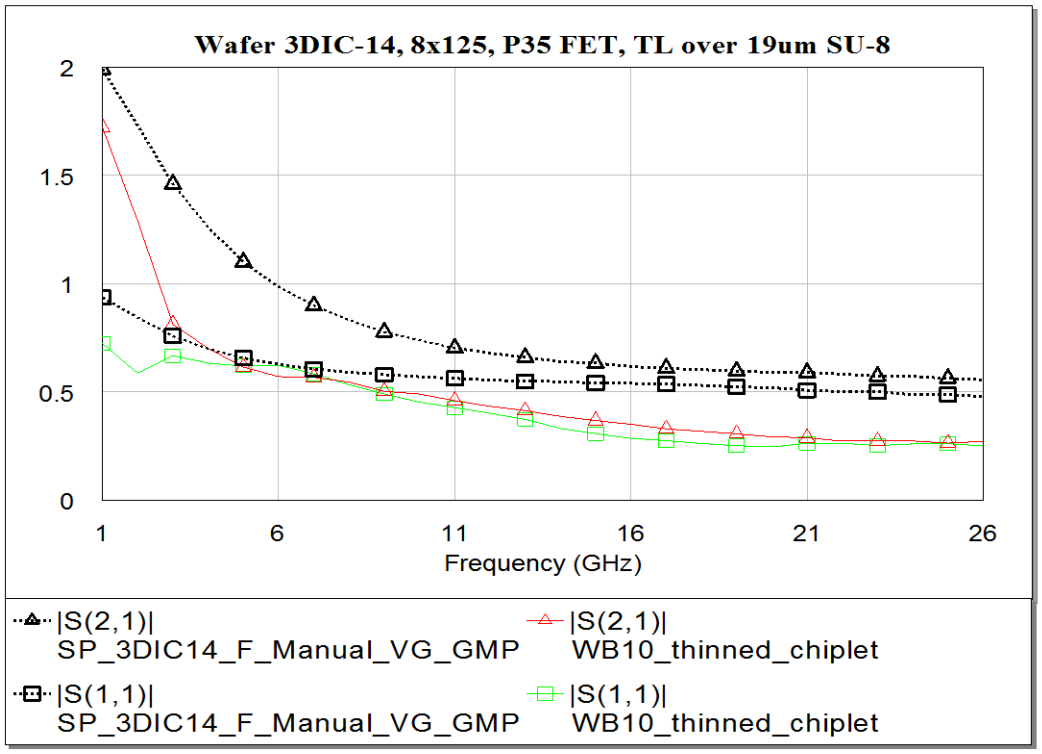

Fig. 49 Gain versus frequency for the GaN chiplet (wafer level data labeled WB10) and the chiplet embedded into SU-8 (labeled 3DIC14).

embedded chiplet actually increased. The cause of this increase is under investigation but may be due to the contact resistance of the ground-signal-ground probes to the chiplet during s-parameter measurements, since both ground pads could not contact the top-side bridge ground simultaneously.

Besides the active chip integration with transmission lines over SU-8, an X-band filter layout shown in Fig. 50 was simulated and fabricated over the SU-8 layer. Here, the simulated data closely matched the measured data, also shown in Fig. 50, indicating that the larger 75µm vias sufficiently grounded the structure.

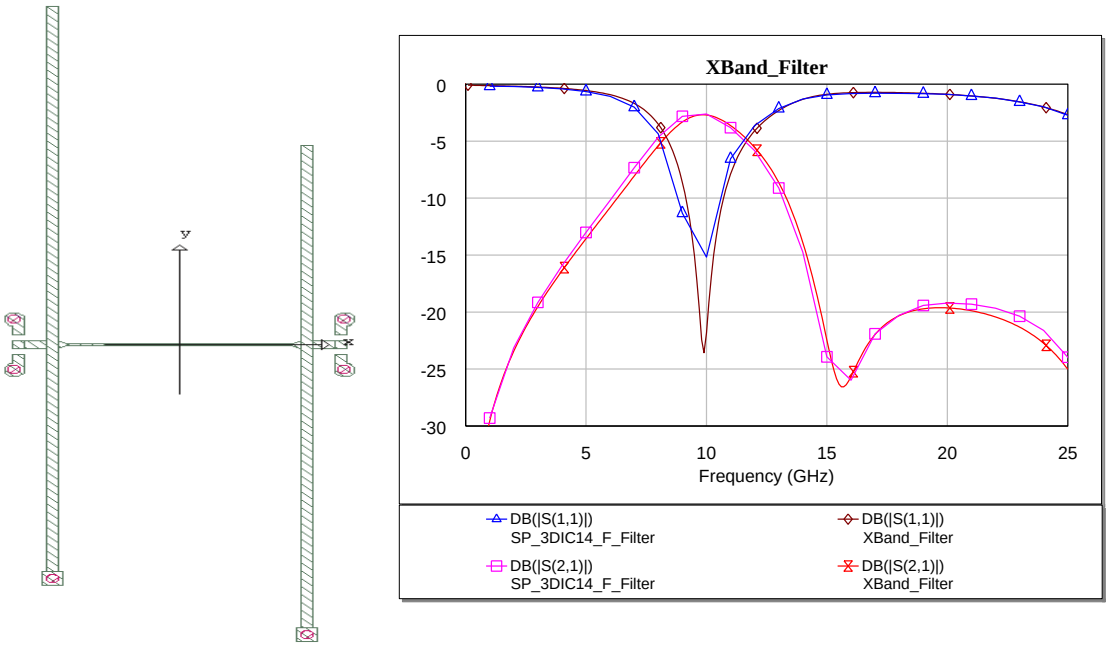

Fig. 50 X-band filter with simulated (labeled XBand_Filter) versus measured gain versus frequency.

V. Summary

A. Conclusions

The Matlab inductor model generated herein provides an accurate representation of the fabricated solenoid designs. Simulation and RF test data verified that tightly-spaced solenoid turns are not the optimum geometrical configuration necessary to achieve more uniform inductance versus frequency or higher quality factors when a FM core is not used. However, when a FM core is used in the solenoid, more tightly-spaced turns result in higher inductance values and higher quality factor. The resonant frequency does suffer by a significant reduction when a core is used. The FeCoAl core material used here provided as much as a 37% increase in inductance from 10MHz to 2.6GHz in the transmission line configuration. When employed as a solenoid core, the FeCoAl resulted in as much as a 2-14% inductance increase from 1GHz to 6GHz. Until a material with extremely high resistivity and high permeability, and potentially a high ferromagnetic resonance frequency is developed, this solenoid design will only be advantageous at sub-GHz frequencies. The simulated GaN HEMT circuit parameters closely matched the test results of the fabricated circuit. Finally, the SU-8 processing is compatible with both active and passive components and promises to be a suitable interposer layer for prototyping microwave circuits using known good chips, thereby significantly reducing the costs of hybrid integration.

B. Contributions of this Dissertation

This dissertation focused on the design of integrated inductors, specifically those of the solenoid geometry, primarily since the magnetic field can be confined within the turns of the coil. Compared with existing solenoid technologies, the largest solenoid in the DOE presented here achieved the highest f_{max}, Q_{max}, L combination to date (19GHz, 15, 1.5nH), respectively. Given this geometry, a high quality ferromagnetic material acting as the core of the solenoid can significantly enhance the inductance and quality factor. The modeling of this structure is very complicated in nature due to the proximity effects of adjacent windings and other components. Software packages such as Ansoft's HFSS, full-wave electromagnetic field simulator and CoventorWare's MemHenry simulator will perform analyses; however, they are expensive and are very time consuming. Therefore, a more tailored model for the solenoid geometry and one which allows for modification of the core material characteristics was developed. The frequency-dependent model was verified through fabrication of an array of solenoid designs, tested to determine the AC inductance and resistance, and quality factor for each design. This feedback loop was also verified through MemHenry simulations.

Additional work involved the evaluation of ferromagnetic materials such as NiFe and FeCoAl and their incorporation into the solenoid core. A DC magnetron sputtering technique was developed to deposit the FeCoAl thin ferromagnetic film which was evaluated as the magnetic core of transmission line structures as well as solenoids. SQUID Magnetometry measurements were also employed for the first time on this film to determine it magnetic characteristics. Also, a novel dry/wet etching process was developed using an inductively coupled plasma blast etch to enhance the etch rate of

FeCoAl. During the solenoid fabrication process, a deep reactive ion etching (DRIE) process was developed to remove the substrate beneath the solenoids which were built on a silicon wafer. This process helped verify the inductor model for suspended solenoids and was also beneficial in developing a hybrid integration technique where gallium nitride, high electron mobility transistor (GaN HEMTs) chips were placed into DRIE pockets on a silicon wafer and then interconnected with transmission lines and vias formed in a layer of SU-8 patterned over the embedded chips. Ultimately, these inductor building blocks will be combined with active chips in SU-8 to attain a new approach to high speed, high quality and rapidly integrated circuit designs and fabrication.

C. Future Work

The road has been paved for the potential to make more significant contributions towards the development of integrated passive inductors with higher quality factor and inductance values in a smaller volume footprint. Additional solenoid model optimization, including a ferromagnetic core, would require significant effort, but given the complexity and cost of existing finite element simulators, would be very beneficial to designers. The next logical step in solenoid development is to enhance the performance of core materials by reducing their magnetic loss characteristics and lowering their conductivity. FeCoAl is a promising material that needs further examination and optimization.

VI. References

[1] (2008, July) ifixit. [Online]. http://www.ifixit.com

[2] Kohie Fujii, John Stanback, and Henrik Morkner, "DC to 85GHz TWA and Ka-band 4.9W Power Amplifier Using an Optical Lithography Based Low Cost PHEMT Process," Avago Technologies, White Paper 2006.

[3] Richard K. Ulrich and Leonard W. Schaper, Eds., *Integrated Passive Component Technology*. Piscataway, NJ: IEEE Press, 2003.

[4] A. E. Ruehli, "Inductance Calculations in a Complex Integrated Circuit Environment," *IBM J. Res. Develop.*, pp. 470-481, Sep. 1972.

[5] E. B. Rosa, "The self and mutual inductances of linear conductors," *Bulletin of the Bureau of Standards*, vol. 4, pp. 301-344, Jan. 1908.

[6] John D. Kraus, *Electromagnetics*, 3rd, Ed. New York: McGraw-Hill Book Company, 1984.

[7] Melia Fulvio, *Electrodynamics*. Chicago, United States of America: The University of Chicago Press, 2001.

[8] F. W. Grover, *Inductance Calculations Working Formulas and Tables*. New York, USA: D. Van Nostrand Company, Inc., 1946.

[9] C. Hoer and C. Love, "Exact inductance equations for rectangular conductors with applications to more complicated geometries," *J. Res., Nat. Bur. Stand. C.*, vol. 69C,

no. 2, pp. 125-137, Apr.-Jun. 1965.

[10] H. M. Greenhouse, "Design of Planar Rectangular Microelectronic Inductors," *IEEE Trans. on Parts, Hybrids and Packaging*, vol. PHP-10, no. 2, pp. 101-109, Jun. 1974.

[11] J. -T. Kuo, K. -Y. Su, T. -Y. Liu, H. -H. Chen, and S. -J. Chung, "Analytical Calculation for DC Inductances of Rectangular Spiral Inductors with Finite Metal Thickness in the PEEC Formulation," *IEEE Microwave and Wireless Components Letters*, vol. 16, no. 2, pp. 69-71, Feb. 2006.

[12] S. Jenei, B. Nauwelaers, and S. Decoutere, "Physics-Based Closed-Form Expression for Compact Modeling of Integrated Spiral Inductors," *IEEE J. Solid-State Circuits*, vol. 37, no. 1, pp. 77-80, Jan. 2002.

[13] A. M. Niknejad and R. G. Meyer, "Analysis, Design and Optimization of Spiral Inductors and Transformers for Si RF IC's," *IEEE J. Solid State Circuts*, vol. 33, no. 10, pp. 1470-1481, Oct. 1998.

[14] W. T. Weeks, L. L. Wu, M. F. McAllister, and A. Singh, "Resistive and inductive skin effect in rectangular conductors," *IBM J. Res. Develop.*, vol. 23, pp. 652-660, Nov. 1979.

[15] Burhan Bayraktaroglu, "Micromachined Microwave Integrated Circuits," in *Topical Workshop on Heterostructure Microelectronics*, Bankoku-Shinryokan Okinawa, 2003, p. 23.

[16] Y. Zhuang, M. Vroubel, B. Rejaei, and J. N. Burghartz, "Integrated RF inductors with micro-patterned NeFe core," *Solid-State Electronics*, vol. 51, pp. 405-413, Feb. 2007.

[17] M. Vroubel, Y. Zhuang, B. Rejaei, and J. N. Burghartz, "Investigation of Microstrips with NiFe Magnetic Thin Film (II): Modeling," *Transaction of the Magnetic Society of Japan*, vol. 2, no. 5, pp. 371-376, December 2002.

[18] Yung-Wang Peng, Fan-Bean Wu, Shangong Li, Cheng-Lun Kuo, and Jeng-Gong Duh, "Fabrication and high frequency magnetic characterization of FeCoAl Ternary Thin Films," *Physica Status Solidi*, vol. 12, pp. 4129-4132, December 2007.

[19] D. M. Fang, Y. Zhou, X. M. Jing, X. L. Zhao, and X. N. Wang, "Modeling, optimization and performance of high-Q MEMS solenoid inductors," *Microsyst Technol*, vol. 14, no. 2, pp. 185-191, Feb. 2008.

[20] Gabriele Grandi, Marian K. Kazimierczuk, Antonio Massarini, Ugo Reggiani, and Guiseppe Sancineto, "Model of Laminated Iron-Core Inductors for High Frequencies," *IEEE Transactions on Magnetics*, vol. 40, no. 4, pp. 1839-1845, July 2004.

[21] C. P. Yue and S. S. Wong, "On-Chip Spiral Inductors with Patterned Ground Shields for Si-Based RF IC's," *IEEE J. Solid-State Circuits*, vol. 33, no. 5, pp. 743-752, May 1998.

[22] H. Sagkol, S. Sinaga, J. N. Burghartz, B. Rejaei, and A. Akhnoukh, "Thermal

Effects in Suspended RF Spiral Inductors," *IEEE Electron Device Letters*, vol. 26, no. 8, pp. 541-543, Aug. 2005.

[23] Dok Won Lee, Kyu-Pyung Hwang, and Shan X. Wang, "Design and Fabrication of Integrated Solenoid Inductors with Magnetic Core," in *Electronic Components and Technology Conference*, Lake Buena Vista, 2008, pp. 701-705.

[24] W. R. Eisenstadt and E. Yungseon, "S-Parameter-Based IC Interconnect Transmission Line Characterization," *IEEE Transactions on Components, Hybrids, and Manufacturing Tehcnology*, vol. 15, no. 4, pp. 483-490, August 1992.

[25] Y. Zhuang, B. Rejaei, E. Boellaard, and J.N. Burghartz, "Investigation of Microstrips with NiFe Magnetic Thin Film (I): Experiment," *Transactions of the Magnetic Society of Japan*, vol. 2, no. 5, pp. 367-370, December 2002.

VII. Appendix A: Solenoid Model MATLAB Code

```
%Solenoid Inductance Function - PhD Dissertation Research Robert Fitch
%Contains multiple Mutual Inductance Equations for various segment
spacings
%function[f,g,H]=myfun_Fitch_SU8(x)
clc
clear all
global mu I PP JJ Lt C Ct MM LL CC ZZ L M Q Rtrace Rtrdc Xtrace Z Zmag
phi...
    delta freq ep k xx1 xx2 xx3 xx4 xx5 xx6 xx7 xx8 xx9 xx10 xx11 p ...
    Ztotal Ltotal Qtotal scalefactor_f
i=0;j=0;kp=0;kpp=0;kppp=0;s=0;l=0;u=0;v=0;alpha=0;beta=0;del=0;gamma=0;
M=0;L=0;theta=0;LfromZ=0;Q=0;Zmag=0;phi=0;Q3D=0;L3DfromZ=0;Z3Dtotal=0;
%rho_m=0.0671                              %nickel resistivity
%rho_m=0.0168;                             %copper resistivity
rho_m=0.0208;                              %gold resistivity 0.022 ohm-
um; measured 0.0208 ohm-um
for scalefactor_f=1:1:15
%%%%%%%%%%%%Test IC's%%%%%%%%%%%%%%%%%%%%%%%%%
k=0;q=0;
for scalefactor_W=145;            %Y value
    q=q+1;
for scalefactor_D=10:10:50;              %X value
        x=0;freq=0;p=1;
        %scalefactor_W=300;
        scalefactor_H=9.1;  %was 9.1
        %scalefactor_D=60;
        %scalefactor_f=10;
        scalefactor_N=10;    %was 10
        scalefactor_mu_core=1.18; %was 1.08
        %scalefactor_mu_core=0.8-(scalefactor_f-1)*0.008; %was 1.08
        scalefactor_w=6.3;  %was 7.3
        scalefactor_t=4.5; %was 4.5
        scalefactor_d=6.3; %was 7.3
        scalefactor_mu_metal=0.99996;   %was 0.99996
        %scalefactor_mu_metal=0.4-(scalefactor_f-1)*0.0276; %was
0.99996
        scalefactor_SU8=5.3; %was 6.5
        x(1)=1*scalefactor_W;        x(2)=1*scalefactor_H;
x(3)=1*scalefactor_D;
        x(4)=2e9*pi()*scalefactor_f;
x(5)=1*scalefactor_mu_core;x(6)=1*scalefactor_N;
        x(7)=1*scalefactor_w;        x(8)=1*scalefactor_t;
x(9)=1*scalefactor_d;
        x(10)=1*scalefactor_mu_metal;x(11)=1*scalefactor_SU8;
        scalefactor_ep=3.9; %was 3.9 for SU-8
        %scalefactor_ep=3.9+(scalefactor_f-1)*(0.155); %was 3.9
        mu=4*pi()*1e-13;   ep=scalefactor_ep*8.854e-18;   I=1e-6;
M=0;   L=0;
%%%%%%%%%%%%%%%%%%%%%%%%%%%%%%%%%%%%%%%%%%%%
        %rho_m=0.02+(scalefactor_f-1)*2.04e-3
        %rho_m=0.1+(scalefactor_f-1)*1.04e-3;
%%%%%%%%%Scale Factor For Variable Initial Conditions and Un-normalized
Variables
%    wmin=400;                wmax=400;
```

```
%     x(1)=(wmax-wmin)*x(1)+wmin;
%     hmin=40;                  hmax=40;
%     x(2)=(hmax-hmin)*x(2)+hmin;
%     dmin=140;                  dmax=140;
%     x(3)=(dmax-dmin)*x(3)+dmin;
%     omegamin=2*pi()*scalefactor_f*p*1e9;
omegamax=2*pi()*scalefactor_f*p*1e9;
%     x(4)=(omegamax-omegamin)*x(4)+omegamin;
%     mu_core_min=1;            mu_core_max=1;
%     x(5)=(mu_core_max-mu_core_min)*x(5)+mu_core_min;
%     nturns_min=7;             nturns_max=7;
%     x(6)=(nturns_max-nturns_min)*x(6)+nturns_min;
%     wsmin=50;                 wsmax=50;
%     x(7)=(wsmax-wsmin)*x(7)+wsmin;
%     tsmin=5;                  tsmax=5;
%     x(8)=(tsmax-tsmin)*x(8)+tsmin;
%     dsmin=100;                 dsmax=100;
%     x(9)=(dsmax-dsmin)*x(9)+dsmin;
%     mu_metal_min=1;           mu_metal_max=1;
%     x(10)=(mu_metal_max-mu_metal_min)*x(10)+mu_metal_min;
%     t_SU8_min=10;           t_SU8_max=10;
%     x(11)=(t_SU8_max-t_SU8_min)*x(11)+t_SU8_min;
%%%%%%%%%%%%%%%%%%%%%%%%%%%%%%%%%%%%%%%%%%%%%%%%%%%%%%%%%%%%%%%%%%%%%%%%%%%%
%%%%%%%%%%%%%
k=k+1;                              %Counter for myfun_mult iterations
%x(6)=round(x(6));                  %Make whole number of turns
%Constraint Functions
delta(scalefactor_f)=sqrt(2*rho_m/(mu*x(10)*x(4)));                %Skin
depth

%Solenoid Mutual Inductance Functions
S=(4*x(6));                                  %#of segments
for i=1:S-2;
    for j=i+2:S;
        if mod(i,2)~=0;                    %i is odd, vertical posts
            if mod((i+j),2)==0;            %Calculate every other pair
                kp=(j-i)/4;
                if mod((i+j),4)==0
                    kpp=1;
                else
                    kpp=0;
                end
            s=sqrt((kp*x(3))^2+(kpp*x(1))^2);   %s is the distance
between posts
            %Determine which Mutual Inductance equation (2), (3) or (4)
to
            %use depending on the ratio of H/s
            if x(2)/s >= 10;
                 M(i,j)=2e-13*x(5)*(log(2*x(2)/s)-1+x(2)/s-
0.25*((x(2)/s)^2));%Grover's formula
            else if x(2)/s< 0.1;
                %M(i,j)=2e-13*x(5)*(log(2*x(2)/s)-1+x(9)/s-
0.25*((x(9)/s)^2));
                 M(i,j)=2e-13*x(5)*x(2)*(0.5*x(2)/s)*(1-
(1/12)*((x(2)/s)^2)+(1/40)*((x(2)/s)^4));%Grover's formula
                 %M(i,j)=1e-13*x(5)*(2*x(2)*asinh(x(2)/s)-
2*sqrt(x(2)^2+s^2)+2*s);%Rosa's filament formula
```

```
                else
                 M(i,j)=2e-
13*x(5)*x(2)*(log(x(2)/s+sqrt(1+(x(2)/s)^2))-
sqrt(1+(s/x(2))^2)+s/x(2));%Grover's formula
                 %M(i,j)=2e-13*x(5)*(x(2)*asinh(x(2)/s)-
2*sqrt(x(2)^2+s^2)+2*s);%Rosa's filament formula
                end
            end
            M(i,j)=(-1)^kpp*M(i,j);
            else
            M(i,j)=0;
            end
%         if j-i>4        %only count adjacent turns
%             M(i,j)=0;
%         end
        end

        if mod(i,2)==0;                  %i is even, horizontal bars
            if mod((i+j),2)==0;          %Calculate every other pair
                kp=(j-i)/4;
                eps=2*atan(x(3)/(2*x(1)));
                eps_deg=eps*360/(2*pi());
                tau=asin(x(1)/l);
                if mod((i+j-2),4)==0;    %non-parallel bars
                    kppp=1;
                    %l=sqrt(x(1)^2+(x(3)/2)^2);  %l is the length of
horizontal bars
                    l=sqrt((x(1)+x(7))^2+((x(3)+x(9))/2)^2);
                    u=(kp-0.5)*l;
                    v=u;
                    R1=sqrt(x(2)^2+2*(u+l)^2-2*(u+l)^2*cos(eps));
                    R2=sqrt(x(2)^2+(u+l)^2+u^2-2*u*(u+l)*cos(eps));
                    R3=sqrt(x(2)^2+2*u^2-2*u^2*cos(eps));
                    R4=sqrt(x(2)^2+u^2+(u+l)^2-2*u*(u+l)*cos(eps));

omega=atan((x(2)^2*cos(eps)+(u+l)^2*((sin(eps))^2))/(x(2)*R1*sin(eps)))
...
                     -
atan((x(2)^2*cos(eps)+u*(u+l)*((sin(eps))^2))/(x(2)*R2*sin(eps)))...

+atan((x(2)^2*cos(eps)+u^2*((sin(eps))^2))/(x(2)*R3*sin(eps)))...
                     -
atan((x(2)^2*cos(eps)+u*(u+l)*((sin(eps))^2)/(x(2)*R4*sin(eps))));
                   M(i,j)=2e-
13*x(5)*cos(eps)*((u+l)*atanh(l/(R1+R2))+(u+l)*atanh(l/(R1+R4))...
                    -u*atanh(l/(R3+R4))-u*atanh(l/(R2+R3)))-1e-
13*cos(eps)*omega*x(2)/sin(eps);
                else                     %parallel bars
                    %check for overlap of bars
                    kppp=0;
                    %l=sqrt(x(1)^2+(x(3)/2)^2); %l is the length of
horizontal bars
                    l=sqrt((x(1)+x(7))^2+((x(3)+x(9))/2)^2);
                    theta=eps/2+atan(((j-i-2)/4)*x(3)/x(1));
%angle between i and j opposite ends
                    theta_deg=theta*360/(2*pi());
                    s=kp*x(3)*sin(tau);
```

```
                    if theta > pi()/2;
                        del= abs(l-kp*x(3)*cos(tau));
                    else
                        del= -abs((kp*x(3)*cos(tau)-l));
                    end
                    beta=l+del;
                    gamma=beta;
                    alpha=2*l+del;
                    M(i,j)=1e-13*x(5)*(2*l*asinh(l/s)-
2*sqrt(l^2+s^2)+2*s);%Rosa parallel filaments
                    %M(i,j)=1e-13*x(5)*(alpha*asinh(alpha/s)-
beta*asinh(beta/s)...
                    %-gamma*asinh(gamma/s)+del*asinh(del/s)-
sqrt(alpha^2+s^2)...
                    %+sqrt(beta^2+s^2)+sqrt(gamma^2+s^2)-
sqrt(del^2+s^2));
                end
                    M(i,j)=(-1)^(kppp)*M(i,j);
            else
                M(i,j)=0;
            end
%             if j-i>4        %only count adjacent turns
%                M(i,j)=0;
%             end
        end
    end
end
MMatrix(:,:,k)=M;
M=sum(M);
M=sum(M);
M=2*M;
MVector(k)=M;

%Solenoid Self-Inductance Function
  length_v=(x(6)*2)*x(2);                    %Length of all vertical
segments corrected for right angles
  length_h=(x(6)*2)*(l);             %Length of all horizontal segments
corrected for right angles
  sol_length=length_v+length_h;
  %LH=x(5)*2e-13*l*(log(2*l/(2*0.447))-1+(2*0.447)/l); %DC Self Rosa
  LH=x(6)*x(5)*2e-
13*l*(log(2*l/(x(8)+x(9)))+0.50049+(x(8)+x(9))/(3*l)); %Greenhouse
  %LH=x(6)*x(5)*2e-
13*l*(log(2*l/(x(8)+x(9)))+0.5+x(10)*0.2235*(x(8)+x(9))/(l*x(5)));
%Horizontal segments
 %LV=x(6)*x(5)*2e-
13*x(2)*(log(2*x(2)/(x(7)+x(9)))+0.5+x(10)*0.2235*(x(7)+x(9))/(x(2)*x(5
)));  %Vertical segments
 LV=x(6)*x(5)*2e-
13*x(2)*(log(2*x(2)/(x(7)+x(9)))+0.50049+(x(7)+x(9))/(3*x(2)));
%Greenhouse
 %LV=x(5)*2e-13*x(2)*(log(2*x(2)/(2*0.447))-1+(2*0.447)/x(2)); %DC Self
Rosa
 L=2*(LH+LV);
 %L=L_sol;
 %LVector(k)=L;
```

```
 Lt_noskin=L+M;                                          %DC Total
Inductance
 Lt=Lt_noskin;
 LtperLength=Lt/sol_length;
 LS=Lt;
 %Solenoid Self-Inductance Function accounting for skin effect
%  xd=delta(scalefactor_f)/(0.2235*(x(8)+x(9)));
%  if xd<0.5
%      Xfactor=0.4372*xd;
%  end
%  if xd >= 0.5
%      if xd <= 1
%      Xfactor=0.0578*xd+0.1897;
%      end
%  end
%  if xd>1
%      Xfactor=0.25;
%  end
%
%  LH_delta=x(10)*(0.25-Xfactor);
%  LHd=x(6)*x(5)*2e-
13*l*(log(2*l/(x(8)+x(9)))+0.5+x(10)*0.2235*(x(8)+x(9))/(l-
LH_delta)*x(5));    %Horizontal segments
%
%  xd=delta(scalefactor_f)/(0.2235*(x(7)+x(9)));
%  if xd<0.5
%      Xfactor=0.4372*xd;
%  end
%  if xd >= 0.5
%      if xd <= 1
%      Xfactor=0.0578*xd+0.1897;
%      end
%  end
%  if xd>1
%      Xfactor=0.25;
%  end
%
%  LV_delta=x(10)*(0.25-Xfactor);
%  LVd=x(6)*x(5)*2e-
13*x(2)*(log(2*x(2)/(x(7)+x(9)))+0.5+x(10)*0.2235*(x(7)+x(9))/(x(2)-
LV_delta)*x(5)); %Vertical segments
%  Ld=LHd+LVd;
%  LdVector(k)=Ld;
%  Lt_skin=2*(Ld+M);                  %DC Total Inductance due to skin
effect

%LS=Lt_skin;
%LtVector(k)=Lt_skin;
LtVector(k)=Lt_noskin;

 %DC Resistance
 Rtrdc_v=rho_m*length_v/(x(7)*x(9));
 Rtrdc_h=rho_m*length_h/(x(8)*x(9));
 Rtrdc=Rtrdc_v+Rtrdc_h;
%AC Resistance loss due to skin effect from Kazimierczuk
 A_loss=(x(8)/delta(scalefactor_f))*sqrt(x(9)/x(3));
```

```
 A_lossVector(scalefactor_f)=A_loss;
 Rskin=A_loss*Rtrdc*(((exp(2*A_loss)-exp(-
2*A_loss)+2*sin(2*A_loss))/...
     ((exp(2*A_loss)+exp(-2*A_loss)-2*cos(2*A_loss)))));
 Rskin_vs_freq(scalefactor_f)=Rskin;
 Rprox=A_loss*Rtrdc*(1/3)...
    *(exp(A_loss)-exp(-A_loss)-2*sin(A_loss))/(exp(A_loss)+exp(-
A_loss)+2*cos(A_loss));
 Rprox_vs_freq(scalefactor_f)=Rprox;

%Rac=rho_m*(length_v+length_h)/(x(9)*delta(scalefactor_f))*sqrt(x(9)/x(
3))*(Rskin+Rprox);
 Rprox=0;   %Proximity effect is zero for a single layer solenoid!
 Rac=Rskin+Rprox;
 Rac_vsk(k)=Rac;
 Rs=Rtrdc+Rac;
 RS=Rs;

%AC Resistance loss due to skin effect from Ulrich

%Capacitance Turn-to-Turn (first-order swag at parasitic capacitance)
% A_t=2*(l+x(7))*x(8)+2*(x(2)-x(7))*x(9);         %Area of a turn
% Ctt=ep*A_t/(x(3)-x(9))                          %Turn-Turn Capacitance
% Ct=Ctt/(x(6)-1);                                %Total Turn
Capacitance

%Capacitance Turn-to-Turn all terms
Ctop =  ep*l*x(8)/(x(3)-x(9));  %C4-8
Cbottom=ep*l*x(8)/(x(3)-x(9));  %C2-6
Ctopbottom=ep*l*x(8)/sqrt(x(3)^2-x(2)^2); %C2-4, C4-6, C6-8      %This
term is in error and should be adjusted!!!!
%Ctopbottom=0;
Cx=ep*l*x(8)/x(3);%C2-8
%Cx=0;
Cfront=ep*x(7)*(x(2)+x(8))/(x(3)-x(9)); %C1-5
Cback=ep*x(7)*(x(2)+x(8))/(x(3)-x(9));  %C3-7
Cfrontback=ep*x(9)*(x(2)-x(8))/(l-2*x(7));%C1-3, C3-5, C5-7
Cy=ep*sqrt(x(7)^2+x(9)^2)*(x(2)-x(8))/sqrt(x(1)^2+(3*x(3)/2)^2);%C2-8
Ctt=Ctop+Cbottom+3*Ctopbottom+Cx+Cfront+Cback+3*Cfrontback+Cy;
Ct=Ctt/(x(6)-1);
%Capacitance to Substrate for SU8
% Cbottom_SU8=3*ep*(length_h/2)*x(9)/(x(11));          %Bottom turns'
Capacitance to Substrate
% Ctop_SU8=3*ep*((length_h)/2)*x(9)/(x(11)+x(2)+2*x(8)); %Top turns'
Capacitance to Substrate
% C_SU8=Cbottom_SU8+Ctop_SU8;
% C=Ct+C_SU8;
% CVector(k)=C;
%Resistance of Substrate
GSUB=1e-9; %was 1e-12
RSUB=2/((length_h+length_v)*x(9)*GSUB);
CSUB=0.5*(length_h+length_v)*x(9)*1e-9; %was 1e-9
ep_BSG=8.854e-18*4.6; %was 3.9
%Capacitance of Posts to Ground
CIS=2*x(6)*(x(2)+x(8))*x(9)/x(11)*ep;
%CIS=0.5*(length_h+length_v)*x(9)*ep_BSG/x(11);
```

```
RP=1/(x(4)^2*CIS^2*RSUB)+RSUB*(CIS+CSUB)^2/CIS^2;
CP=CIS*(1+x(4)^2*(CIS+CSUB)*CSUB*RSUB^2)/(1+x(4)^2*(CIS+CSUB)^2*RSUB^2)
;
CS=Ct;
%Reactances and Impedance
XCP=1/(1i*x(4)*CP);
XCPf(scalefactor_f)=XCP;
XCS=1/(1i*x(4)*CS);
XCSf(scalefactor_f)=XCS;
XLS=1i*x(4)*Lt;
XLSf(scalefactor_f)=XLS;
RSLSCS=(RS+XLS)*XCS/(RS+XLS+XCS);
RPCP=RP*XCP/(RP+XCP);
Z=RSLSCS*RPCP/(RSLSCS+RPCP);
Zf(scalefactor_f)=Z;
%Z=RP*XCP*XCS*(RS+XLS)/(RP+XCP+XCS+RS+XLS)

%Impedance of Solenoid
 XLt=x(4)*Lt;
 C=Ct+CIS;
 XC=1/(x(4)*C);
 Z=       (-1i*XC)*(Rs+(1i)*XLt)/(Rs+1i*XLt-1i*XC);
Ztot(k)=(-1i*XC)*(Rs+(1i)*XLt)/(Rs+1i*XLt-1i*XC);
% Z=       XC*XLt-1i*Rs*XC/(Rs+1i*(XLt-XC));
% Ztot(k)=XC*XLt-1i*Rs*XC/(Rs+1i*(XLt-XC));
% Z=sqrt((Rs+1i*XLt)/1i*x(4)*C);
% gamma=sqrt((Rs+1i*XLt*1i*x(4)*C));
% gammaZ=gamma*Z;

Rtrace=real(Z);
Xtrace=imag(Z);
XtraceVector(k)=Xtrace;
scalefactor_f;

LL(k)=L;                                          %DC Self
MM(k)=M;
PP(k)=I^2*Rs;
JJ(k)=I/(4);
%ZZ(k)=(Z);
freq(k)=x(4)/(2*pi());
Zmag(k)=abs(Z);
phi(k)=angle(Z);
%f=-Lt
f=-Xtrace/x(4);
%Quality Factor
wLR=x(4)*LS/RS;
SLF=RP/(RP+(1+(wLR)^2)*RS);
SRF=1-RS^2*(CP+CS)/LS-x(4)^2*LS*(CS+CP);
Q(k)=wLR*SLF*SRF;
%Q(k)=(x(4)*Lt/Rs)*(1-(Rs^2*C/Lt)-x(4)^2*Lt*C)
%Q(k)=imag(Z)/real(Z)
%Q(k)=x(4)*Lt/Rs;
%Q(k)=(x(4)*Lt/Rs)*(1-Rs^2*C/Lt-x(4)^2*Lt*C)
%Q(k)=(x(4)*Lt/Rtrdc)*(1-(Rtrdc^2*Ct/Lt)-x(4)^2*Lt*Ct);
%Q(k)=(Rs/(x(4)*Lt))*(1-(x(4)*sqrt(Lt*Ct))^2);    %Yue's Paper
%Q(k)=(x(4)*Lt/Rs)*(1-Rs^2*Ct/Lt-x(4)^2*Lt*Ct); %Yue's Paper
```

```
%Ztotal(p)=Ztot(k);
%Ltotal(p)=Lt;
%Qtotal(p)=Q(k);
sol_length;
LfromZ(k)=Xtrace/x(4);
LfromZ_unit(k)=LfromZ(k)/sol_length;
RfromZ(k)=Rtrace/4;
Rac(k)=Rac;
%Rac(k)=Rtrace*50/abs(Z);    %ac resistance normalized to magnitude of
Z and 50 ohms
x=x';
xx1(k)=x(1);xx2(k)=x(2);xx3(k)=x(3);xx4(k)=x(4);xx5(k)=x(5);xx6(k)=x(6)
;
xx7(k)=x(7);xx8(k)=x(8);xx9(k)=x(9);xx10(k)=x(10);xx11(k)=x(11);
LfromZ_vs_D(scalefactor_f,k)=LfromZ(k);
LfromZ_unit_vs_D(scalefactor_f,k)=LfromZ_unit(k);   %per unit length
inductance
RfromZ_vs_D(scalefactor_f,k)=RfromZ(k);
Q_vs_D(scalefactor_f,k)=Q(k);
Zmag_vs_D(scalefactor_f,k)=Zmag(k);
Zphi_vs_D(scalefactor_f,k)=phi(k);
Rac_vs_D(scalefactor_f,k)=Rac(k);
Rs_vs_D(scalefactor_f,k)=Rs;
%Length_vs_D(scalefactor_f,k)=sol_length(k);
%%%%%%%%%Plots versus frequency and geometry
% % if scalefactor_D==105
% % figure(23)
% % plot(freq(k),Lt_noskin,'--rs')
% % hold on
% % figure(24)
% % plot(freq(k),Lt,'--ro')
% % hold on
% % figure(25)
% % plot(freq(k),LfromZ(k),'--rs')
% % hold on
% % figure(26)
% % plot(freq(k),Q(k),'--ro')
% % hold on
% % figure(27)
% % plot(freq(k),Zmag(k),'--ro')
% % hold on
% % figure(28)
% % plot(freq(k),phi(k),'--ro')
% % hold on
% % figure(29)
% % plot(freq(k),Rac(k),'--rs')
% % hold on
% % end
% % if scalefactor_D==205
% % figure(23)
% % plot(freq(k),Lt_noskin,'--ys')
% % hold on
% % figure(24)
% % plot(freq(k),Lt,'--yo')
% % hold on
% % figure(25)
% % plot(freq(k),LfromZ(k),'--ys')
```

```
% % hold on
% % figure(26)
% % plot(freq(k),Q(k),'--yo')
% % hold on
% % figure(27)
% % plot(freq(k),Zmag(k),'--yo')
% % hold on
% % figure(28)
% % plot(freq(k),phi(k),'--yo')
% % hold on
% % figure(29)
% % plot(freq(k),Rac(k),'--ys')
% % hold on
% % end
% % if scalefactor_D==305
% % figure(23)
% % plot(freq(k),Lt_noskin,'--gs')
% % hold on
% % figure(24)
% % plot(freq(k),Lt,'--go')
% % hold on
% % figure(25)
% % plot(freq(k),LfromZ(k),'--gs')
% % hold on
% % figure(26)
% % plot(freq(k),Q(k),'--go')
% % hold on
% % figure(27)
% % plot(freq(k),Zmag(k),'--go')
% % hold on
% % figure(28)
% % plot(freq(k),phi(k),'--go')
% % hold on
% % figure(29)
% % plot(freq(k),Rac(k),'--gs')
% % hold on
% % end
% % if scalefactor_D==405
% % figure(23)
% % plot(freq(k),Lt_noskin,'--bs')
% % hold on
% % figure(24)
% % plot(freq(k),Lt,'--bo')
% % hold on
% % figure(25)
% % plot(freq(k),LfromZ(k),'--bs')
% % hold on
% % figure(26)
% % plot(freq(k),Q(k),'--bo')
% % hold on
% % figure(27)
% % plot(freq(k),Zmag(k),'--bo')
% % hold on
% % figure(28)
% % plot(freq(k),phi(k),'--bo')
% % hold on
% % figure(29)
```

```
% % plot(freq(k),Rac(k),'--bs')
% % hold on
% % end
% % if scalefactor_D==505
% % figure(23)
% % plot(freq(k),Lt_noskin,'--cs')
% % hold on
% % figure(24)
% % plot(freq(k),Lt,'--co')
% % hold on
% % figure(25)
% % plot(freq(k),LfromZ(k),'--cs')
% % hold on
% % figure(26)
% % plot(freq(k),Q(k),'--co')
% % hold on
% % figure(27)
% % plot(freq(k),Zmag(k),'--co')
% % hold on
% % figure(28)
% % plot(freq(k),phi(k),'--co')
% % hold on
% % figure(29)
% % plot(freq(k),Rac(k),'--cs')
% % hold on
% % end

%%%%%%%%%%%To Plot 3D surfaces%%%%%
Q3D(k,q)=Q(k);
L3DfromZ(k,q)=LfromZ(k);
Z3Dtotal(k,q)=Zmag(k);
eangle(k)=eps;
Volumefactor(k,q)=(xx1(k)+xx7(k))*(xx11(k)+xx2(k)+xx8(k))*(xx6(k)*(xx3(
k)+xx9(k)));
ND(k,q)=x(3)*x(6);
end
k=0;
end
% [X,Y]=meshgrid(144:1:145,105:100:505);
% %hold on
% figure(11)
% surf(X,Y,L3DfromZ)
% hold on
% figure(12)
% surf(X,Y,Q3D)
% hold on
% figure(13)
% surf(X,Y,Z3Dtotal)
% hold on
% figure(14)
% surf(X,Y,ND)
end
% figure(1)
% plot(Length_vs_D(:,1),LfromZ_vs_D(:,1),'c');
% hold on
% plot(Length_vs_D(:,2),LfromZ_vs_D(:,2),'m');
% hold on
```

```
% plot(Length_vs_D(:,3),LfromZ_vs_D(:,3),'y');
% hold on
% plot(Length_vs_D(:,4),LfromZ_vs_D(:,4),'r');
% hold on
% plot(Length_vs_D(:,5),LfromZ_vs_D(:,5),'g');
% hold on
%plotedit on
figure(100)
plot(LfromZ_vs_D(:,1),'-+c')
xlabel('Frequency(GHz)','FontSize',16)
ylabel('Inductance(H)','FontSize',16)
title('Solenoid Inductance vs. Frequency','FontSize',16)
 hold on
 %txtar =  annotation('textarrow',[.5,.5],[.75,.25],'string','We are
here.','FontSize',14);
 %text(pi,0,' \leftarrow sin(\pi)','FontSize',14)
plot(LfromZ_vs_D(:,2),'-om')
hold on
plot(LfromZ_vs_D(:,3),'-*y')
hold on
plot(LfromZ_vs_D(:,4),'-.r')
hold on
plot(LfromZ_vs_D(:,5),'-xg')
hold on
legend('D = 10um','D = 20um','D = 30um','D = 40um','D = 50um')
text(20, 5e-9,'W = 145 um')
%axis([0 40 -6e-9 20e-9])
figure(101)
plot(Q_vs_D(:,1),'-+c')
xlabel('Frequency(GHz)','FontSize',16)
ylabel('Quality Factor','FontSize',16)
title('Solenoid Quality Factor vs. Frequency','FontSize',16)
hold on
%annotation('textarrow',20 ,5)
plot(Q_vs_D(:,2),'-om')
hold on
plot(Q_vs_D(:,3),'-*y')
hold on
plot(Q_vs_D(:,4),'-.r')
hold on
plot(Q_vs_D(:,5),'-xg')
hold on
legend('D = 10um','D = 20um','D = 30um','D = 40um','D = 50um')
text(20, 0,'W = 145 um')
% figure(102)
% plot(Zmag_vs_D)
% hold on
% figure(103)
% plot(Zphi_vs_D)
% hold on
figure(104)
plot(RfromZ_vs_D(:,1),'-+c')
xlabel('Frequency(GHz)','FontSize',16)
ylabel('AC Resistance','FontSize',16)
title('Solenoid AC Resistance vs. Frequency','FontSize',16)
hold on
%annotation('textarrow',20 ,1000)
```

```
plot(RfromZ_vs_D(:,2),'-om')
hold on
plot(RfromZ_vs_D(:,3),'-*y')
hold on
plot(RfromZ_vs_D(:,4),'-.r')
hold on
plot(RfromZ_vs_D(:,5),'-xg')
hold on
legend('D = 10um','D = 20um','D = 30um','D = 40um','D = 50um')
text(20, 2000,'W = 145 um')
% figure(105)
% plot(Rac_vs_D(:,1),'c')
% xlabel('Frequency(GHz)','FontSize',16)
% ylabel('AC Resistance','FontSize',16)
% title('Rac Solenoid AC Resistance vs. Frequency','FontSize',16)
% hold on
% plot(Rac_vs_D(:,2),'m')
% hold on
% plot(Rac_vs_D(:,3),'y')
% hold on
% plot(Rac_vs_D(:,4),'r')
% hold on
% plot(Rac_vs_D(:,5),'g')
% hold on
% figure(106)
% plot(Length_vs_D(:,1),'c')
% hold on
% plot(Length_vs_D(:,2),'m')
% hold on
% plot(Length_vs_D(:,3),'y')
% hold on
% plot(Length_vs_D(:,4),'r')
% hold on
% plot(Length_vs_D(:,5),'g')
% hold on
%%%%%%%%%%%%%%%%%%%%%%%%%%%%%%%%%%%%%%%%%%%
g=[];H=[];
```

VIII. Appendix B: Solenoid DOE Structures

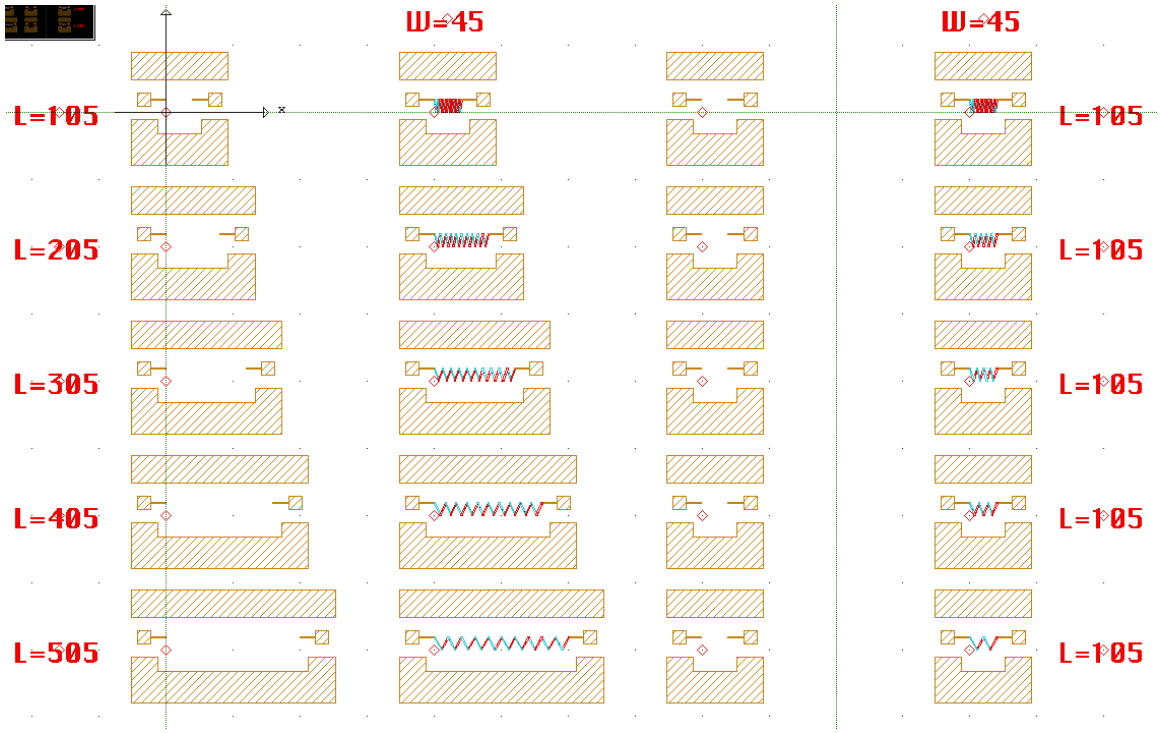

Fig. 51 Solenoid array 1 where *W* is the coil y-height and *Len* the coil length in x (all turns are 5µm's wide).

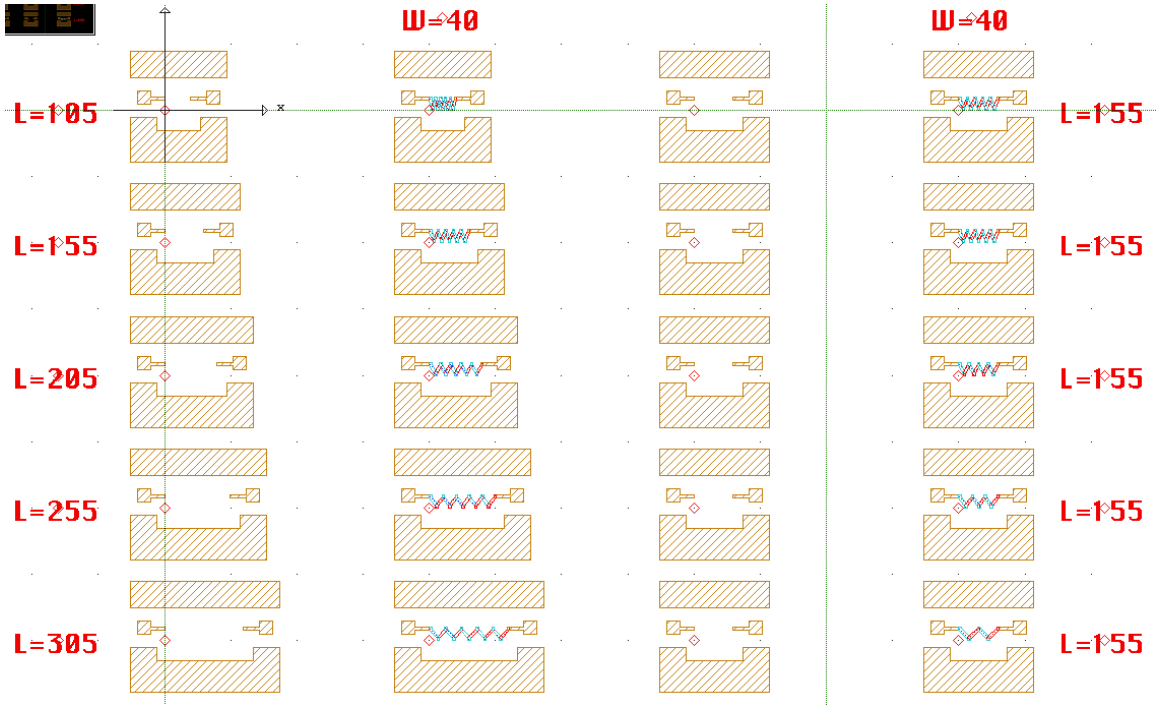

Fig. 52 Solenoid array 2 where *W* is the coil y-height and *Len* the coil length in x (all turns are 10-µm's wide).

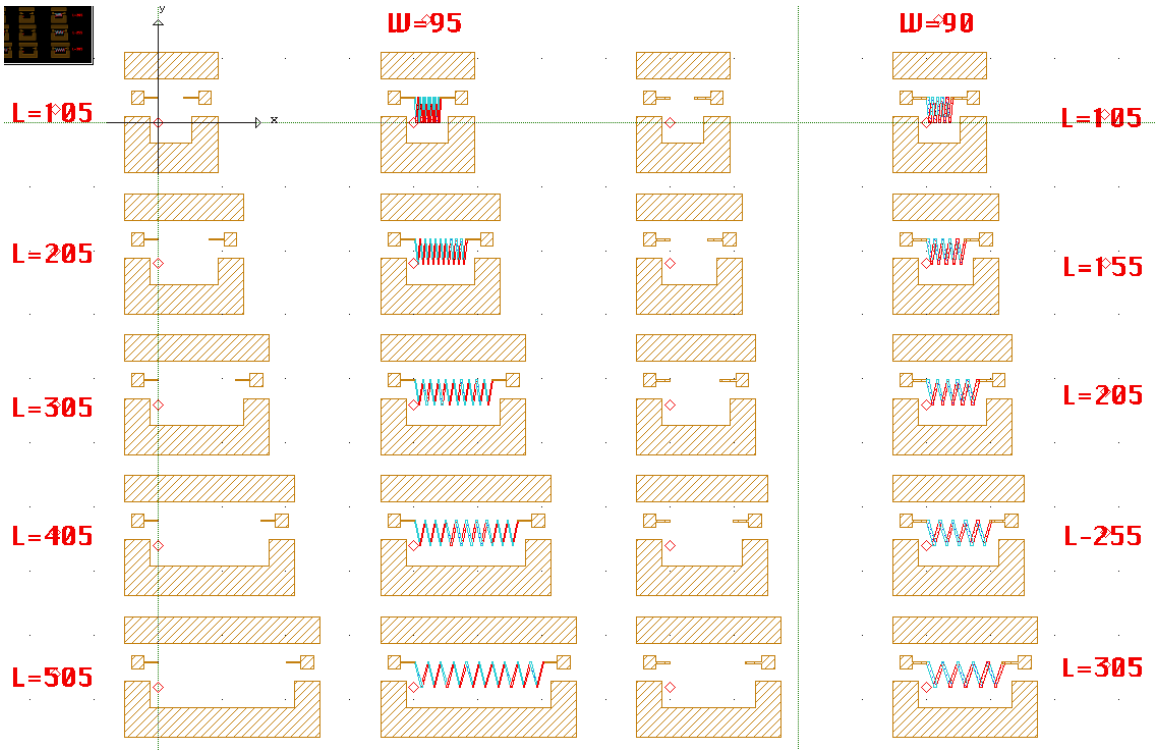

Fig. 53 Solenoid array 3 where *W* is the coil y-height and *Len* the coil length in x (turn widths are 5µm and 10µm for W of 95µm and 90µm, respectively).

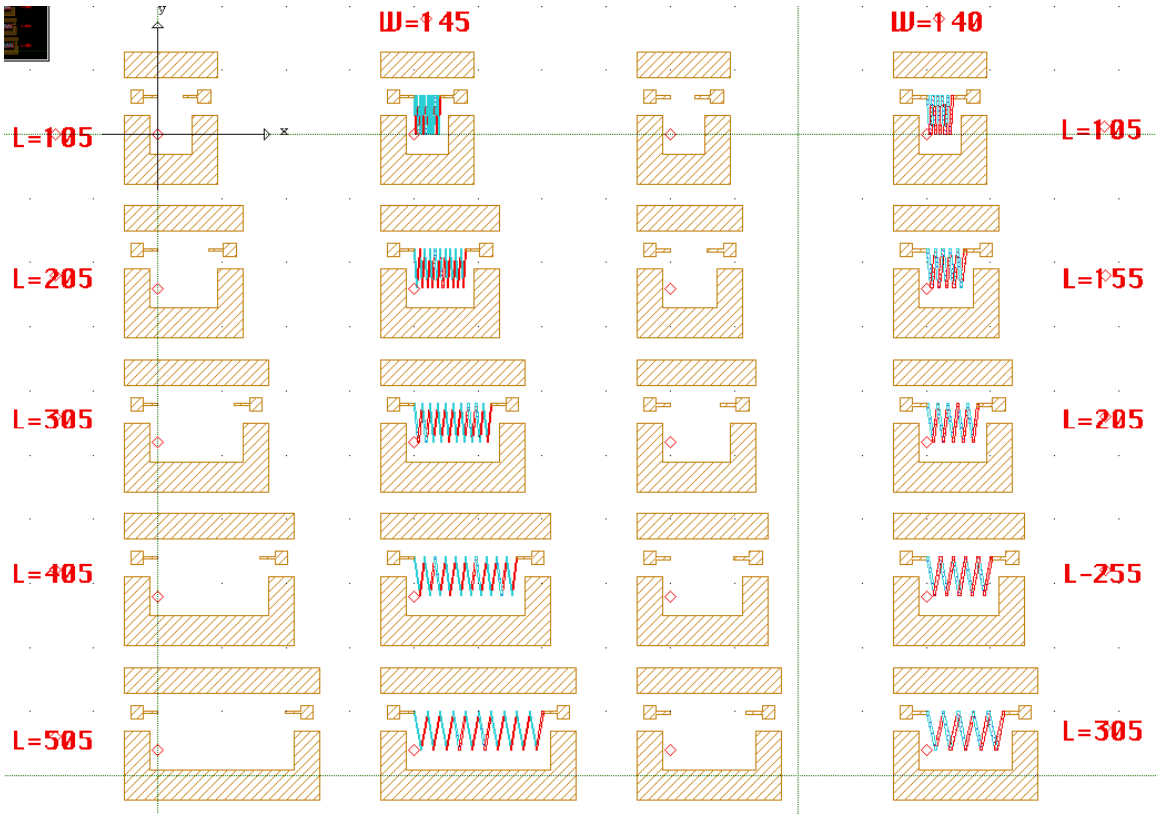

Fig. 54 Solenoid array 3 where *W* is the coil y-height and *Len* the coil length in x (turn widths are 5µm and 10µm for W of 95µm and 90µm, respectively).

IX. Appendix C: Solenoid Fabrication Process

Experimental Study

- Process Development

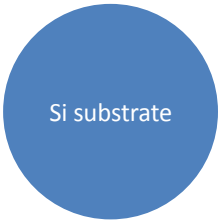

P-type silicon substrate with 1µm of thermal oxide top and bottom

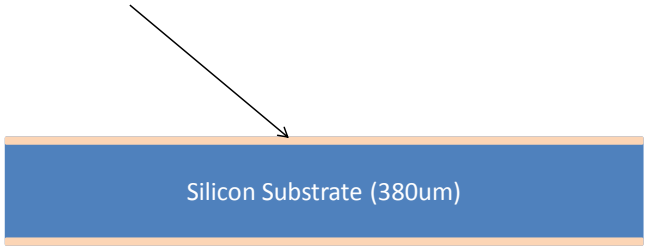

Experimental Study

- Process Development

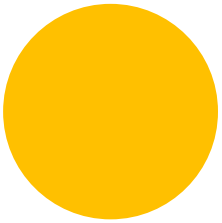

TiAu Seed layer deposited using Denton Discovery 18 DC Magnetron Sputter System

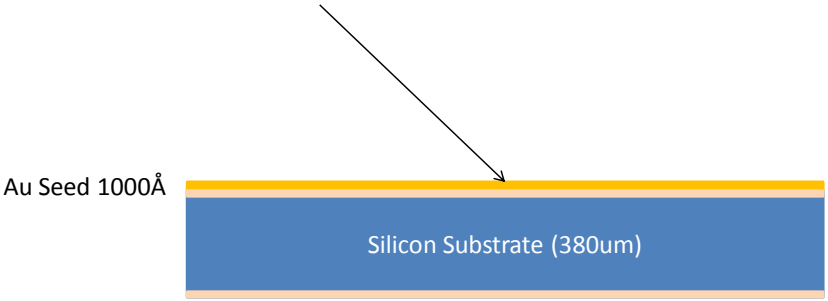

Experimental Study

- Process Development

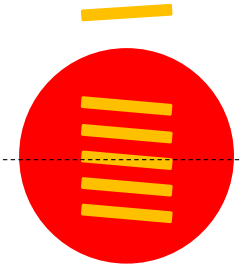

Photolithographically defined M1 pattern in the SU-8 Form
Using Karl Suss MA6 Backside Aligner (365nm, 7mW/cm^2)

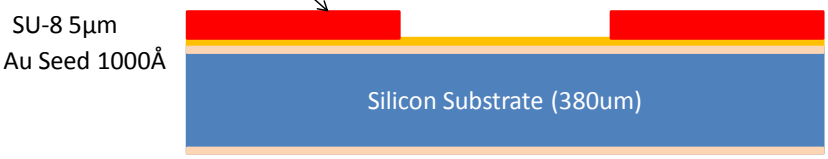

Experimental Study

- Process Development

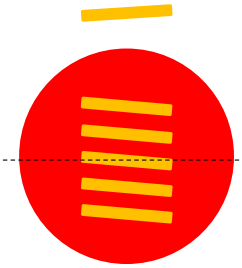

Electroplate Au inside, and to the top of the SU-8 forms
With Technic 25E plating bath (40% DC, 2mA/cm^2)

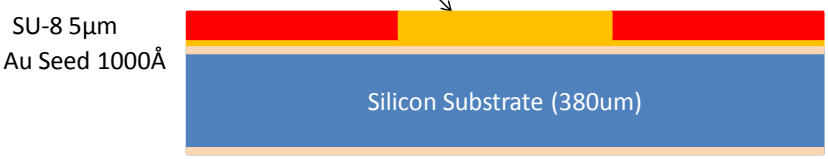

Experimental Study

- Process Development

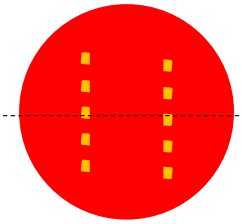

Photolithographically defined POST pattern in the SU-8 Form
Using Karl Suss MA6 Backside Aligner (365nm, 7mW/cm^2)

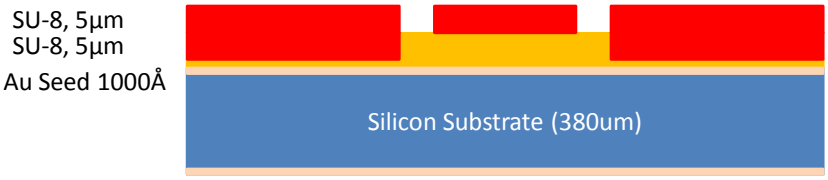

Experimental Study

- Process Development

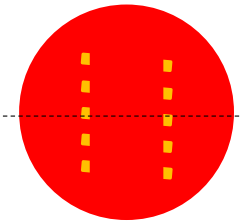

Electroplate Au inside, and to the top of the SU-8 forms
With Technic 25E plating bath (40% DC, 2mA/cm^2)

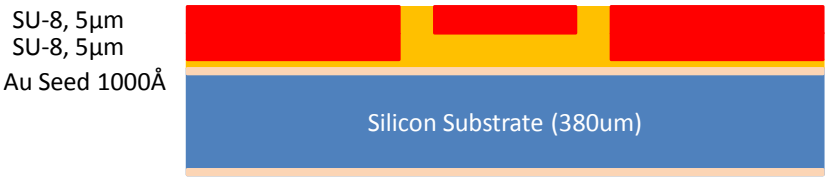

Experimental Study

- Process Development

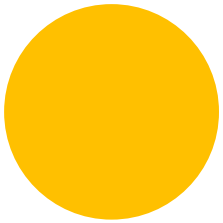

TiAu Seed layer deposited using Denton Discovery 18
DC Magnetron Sputter System for top metal layer

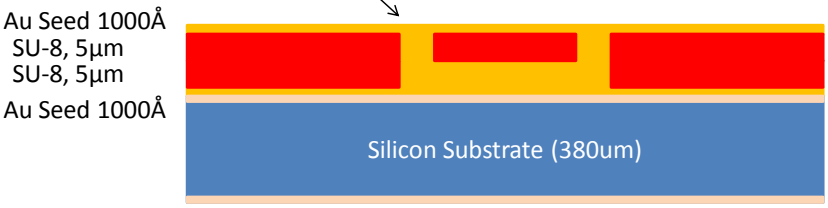

Experimental Study

- Process Development

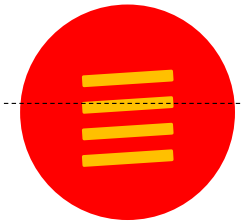

Photolithographically defined M2 pattern in the SU-8 Form
Using Karl Suss MA6 Backside Aligner (365nm, 7mW/cm^2)

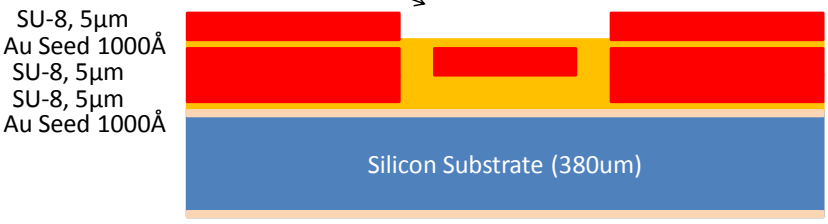

Experimental Study

- Process Development

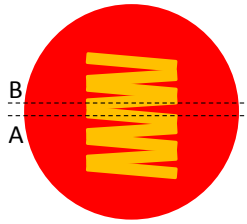

Electroplate Au inside, and to the top of the SU-8 forms
With Technic 25E plating bath (40% DC, 2mA/cm^2)

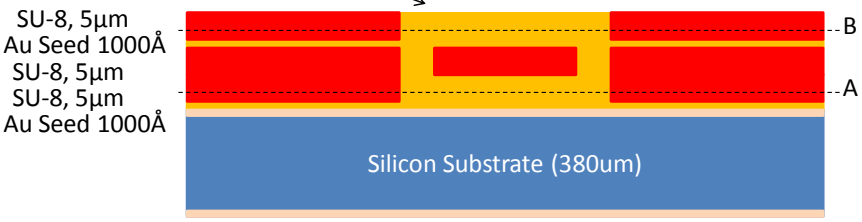

Experimental Study

- Process Development

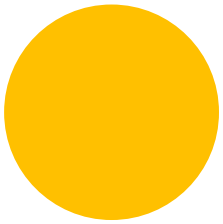

Oxygen plasma etch of SU-8 in barrel asher; SU-8
Removed above M2 seed layer only

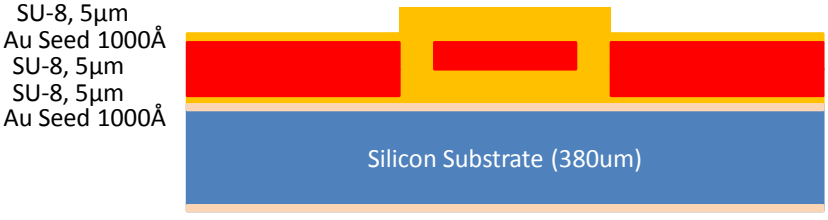

Experimental Study

- Process Development

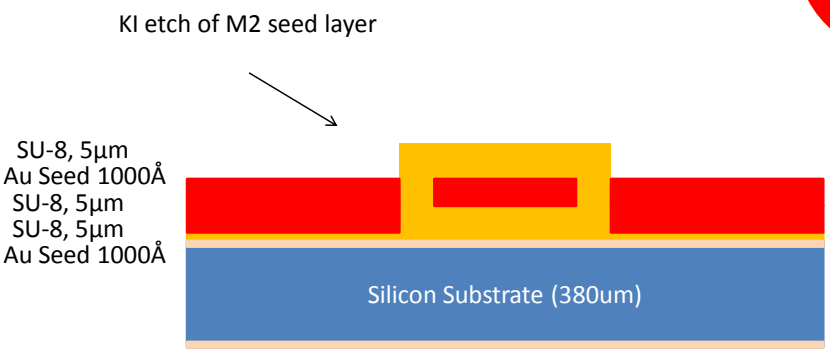

Experimental Study

- Process Development

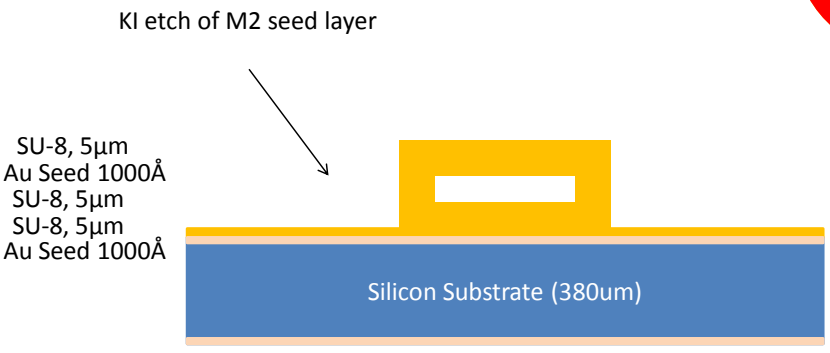

Experimental Study

- Proc

KI e

SU-8, 5µm
Au Seed 1000Å
SU-8, 5µm
SU-8, 5µm
Au Seed 1000Å

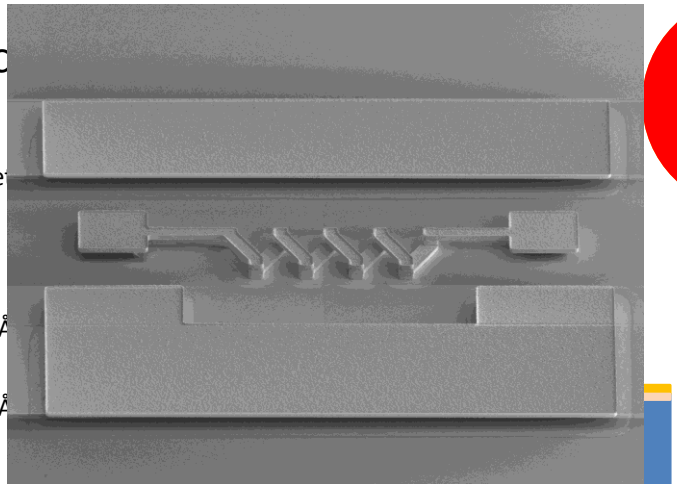

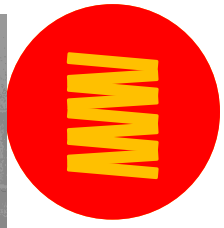

Completed top-side solenoid with SU-8 removed for clarity

Experimental Study

- Process Development

Flip wafer for backside processing

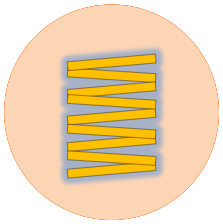

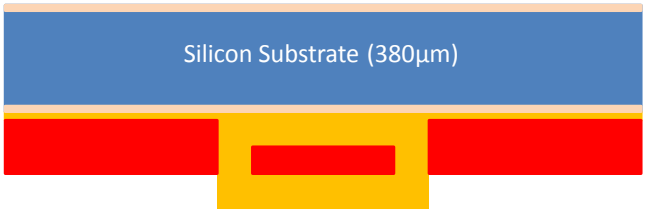

Experimental Study

- Process Development

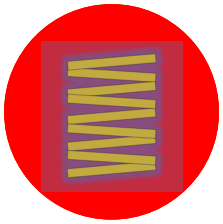

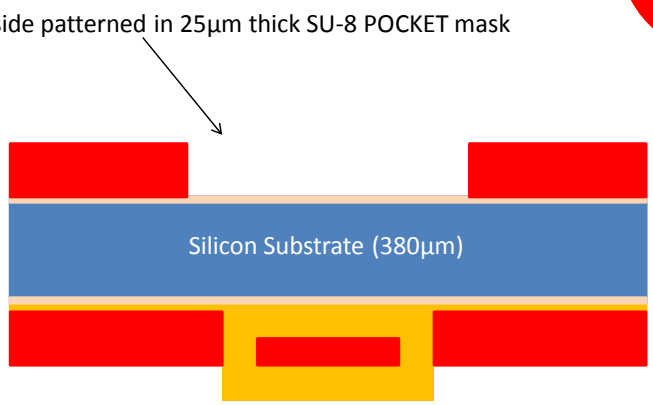

Experimental Study

- Process Development

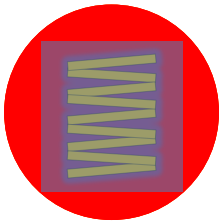

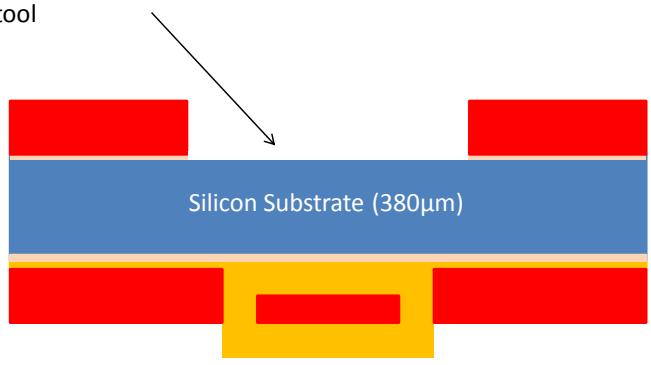

Experimental Study

- Process Development

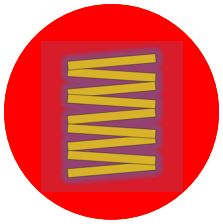

Reactive ion etch of silicon substrate layer beneath solenoids using Plasma Therm Versaline Deep Reactive Ion Etch tool and the Bosch process; etch stop on back-side SiO_2 layer

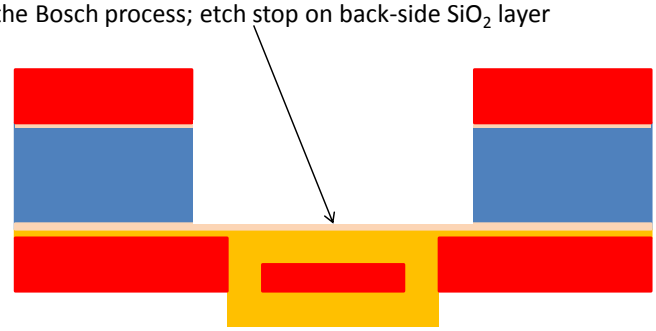

Experimental Study

- Process Development

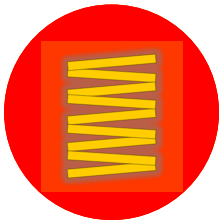

Reactive ion etch of SiO_2 layer using Plasma Therm 790 etch tool to expose M1 seed layer

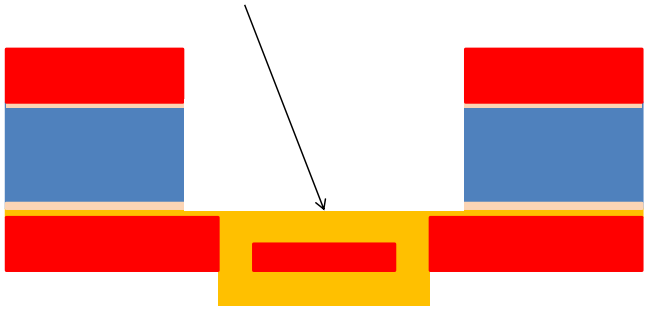

Experimental Study

- Process Development

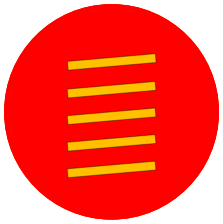

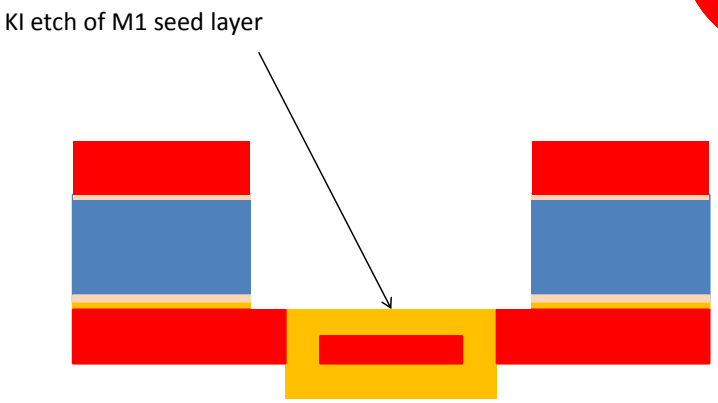

Experimental Study

- Process Development

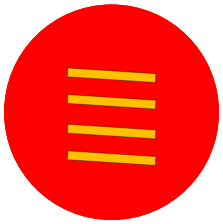

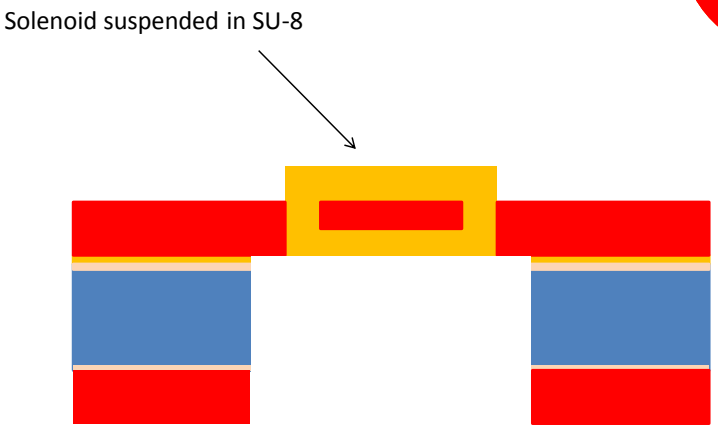

Experimental Study

- Proc

Sol

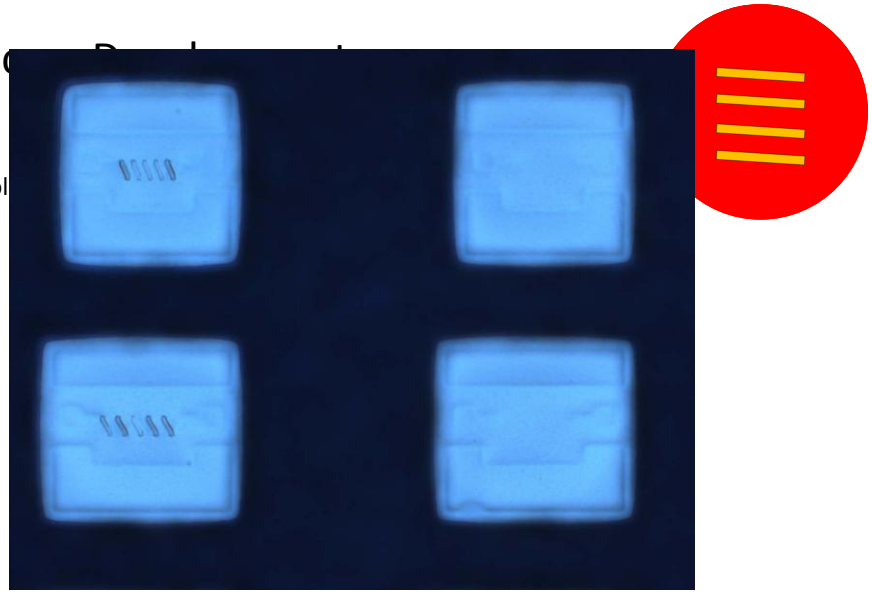

Suspended solenoids in SU-8 imaged through backside pockets in silicon wafer.

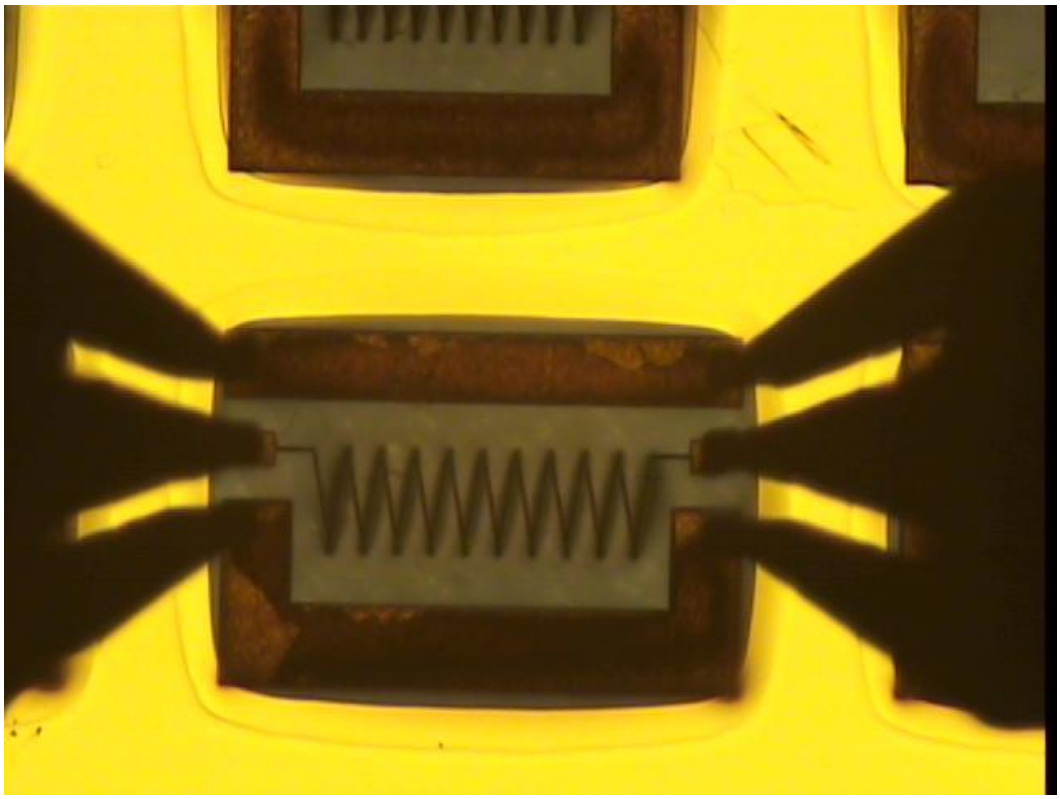

Suspended solenoids in SU-8 being electrically probed from the wafer top-side.